# CELLULAR INSTABILITY IN BINARY SOLIDIFICATION

By

© DEVARAJAN VENUGOPALAN

A Thesis

Submitted to the School of Graduate Studies

in Partial Fulfilment of the Requirements

for the Degree

Doctor of Philosophy

McMaster University

August 1982

# CELLULAR SOLIDIFICATION

Nature likes to hide

- Heracleitus

DOCTOR OF PHILOSOPHY (1982)
(Metallurgy)

McMASTER UNIVERSITY
Hamilton, Ontario

TITLE: Cellular Instability in Binary Solidification

AUTHOR: Devarajan Venugopalan, B.Tech. (I.I.T., Madras, India)
M.Eng. (McMaster University)

SUPERVISOR: Professor J.S. Kirkaldy

NUMBER OF PAGES: x;131

ABSTRACT

The steady-state growth of cells in binary alloy single phase solidification is examined theoretically and experimentally. The failure of the marginal-stability calculations to predict and describe the growth of stable cells indicates a theoretical gap in this field. The Zener-Hillert type model for cellular solidification proposed by Kirkaldy is discussed. In this theory the physics of cell growth demands that the interface be a non-equilibrium interface stabilized by kinetic and crystallographic effects. A quantitative model following this line is advanced for the steady-state growth of two-dimensional cells. The solution to the free boundary diffusion problem requires, in addition to the boundary conditions, two extra constraints. A principle of minimum cell root radius, surrogate to the principle of minimum rate of entropy production, is used to provide the additional conditions. Cell growth in the succinonitrile-salol system was studied experimentally. For a given set of growth conditions the cells have a unique steady-state spacing and length. Perturbation experiments about the steady-state support the validity of the optimization procedure used in the calculations. Quantitative predictions on steady-state growth are verified by the experiments.

ACKNOWLEDGEMENTS

I take this opportunity to thank sincerely all those who have assisted me in the course of this work. In particular, the following people have made invaluable contributions in making this thesis a reality:

- Professor Jack Kirkaldy who initiated, inspired and supervised this work and was the first to understand and explain the physics of cellular solidification. It was a pleasure to work with him.

- Professor Gary Purdy for his critical comments, suggestions and guidance. The interest he showed in this work was a source of inspiration.

- Professor Tom Timusk who along with Professors Kirkaldy and Purdy served on the supervisory committee and made many valuable suggestions.

- Mrs. Kathy Noon for the patient and excellent typing of the manuscript.

- Martin Van Oosten for preparing the diagrams.

- Tom Bryner who offered me his expertise in photography.

I am indebted to the faculty, staff and graduate students of the Department of Metallurgy for all the discussions I have had with them on this topic.

Financial assistance from the Sherman Estate in the form of a scholarship and from McMaster University in the form of a teaching assistantship are gratefully acknowledged.

TABLE OF CONTENTS

## LIST OF SYMBOLS

| | |
|---|---|
| $D$ | Diffusion coefficient in liquid |
| $G$ | Temperature gradient |
| $H$ | Latent heat of fusion |
| $k$ | equilibrium distribution coefficient |
| $l$ | Length of cells |
| $m$ | liquidus slope |
| $r$ | root radius of curvature |
| $s$ | cell spacing |
| $T_o$ | melting point of pure solvent |
| $T_1$ | temperature of cell tips |
| $T_2$ | temperature of cell roots |
| $v$ | velocity of cells parallel to the temperature gradient |
| $v_n$ | normal velocity of the interface |
| $X$ | composition in liquid |
| $X_o$ | alloy composition |
| $X_1$ | liquid composition at the cell tips |
| $X_2$ | liquid composition at the cell roots |
| $X_s$ | solid composition |
| $x;y$ | Cartesian coordinates |
| $\sigma$ | solid-liquid interfacial energy |

LIST OF FIGURES

# CHAPTER 1
# INTRODUCTION

Solidification is a central phase transformation in the science and engineering of metallurgy. In the manufacture of metallic articles, the starting material most often is liquid metal which is solidified into desired shapes to be used as such or after further processing. In most cases, the engineering properties of the product can be directly related to the manner in which the material solidified. For this reason understanding of the various aspects of solidification is crucial to the metallurgist in the quest for producing better products.

The properties of a given material are related to its microstructure via well established relations. The goal of the physical metallurgist is to develop and control the processing of materials to obtain the desired structure and hence the desired properties. Quite often the structure produced during solidification has a large influence on how the material should be processed and also on the final structure and properties. Empirical relations between solidification conditions and the structure are known but there has been no major theoretical advances in this field for nearly two decades.

The microstructure produced during solidifiction is related to the morphology of the solid-liquid interface during solidification. As the solidification conditions are varied, the morphology of the interface changes. In a binary alloy, the factors which affect the morphology are the alloy content, the rate of solidification and the

temperature gradient in which solidification occurs. Empirically it has been observed that proper control of these variables can produce either a planar interface or a non-planar interface. The non-planar interfaces can be further classified into dendritic, cellular or irregular interfaces. There is empirical evidence showing a continuous transition between cellular and dendritic interfaces but no such evidence exists for the transition between planar and cellular interfaces. The dendritic structures are the most important for engineering applications. Although many researchers have studied this phenomenon for several decades there has been no major theoretical advances in this field and there is no complete understanding of why dendrites or cells form. Thus cellular and dendritic solidification pose important theoretical problems, the solution to which will advance our knowledge of solidification greatly.

Recently Kirkaldy presented new ideas on cellular solidification, including a model for the evolution and the steady-state growth of cells. His ideas have advanced our understanding of the physics of the cell problem. What remains to be done is the development of a rigorous quantitative model, not only to test the new ideas but also to make quantitative predictions on the structures produced during cellular solidification. This is the challenge taken up in this work. A typical cellular interface is shown in figure 1.

In chapter 2, previous work on this problem is reviewed. In chapter 3, a mathematical model is developed based on the semi-quantitative model of Kirkaldy. Experimental measurements were carried out on a

transparent organic model system to facilitate quantitative measurements. These are described in chapter 4. In chapter 5, a comparison is made between the theory and the experiments and the model is further amplified and discussed.

# CHAPTER 2

# REVIEW OF PREVIOUS WORK

## 2.1 Introduction

The problem of cellular instability of the binary solid-liquid interface during controlled solidification has been under investigation for several decades. Like most problems in metallurgy, empirical observations preceded theoretical advances in the cell problem. This problem has been attacked from many different directions using, for example, perturbation methods, extension of methods used in the related problem of dendrite growth and methods based on irreversible thermodynamics. In spite of the fact that this problem is quite "old", it was not until recently that an adequate description of the physics of stable cells was presented. A complete quantitative description of the steady-state cell problem has not yet been presented. In this chapter, we shall examine the previous work done on the cell problem.

## 2.2 Experimental Observations

The first reported observation of cellular structure in solidification was made by Buerger[1] in 1934. He referred to this structure as "lineage structure". Pond and Kessler[2] observed hexagonal arrays of cells in impure lead and tin solidified in a temperature gradient. Rutter and Chalmers[3] reported the results of a systematic set of experiments on the instability of the solid-liquid interface in lead-tin alloys. The main findings of this work are:

a) Under certain solification conditions (alloy content, temperature gradient and velocity), the solid-liquid interface assumes a regular cellular morphology.

b) The cell size decreased with increasing velocity and c) the cell size increased with increasing alloy content.

The occurrence of cells was attributed to the presence of a supercooled region of liquid in contact with the solid. This led to the development of the constitutional supercooling criterion [CS criterion] which is dealt with in the following section. According to this criterion, when the growth velocity exceeds a critical value, the planar interface becomes unstable and breaks down. This condition was verified by Tiller et al.[4].

Walton et al.[5] observed that while the planar interface became unstable at the critical velocity given by the CS criterion, cells were obtained only at velocities much higher than the critical velocity for planar interface break-down. At velocities slightly above the critical velocity, "pox" structure and irregular breakdown occurred. These experiments were conducted on the lead-tin system. Similar observations were made by Herman and Damiano[6] in zinc and by Bolling et al.[7] in germanium.

Kramer et al.[8] considered the problem of microsegregation attending cellular solidification. The cell tip temperature was measured in a lead-tin alloy. The solute concentration at the tip, in the liquid and in the solid, were calculated from the measured tip temperature and from the phase diagram. It was found that the solute concentration in the solid at the tip approaches $kC_o$ for small values

of $G_L/vC_o$, and $C_o$ for large values of the parameter ($C_o$ is the solute content of the alloy, $G_L$ is the thermal gradient in the liquid, v is the growth velocity and k is the equilibrium ditribution coefficient). In other words, the effective distribution coefficient at the tip varied from k to unity as growth conditions were varied.

Morris and Winegard[9] studied the effects of crystal defects and orientation on cellular solidification. They observed that the planar interface became unstable first at grain boundaries and at the intersection of dislocations with the interface. They found a large influence of crystallorgraphic orientation, with respect to the growth direction, on the morphology of the solid-liquid interface. The elongated, hexagonal arrays of cells were obtained only when the cell walls were parallel to a plane on the [100] zone in lead-antimony alloys. They also reported that small changes in velocity did not alter the steady-state spacing of cells; however, when the velocity was changed by a large value, the spacing changed, decreasing with an increase in velocity.

Sharp and Hellawell[10] reported, from their experimental observations on Al-Cu alloys, that at the cell tips, the curvature is so small as to render negligible capillarity effect at the tip at growth velocities smaller than the dendrite-transition velocity.

Burden and Hunt[11] measured the tip temperature in Al-Cu alloys. Their results showed that the tip temperature first increased with velocity and then decreased. The tip concentration, in turn, decreased and then increased with velocity.

Jin and Purdy[12] conducted experiments on the Fe-8wt%Ni alloy. They reported that the tip concentration decreased rapidly

with velocity at the low velocity region and remained essentially independent of velocity at higher velocities. The tip concentration and the cell spacing decreased with increasing temperature gradient at constant velocity. They also observed that at the growth velocities encountered, the capillarity effect was negligible at the cell/dendrite tips.

Coulet et al.[13] investigated cellular growth in the Cu-Au system. They measured the solute profile in the solid behind the interface. Periodic, sharp peaks in solute concentration were observed just behind the "cusp" at the solid side of the interface. The solute concentration profile measured at a large distance behind the interface showed an absence of these sharp peaks and was approximately sinusoidal.

One of the difficulties in observing cellular solidification interface in metallic systems is due to the fact that metals are opaque to visible light radiation and so all examinations of the interface structure had to be done by interrupting the steady-state growth by either decanting techniques or quenching the sample. Chadwick[14] has warned of the artifacts created by a film of liquid which adheres to the decanted interface and then freezes. Whether or not quenching experiments preserve the actual interface shape is not known.

Jackson and Hunt[15] experimented with a number of transparent organic chemicals which can be used as model systems. Based on empirical observations, Jackson and Hunt concluded that those organic chemicals, otherwise called plastic crystals, which do not facet during solidification can be used as model systems to study solidification in metallic systems. Examples are carbon tetrabromide, and succino nitrile. Since

that time these and other organic materials have been employed successfully to study various aspects of solidification. Jackson and Hunt[16], Glicksman[17] and Schaefer and Glicksman[18] have discussed much of this type of work.

There are several advantages in using these model systems. They are transparent and so the interface can be observed directly during solidification. Also, these materials have very low melting points and so the experimentation is rather simpler as compared with the experimentation in metallic systems. But, one of the drawbacks is that these materials are not as well characterized thermodynamically as metals.

Cellular structures have been observed in alloys of carbon tetrabromide with salol and hexachloroethane, and in impure succinonitrile.

## 2.3 Theoretical Work

### 2.3.1 Perturbation methods

Rutter and Chalmers[3] advanced the qualitative idea that above a critical velocity, a zone of supercooled liquid is to be formed in front of a growing planar interface. If a protuberence develops on the interface, it will grow faster than the rest of the interface and lead to a non-planar morphology of the interface. This condition, known as the constitutional supercooling criterion, was quantified by Tiller et al.[4]. It predicts that when the growth velocity,

$$v > G_L D_L k/mC_o(1-k) \qquad (2.1)$$

the planar interface is unstable and non-planar interfaces are obtained. Here the symbols have the usual meaning given in the List of Symbols. This criterion is conventionally shown on the phase diagram as in figure 2. The cellular structure was considered as a result of the growth of periodic protuberances. At very high velocities, dendritic solidification took place. The cell spacing was given intuitively as $D_L/v$. While inequality (1) was found to predict the instability of a planar interface, experiments showed that cells are obtained only when the velocity far exceeds that given by the right hand side of (2.1)[5].

Mullins and Sekerka[19] carried out rigorous analysis of the morphological stability of a planar interface. The effect of capillarity was included. Steady-state thermal and solute fields were expressed with reference to a perturbed planar interface and the behaviour of the perturbation was analyzed. The perturbation itself was given in terms of a Fourier series. The rate of change of amplitude of the Fourier components were calculated. The planar interface is stable when all Fourier components decay. The principal finding of this study is that capillarity effect enhances the stability of the planar interface. The cell spacing was given as the wavelength of the fastest growing fourier component. While this theory predicts the marginal instability of the planar interface rather accurately, the predictions on the cell spacings are poorly confirmed by the experiments[13,19]. This is not surprising because the Mullins and Sekerka theory addresses itself only to the problem of marginal stability of planar interface rather than steady-state cell growth. The assumptions of steady diffusion fields around a small perturbation are not applicable as these pertur-

bations grow. The problem becomes unyielding as the perturbations become large.

It is worthwhile here to note some improvements made to the perturbation analysis. Tarshis and Tiller[20] considered the effect of interface attachment kinetics on the stability of the planar interface. They found that slow kinetics has a significant stabilizing effect. Shewmon[21] investigated the stability of interfaces in solid-solid transformations. His conclusion was that low interface mobility has a stabilizing effect on the interface.

Despite their elegance, the perturbation theories of Mullins and Sekerka fail when the amplitude of perturbation becomes large. This is because the theory is linear in which the perturbation of solute and thermal fields are related linearly to the amplitude of interface perturbation. As Sekerka[22] points out, where the amplitudes become large, the linear analysis becomes inapplicable. For this reason, calculations of the time evolution of the perturbed interface using the linear theory do not represent any noteable improvement over the marginal stability analysis[22,23].

Introduction of non-linearity to the marginal stability analysis was done by Wollkind and Segel[24], and by Langer[25]. This has lead to more questions than it has answered. As Langer writes in his paper, his calculations for stable cells using non-linear analysis showed a lack of self-consistency as stationary solutions were not obtained.

2.3.2 Treatment of the cell problem

As mentioned in the introduction to this chapter, a complete picture of the physics of the cell problem was only given recently. However, there are, in the literature, several reports of treatments of some aspects of cellular growth.

Bolling and Tiller[26] attempted an approximate calculation of cell spacing as a function of growth parameters. The analysis of the diffusion problem was limited to a region near the cell tips. Local equilibrium was assumed at the tip and Gibbs-Thomson capillarity effect was included. Solutions to thermal and solute diffusion equations were obtained. Invoking the local equilibrium condition and mass balance at the interface, the interface shape was calculated near the tips and was found to be elliptical. The cell spacing was estimated as the lateral diffusion length ($\sqrt{Dt}$) where t is the time taken by the cell tips to advance, in the forward direction, a distance at which lateral solute field vanishes. Agreement with experiment was poor. A complete solution of the cell problem was not given. Their calculations contained a free variable in the solution. The authors discuss the need for an optimizing condition in order to obtain a unique solution and have favoured the use of maximum tip temperature as the optimizing principle.

Kramer et al.[8] considered the problem of solute segregation during cellular solidification, using dimensional arguments. Local equilibrium was assumed at the interface whose shape was taken as experimentally observed shape in decanted samples. The effective distribution coefficient at the cell tip was found to approach the

equilibrium distribution coefficient at small values of $G_L/vC_o$ and unity at large values of $G_L/vC_o$, a trend seen in experimental observations.

Donaghey and Tiller[27] proposed a model for predicting equilibrium cell spacing and solute distribution. Assuming a simplified interface shape, the solute diffusion equation in the liquid was solved using methods of fourier analysis. In this analysis, the interface shape was assumed to be rectangular with near-planar groove walls. The diffusion equation was solved ahead of the tips and diffusion in the groove was represented in terms of a single parameter. The solution of the problem demanded an extra criterion and the ad hoc "maximum-intrusion criterion" was used. Applying this criterion, the tip temperature was maximised with respect to cell spacing. This yielded relations for the tip temperature and the cell spacing.

The model predicts that the cell spacing increases with decreasing velocity and alloy content and increasing temperature gradient. The experimental data was so scanty that it provided only two points for comparison with theory. The two points were in fair agreement with theory.

The defect of this model is that, in the interest of keeping the solution analytic, diffusion in the grooves was not considered and the assumed interface shape was unrealistic. The choice of maximum tip temperature as the optimizing criterion is without scientific basis.

Burden and Hunt[28] combined Trivedi's[29] solution for the isothermal growth of a paraboloidal crystal with the treatment of Bower et al.[30] of solute segregation during growth in a temperature gradient. Following Bower et al. and Sharp and Hellawell[31], zero

constitutional super cooling was assumed at the tip. Following the isothermal growth model, a radial solute gradient was introduced to satisfy mass balance conditions at the tip. A relationship was obtained between the tip temperature/concentration and tip curvature. Minimum tip undercooling was used as the optimizing criterion. The predictions indicate that the tip temperature first increases and then decreases with growth velocity. Correlation with experimentally measured tip temperature in Al-Cu alloys[11] was good despite the lack of justification for the assumptions used in the model.

Hillert[32] criticized the treatment of Burden and Hunt for not describing the transition from planar to cellular to dendritic mode of growth. He presented a new treatment which was purely formalistic and without physical justification. An assumption was made that a gradual transition exists between dendritic and planar growth. The tip temperature was written as a function of the tip radius of curvature to show such a transition. Optimization was done by invoking maximum tip temperature.

Jin and Purdy[33] advanced a theory for the steady-state controlled solidification of binary alloys. Local equilibrium was invoked at the interface. A solution of the solute diffusion equation in the liquid was obtained for an infinite paraboloidal dendrite. For arrays of dendrites, the solution was truncated at a self-consistent boundary condition behind the tip. Applying mass conservation at the tip, the tip concentration was obtained as a function of the tip curvature. To resolve this indeterminacy, Jin and Purdy followed Kirkaldy[34] and employed the criterion of minimum entropy production. Experiments

were conducted on an Fe-Ni alloy[12]. The theoretical predictions were in reasonable agreement with the experiment. The results showed that the tip concentration decreased rapidly with velocity in the low velocity regime and remained essentially independent of velocity at higher velocities. The tip concentration and the spacing decreased with increasing temperature gradient at constant velocity. The authors concluded that the use of zero constitutional supercooling and the maximum tip temperature criteria yielded results in strong disagreement with their experimental results.

As early as 1959, Kirkaldy[34] applied the principle of minimum rate of entropy production to the cellular growth problem. Using the formulation of Brown[35] and de Groot[36], he derived an expression for the entropy production rate for cellular growth. It was estimated that diffusion of solute supplies the dominant source of entropy production. The system would tend to minimize this entropy production by arranging the morphology in such a way as to conserve available energy through solute segregation. It was noted that the segregation, which occurs in cellular growth, is a direct manifestation of the system's attempt to minimize the entropy production.

Billia and Capella[37] followed Kirkaldy[34] in their analysis of cellular growth. Assuming a sinusoidal interface, the position of which is fixed by a condition that the mean interface temperature is the same as the equilibrium melting temperature of a planar interface, an attempt was made to calculate the entropy production as a function of the wavelength of the sinusoidal interface. Local equilibrium was assumed at the interface and the capillarity effects was ignored.

Diffusion in the solid was neglected. The composition profile in the solid far behind the interface was approximated by a cosine function with an amplitude equal to the maximum concentration difference in the experimentally determined profile. This was used to calculate the liquid composition at the interface and the solute profile in the liquid. The total entropy production was calculated and a minimum was obtained with respect to the wavelength of the interface. Comparison of calculations with the experimental data of Jin and Purdy[12] on Fe-8%Ni showed reasonable agreement between theory and experiment. Severe restrictions were placed on the interface in this model including the shape, which did not take into account the cell grooves, and the position of the interface was fixed a priori without any justification. As a result, the solutions that are obtained are suspect.

Billia et al.[38] have also used the Glansdorff-Prigogine general evolution criterion[39] which reduces to the minimum entropy production theorem when the Onsager reciprocity relations are relevant. For the same model described above, this criterion was applied. The scheme of calculation was similar to that described above. Again, severe restrictions were placed on the interface shape and position. Applying the criterion of minimum free energy of the growing solid for the same physical model yielded results which were within a factor of two of the experimental results[13].

In a recent contribution, Kirkaldy[40] showed that the cellular structure cannot be explained by a theory assuming equilibrium everywhere at the interface. This idea, which represents a departure from conventional, equilibrium propositions for cellular growth, forms the

basis on which this thesis is written and is discussed in detail in the following chapters. The main features of the contribution of Kirkaldy to the cell problem can be summed up as follows:

a) The cellular state is found in a kinetic phase space different than the marginally unstable states of the planar interface, and therefore is not tractable through continuum methods starting from the constitutional supercooling criterion. In fact, the kinetic state of stable cells is continuously accessible from an intial state with planar interface in which the solid is superheated. This virtual initial condition is shown in figure 3. b) The Capillarity effect is significant at the cell "cusps", on the solid side of the interface (figure 4). At all other sections on the interface, curvature is small and the capillarity effect is negligible.

c) Local equilibrium must apply at the cell tips and at the "cusp" when modified for the capillarity effect, as these portions of the interface are bound by irrational walls. d) The capillarity effect makes a positive addition to the equilibrium concentration at the "cusp". This effect, together with the large diffusion coefficient in the liquid and a linear temperature gradient and near-linear equilibrium liquidus line, necessarily puts the cell walls in a non-equilibrium condition such that the solid adjacent to the cell walls will be carried into superheat.

e) The cell walls are thus thermodynamically unstable with respect to melting and are only stabilizied by kinetic and crystallographic effects. f) The strong, positive capillarity effect at the "cusp" also demands that a trailing solute diffusion profile must develop in the solid. It is this diffusional flux in the solid resulting from

the capillarity effect which stabilizes the "cusp" and thus the cellular interface.

Kirkaldy points to the close relation between Widmanstätten ferrite in steels and the liquid region between the cells. He recognized the similarity between the two in terms of thermodynamics, kinetics and crystallography. In fact, from the virtual initial condition shown in figure 3, one would expect Widmanstätten growth of liquid into solid.

On the basis of the aforementioned model, an approximate mathematical analysis was carried out for the stable cell problem. A planar concentration profile in the liquid was assumed (lateral diffusion of solute neglected). Zero constitutional supercooling was assumed at the tip. Application of mass balance at the cusp, yielded a relation for the radius of curvature at the cusp, r, as

$$r = r(v,\Delta T)$$

where v is the velocity and $\Delta T$ is the temperature difference between the tip and the cusp. To solve this indeterminacy, a qualitative representation of the minimum entropy production theorem was employed. Minimum entropy production is equivalent to maximum stored available energy in the solid (minimum dissipation of free energy). This condition is obtained when the segregation of solute is maximum in the solid. This, in turn, corresponds to maximum capillarity effect at the "cusp" or to a minimum in the radius of curvature of the "cusp".

The optimization was carried out with respect to v keeping $\Delta T$ constant. Expressions were derived for the length of the cells, which varies with $v^{-1/2}$, and for the optimum radius of curvature.

A quasi-dimensional argument based on Scheil-Chipman segregation calculation yielded a relation for the spacing of cells.

The salient feature of the quantitative model is that, it predicts a region of supersaturation in which regular cells do not appear. This region lies between the region where the planar interface is stable and a region where stable cells occur.

A defect of the quantitative theory was to assume a planar solute concentration profile in the liquid. This is an oversimplification as it does not take into account the accumulation of solute in the cell grooves. An improvement on the quantitative aspect of the cell problem must begin with a detailed description of the solute field in the liquid in conformity with the boundary conditions.

However, for the first time a complete physical picture was given of the cell problem. This picture, which stems from an analysis of experimental observations made over several decades, marks a qualitative advance in our understanding of the cell problem and forms the basis of this thesis.

## 2.4 Concluding Remarks

(i) The constitutional supercooling criterion and the more rigorous perturbation analyses of marginal stability have greatly influenced research in this field. Extensions of these methods to describe stable cell growth have, however, been unsuccessful. There is an emerging consensus in the literature that the marginal stability of planar interface and stable cell growth are two distinct problems and therefore cannot be described by the same model.

(ii) It is a foregone conclusion in the literature that solutions to stable cell growth possess an inherent indeterminacy and therefore demand the use of an optimizing condition. A variety of such conditions have been proposed. The most widely used conditions are the maximum tip temperature condition and the minimum entropy production criterion. While the former is used purely from the reasoning of competitive growth, the latter has its foundations in the theory of irreversible thermodynamics and has a direct physical meaning within the cell problem.

(iii) Although experimental studies have been made for several decades, there is very little quantitative data on cell spacings and solute segregation. Much of the initial work was aimed at verifying the CS criterion. The more recent observations were mainly focussed on the condition at the cell tips only. Ample data exists, however, to show that the occurrence of cellular structure is related to the crystallographic orientation with respect to the growth direction.

# CHAPTER 3

# THEORY OF CELLULAR SOLIDIFICATION IN A BINARY ALLOY

## 3.1 Introduction

As was noted in the previous chapter, the outstanding problem in binary cellular solidification is to develop a quantitative theoretical model which describes the phenomenon of stable cell growth and is capable of predicting important aspects of cell growth such as the cell spacing and the solute segregation attending the process.

In this chapter, a quantitative model is developed based on the description of stable cell growth due to Kirkaldy[40].

## 3.2 The Physical Model

The problem taken up for solution in this work is the steady-state growth of cells in a binary alloy under the influence of a constant temperature gradient. The mathematical model is developed for the case of two-dimensional cells. The physics of the three-dimensional cell problem, with the hexagonal array of cells, is a trivial extension of the physics of the two-dimensional model and it is hoped that the mathematical model for the two-dimensional problem can be extended without undue complexity to the three-dimensional problem.

The model is based on the following assumptions:

a) Local equilibrium applies at the leading tip of the cells. As has been observed empirically[10-12,40] the radius of curvature at this tip is large so capillarity effects can be neglected. Local equilibrium is a reasonable assumption at this portion of the interface as it is curved and irrational, i.e., it does not lie along a particular crystallographic plane. One of the properties of such an interface is that it does not provide a significant kinetic barrier for motion[41] and therefore local equilibrium is applicable. The temperature and composition at this section of the interface are thus related through the phase diagram.

b) Local equilibrium applies at the root or trailing tip, modified by the capillarity effect. This is a short segment of the interface with a very small radius of curvature. The interface is irrational here also. One of the observations in our experiments, which will be described in later chapters, is that the root of the cellular interface is highly mobile compared with the other sections of the interface. Small perturbations around the steady-state, which create rather insignificant responses from the rest of the interface, are sufficient to make the root traverse up or down the temperature gradient with relative ease. This empirical observation contains more than a hint that local equilibrium assumption is valid at the root. Local equilibrium here is of course modified by capillarity and the composition in the liquid at the root is given by adding an extra term due to capillarity to the liquidus composition given by the phase diagram.

A corollary of this assumption is that the equilibrium partitioning ratio can be used to give the solid composition at the root. In other words, the solidus and the liquidus are shifted proportionately as one traverses along the pressure coordinate.

c) The temperature gradient in the solid and in the liquid are the same. This condition is attained in laboratory experiments by keeping the sample in a much larger thermal environment with a fixed temperature gradient, for example, using a massive container of larger thermal conductivity to hold the sample. Under such a condition, the evolution of the latent heat of fusion at the solid-liquid interface and the difference in the thermal conductivities of the solid and the liquid have a negligible effect on the thermal field in the sample. The advantage resulting from this condition is that the heat transfer problem has been eliminated and the calculations are simplified. This condition has been used by all of the authors whose work was described in the previous chapter.

As discussed by Kirkaldy[40] and in the previous chapter, these conditions yield a solute profile as shown in figure 4. In relation to the phase diagram given in figure 5 the liquid composition at the root is given by $X_2$, which represents the local equilibrium composition in the liquid including the capillarity correction. The composition in the liquid at the tip is given by the equilibrium value $X_1$ at the tip temperature $T_1$. In this model, we have rejected the use of the "no-constitutional-supercooling-ahead-of-the-celltip" condition. This condition has been applied widely in the literature. When this condition is assumed, a severe restriction is placed on the solute profile

in the liquid. This condition not only fixes the tip concentration, but also the concentration gradient at the tip, and so it is an unjustified restriction placed on the system. The local equilibrium assumption at the tip and at the root yield the solid composition at the interface for these points as $X_{1S}$ and $X_{2S}$.

The region over which capillarity applies at the root is of the order of the radius of curvature at the root. Empirically this radius is very small -- at least two orders of magnitude smaller than the length of the cells. Since diffusion in the liquid is fast, it cannot support an extreme amount of concentration gradient such as would be necessary to account for dropping the entire condribution due to capillarity within a distance equal to the radius of curvature at the root. In other words, the concentration profile in the liquid must fall along a smooth curve from $X_2$ to $X_1$. With hindsight, the concentration profile follows the solid curve along the line B-B and the dashed curve along A-A. These profiles are of course calculated exactly as a part of the solution.

Under these conditions it is impossible to maintain local equilibrium along the cell walls. As indicated in the phase diagram, at least a part of the cell walls are superheated. It is our presumption that the cell walls are stabilized by kinetic effects. The experimental observations of Chalmers and Winegard and co-workers described in the previous chapter show clearly that the cells are obtained at particular crystallographic directions. We shall return to this non-equilibrium nature of cell walls in later sections.

The solute distribution in the solid behind the interface would follow along a line from $X_{2S}$ to $X_{1S}$. Due to the non-equilibrium nature of the interface along the walls a simple relation between the interface liquid composition and the interface solid composition does not exist so the two compositions must be related by a mass balance condition at the interface. This leads us to another assumption made in this model. Diffusion in the solid is neglected everywhere except in the vicinity of the root. Behind the root, capillarity and local equilibrium establish a steep concentration gradient in the solid. Because of the high gradient here, the solute flux in the solid is appreciable and must be included in the local mass balance condition at the root. Also, this solute flow in the solid is essential to stabilize this section of the interface. Without the capillary effect at the root, with the associated solute flux in the solid, the build-up of "superheat" in the solid would cause the liquid "spike" to penetrate into the solid to an infinite distance. It is the solid diffusional flux which dissipates the supersaturation built up in this region and stabilizes the root of the interface.

With the model described above, it is now possible to set up the diffusion problem and specify the boundary conditions.

## 3.3 Statement of the Problem

With heat transfer eliminated from the problem, the cell growth is controlled by solute diffusion and interface kinetics. No attempt is made here to solve the interface kinetics problem and it is assumed that kinetic effects stabilize the non-equilibrium cell walls.

Thus the problem is to solve the solute diffusion equation in the liquid subject to the boundary conditions, which are:

a) local equilibrium at the tip

b) local equilibrium at the root modified by capillarity

c) local mass balance at the interface

d) overall solute balance

e) starting liquid composition far away from the interface

The aim is to solve the diffusion equation to obtain the solute profile in the liquid, the solute profile in the solid, the interface position (temperature), the spacing, the length and the root radius of curvature. We note from all the previous work that an internal degree of freedom is to be expected which is to be resolved by using an optimization condition.

Because of the symmetry of the geometry, it is adequate to solve the diffusion problem in the liquid region between two cells (Figure 6).

## 3.4 Mathematical Analysis

### 3.4.1 The diffusion equations

In the two dimensional cartesian coordinate system, the diffusion equation is written as

$$\frac{\partial c}{\partial t} = D\left(\frac{\partial^2 c}{du^2} + \frac{\partial^2 c}{\partial y^2}\right) \tag{3.1}$$

where c is the concentration of diffusing component in moles per unit volume, t is the time, u and y are fixed cartesian coordinates. Taking

c to be proportional to mole fraction X, we can write (4.1) in terms of X as

$$\frac{\partial X}{\partial t} = D\left(\frac{\partial^2 X}{\partial u^2} + \frac{\partial^2 X}{\partial y^2}\right) \tag{3.2}$$

For constant growth velocity, v, in the u-direction, substitution of $x = u - vt$ into (3.2) gives

$$D\left(\frac{\partial^2 X}{\partial x^2} + \frac{\partial^2 X}{\partial y^2}\right) + v\,\frac{\partial X}{\partial x} = 0 \tag{3.3}$$

where now (x,y) is the cartesian coordinate system with a frame of reference moving at a velocity v in the positive u direction.

The solution to equation (3.3) can be obtained by the method of separation of variables as given in appendix 1.

The intercellular liquid region is very narrow except near the tips. This fact together with the large diffusion coefficient in the liquid provides that the lateral solute profile must be flat in the narrow liquid "groove" far behind the cell tips. In line with this and with reference to figure 6, we can write that for $x<0$, the solute profile must become one dimensional for large negative values of x for which the width of the liquid "groove" is very small. We can split the general solution into two parts, one applying for positive values of x and the other for negative values of x, with the condition that the two equations should give the same concentration value as well as the same concentration gradient at $x=0$. This is done in section 3.4.3. The position of $x=0$, or the distance $x_o$, must also be determined.

3.4.2 Boundary Conditions

With reference to figure 6, the following boundary conditions can be written.

a) as x approaches infinity, the liquid composition must approach $X_0$, the alloy solute content.

$$X(\infty,y) = x_0 \tag{3.4}$$

b) the lateral solute gradient must vanish at y = 0 and y = ±s. This is derived from the symmetry of the structure.

$$\frac{\partial X}{\partial y} = 0 \quad \text{for } y = 0 \text{ and } y = \pm s \tag{3.5}$$

c) local equilibrium at the tip. This condition yields two equations. From the phase diagram,

$$T_i = T_0 + mx_i \tag{3.6}$$

where $T_i$ is the temperature at the tip

$x_i$ is the liquid composition at the tip

$T_0$ is the melting point of pure solvent,

and m is the liquidus slope

The local equilibrium mass balance at the tip yields:

$$v(1-k)X_i = -D \left.\frac{\partial X}{\partial x}\right|_{tip} \tag{3.7}$$

where k is the equilibrium distribution coefficient

D is the alloy diffusion coefficient in the liquid.

We not that $\left.\frac{\partial X}{\partial y}\right|_{tip} = 0$ from equation (3.5).

d) local equilibrium condition at the root. This yields the following relation between the root temperature $T_2$, the root liquid composition $X_2$ and the radius of curvature at the root.

$$T_2 = T_0 + mx_2 + \frac{T_o \sigma b_o}{Hr} \tag{3.8}$$

where $\sigma$ is the interfacial energy

H is the latent heat of fusion

and $b_o$ is a numerical parameter ($b_o = 1$ for a cylinder, $b_o = 2$ for a sphere).

For the two dimensional cells, we can assume that the root geometry is cylindrical as shown in figure 7. Thus $b_o = 1$ in equation (3.8).

e) mass conservation at the root is written as

$$v(1-k)x_2 = -D \left.\frac{\partial X}{\partial x}\right|_{root} + D_s \frac{\Delta x_s}{a_o r} \tag{3.9}$$

where $\Delta X_s = k\Delta x_L$ (figure 5)

$\Delta X_L$ = capillary shift in the liquid = $\frac{\sigma V b_o}{RT_2 r(1-k)}$

$D_s$ is the solute diffusion coeffient in the solid and $a_o$ is a parameter equal to 2 for a cylinder[42].

The second term on the right hand side is the solute diffusion flux at the root and is written in the form of the well-known Zener-Hillert flux equation[42,40].

f) the experimental constraint is that the temperature difference between the root and the tip should be equal to the temperature gradient times the length of the cells.

$$T_1 - T_2 = G\ell \tag{3.10}$$

Equation (3.10) together with (3.6) and (3.8) yields one boundary condition.

g) the overall solute balance is an additional condition. This requires that the average composition of solid behind the interface be equal to $X_o$ at the steady-state. The condition is formally expressed as follows:

Ignoring diffusion in the solid, conservation of mass at the interface gives

$$v_{\hat{n}}(X_L - X_S) = -D \frac{\partial X}{\partial \hat{n}} \qquad (3.11)$$

where $\hat{n}$ is the normal vector to the interface

$v_{\hat{n}}$ is the normal interface velocity

$X_L$ is the liquid composition at the interface

$X_S$ is the solid composition at the interface

and $\frac{\partial x}{\partial \hat{n}}$ is the concentration gradient at the interface along $\hat{n}$. Since the model assumes that the cellular interface is non-equilibrium except at the tip and the root, no single phenomenological relation between $X_L$ and $X_S$ can be expressed. Therefore, condition (4.11) may be used only if the interface shape is "a priori" known. Otherwise $\hat{n}$ and $\frac{\partial x}{\partial \hat{n}}$ cannot be evaluated. Thus to make the analysis tractable and following other workers, we construct a parametric interface shape. From a study of the experimental interfaces it was concluded that the shape is approximately elliptical near the tip over a large range of velocities. Accordingly an ellipse of minor axis 2s and semi major axis $\ell$ which terminates in a semicircle of radius r was assumed as the interface shape (figure 7). Mathematically, in reference to

figure 6, $x_i$ and $y_i$ (interface coordinates) are given as

$$(x_i + (\ell - x_o) - r)^2 + y_i^2 = y^2; \quad o < y < r \tag{3.12}$$

and

$$\left(\frac{x_i + \ell - x_o - r}{\ell - r}\right) + \left(\frac{s - y_i}{s - r}\right)^2 = 1; \quad r < y < s \tag{3.13}$$

From figure 8 we can write

$$v_{\hat{n}} = v \sin \theta \tag{3.14}$$

and

$$\frac{\partial x}{\partial \hat{n}} = \frac{\partial x}{\partial x} \sin \theta + \frac{\partial x}{\partial y} \cos\theta \tag{3.15}$$

at the interface. We can also write

$$\tan \theta = \frac{dy_i}{dx_i} \tag{3.16}$$

Using equations (3.13) to (3.16) and (3.11), it is possible to obtain $X_s$ from a knowledge of the diffusion solution in the liquid. Assuming no diffusion in the solid, except near the root, we can equate the solid composition far behind the interface to the solid composition at the interface for the same value of y. Thus we obtain $X_s$ as a function of y. Behind the root, the solid composition at the interface is obtained from the local equilibrium condition as

$$X_s = kX_2; \quad o < y < r \tag{3.17}$$

The overall solute balance can now be written with the use of the symmetry of the structure, as

$$\int_o^s X_s dy = sX_o \tag{3.18}$$

with $X_s$ given by (3.17) and (3.11).

3.4.3 The Solution of Fick's Equation

The general solution is given in appendix 1. For $x < 0$, we note that the equation

$$x = x_o + A_o + b\,\ell\exp(-\nu x/D) + \sum_{n=1}^{\infty} An\,\exp(\mu_n x)\cos \lambda n\, y \qquad (3.19)$$

satisfies the condition that as x becomes large negative, the solute profile becomes one-dimensional and satisfies the condition (3.5). For $x > 0$, the equation

$$x = x_o + B_o \exp(-vx/D) + \Sigma\, B_n \exp(-\eta_n x)\cos \lambda_n y \qquad (3.20)$$

satisfies the boundary condition at $x = \infty$ for $y = 0$ and $y = \pm s$.

The two equations should give the same values of X and $\partial X/\partial x$ at $x = 0$. In appendix 2, these two profiles are matched at $x = 0$ and expressions are obtained for the Fourier coefficients in (3.19) and (3.20).

The various coefficients in equation (3.19) and (3.20) are functions of s, $y_o$, $A_o$ and b. The problem is to use the boundary conditions to solve for these four variables as well as for $x_o$, the length of the cell and the radius of curvature at the root. Thus we have a total of seven unknowns which we must evaluate. $x_o$ and $y_o$ are related by the shape equation (3.13). This reduces the number of unknowns to six. Equations (3.7), (3.9), (3.10) and (3.18) provide four equations relating the six variables. Thus we are left with two degrees of freedom. To obtain a unique solution,

we must find two further constraints.

3.4.4 Optimization

As mentioned in the previous section, the problem has two internal degrees of freedom. To resolve this free boundary problem we look to the thermodynamics of irreversible processes to identify additional constraints to be imposed on the system.

Following Kirkaldy[34,40] and Jin and Purdy[33] we conjecture that the principle of minimum rate of entropy production applies to the stability point in cellular solidification. Theorems of Kirkaldy[43] and Tykodi[44], applicable to the quasi-steady variational pathways considered here, appear to have the necessary generality. As concluded in Chapter 2, this principle has a corollory within the cell problem which has to do with the solute profile obtained in the solid. Minimum entropy production is equivalent to maximum rate of storage of free energy[34]. The stored free energy in the product, namely the solid, should approach a maximum as the solute segregation becomes increasingly singular. Within the present model, the solute is "pumped" into the solid at the root of the interface due to the capillarity effect. As the radius of curvature decreases at the root, the capillarity effect increases and the intensity of solute "pumped" into the solid at the root increases, yielding a more singular segregation profile and thus a higher free energy stand. Thus, we surmise that the free energy associated with segregation

in the solid is a maximum and the entropy production rate is a minimum when the radius of curvature at the root is a minimum. We must admit at this point that the correspondence has not been rigourously demonstrated.

In any case, optimization is achieved here by minimizing the radius of curvature at the root. Since we have two degrees of freedom the optimization must be carried out in a two-dimensional field; firstly a local optimization is found in which the radius is minimized with respect to the length of the cells at fixed spacing, secondly, a refined optimum radius is sought with respect to the spacing of the cells. It is this latter optmization which was previously explored by Billia and Capilla[37]. We shall return to a discussion of this optimization in chapter 5.

### 3.4.5 Computer Solution Technique

Due to the complexity of the boundary conditions a completely analytical solution is not possible. The equations given in appendix 3 must therefore be solved using numerical techniques. The following algorithum was used.

a) Assume a value for the spacing s

b) Assume a value for the length $\ell$

c) Using the four boundary conditions solve for $(x_o, y_o)$, $A_o$, b and r

d) Change the length and repeat (c)

e) Repeat (d) until a minimum is found in the radius $(r_{opt})$

f) Change s, repeat (b) to (e)

g) Repeat (f) until a minimum $r_{min}$ is found.

## 3.5 Results

Calculations were carried out with the primary aim of making comparisons with the experimental results reported in the present study. The calculations were therefore focussed on the succinonitrile-salol system. The material parameters used in the calculations are listed in Table 3.

### 3.5.1 Results of the Optimization

The radius of curvature at the root showed a minimum with respect to the length for a given spacing. Figure 9 shows r as a function of $\ell$ for the specified growth conditions. As the length was decreased below the optimum value, the radius increased rapidly and for every value of s, there was a cut off at the short length side below which the four boundary conditions were not satisfiable.

Figure 10 shows the dependence of $r_{opt}$ as the spacing. Again a minimum was obtained. The stable solution is taken at the minimum $r_{opt}$ value on the $r_{opt}$ - s curve.

$r_{min}$ did not vary significantly with $X_o$ in the range of $0.002 < X_o < 0.05$ or with G in the range of $50 < G < 100$ k/cm. However, it depended on the velocity as indicated in figure 11. At very low velocities, the value of $r_{min}$ increased rapidly accompanied by a decrease in the capillarity effect. Below a critical velocity, a solution could not be obtained as the four boundary conditions

did not yield a convergent solution for $(x_o, y_o)$, r, $A_o$ and b. At this limit, $r_{min}$ had such a large value as to yield a capillarity effect of less than 2%. This critical velocity increased with decreasing $x_o$ and G had no noticeable effect on the critical velocity. Figure 12 shows the dependence of the critical velocity on $X_o$.

### 3.5.2 Prediction of Spacing and Length

The spacing and length were taken as the values which yielded the minimum in the radius of curvature. Figures 13, 14 and 15 show the calculated spacings as functions of velocity for different alloy compositions and temperature gradients. Cell spacing was found to decrease with increase in velocity. As the temperature gradient increased, the spacing decreased. The effect of incrasing the alloy content was to decrease the spacing.

Figures 16 and 17 show the length of the cells as a function of velocity for different alloy contents and temperature gradients. The cell lengths were found to decrease with increasing velocity, increasing temperature gradient and decreasing alloy content.

### 3.5.3 Solute Profiles

Figure 18 shows the variation of tip concentration in the liquid as a function of velocity. As velocity increased the tip concentration decreased. The decrease was large at low velocities and small in the high velocity regime. The effect of the temperature gradient was to decrease the tip concentration as the gradient

decreased. Figure 19 shows that the tip temperature increased with increasing velocity becoming progressively flat.

Figure 20 shows the variation of root composition and figure 21 the root temperature as functions of growth velocity. The root composition increases with increase in velocity and is relatively independent of temperature gradient. The root temperature increases as velocity increases.

Figure 22 shows the calculated composition profiles in the liquid. It can be seen that the profile becomes two-dimensional at a distance behind the tips approximately equal to the spacing of the cells. The same profile when plotted on the phase diagram, in figure 23, shows that along the cell wall the liquid is super cooled for nearly half the length of a cell behind the tip; the rest of the cell retains super-heat at the solid-liquid interface. As the velocity is increased the extent of supercooling increases. This suggests that at large velocities when the supercooling becomes large, the cell walls must break down behind the tip giving rise to dendritic side-branches.

In figure 24 is plotted the calculated solute profile in the solid. As velocity increases the peak height increases and the tip composition in the solid decreases.

These results are discussed further in chapter 5, and where possible, they have been compared with the experimental results.

# CHAPTER 4

# EXPERIMENTAL STUDY OF CELLULAR SOLIDIFICATION IN THE SUCCINONITRILE-SALOL SYSTEM

## 4.1 Introduction

The purpose of the experimental study was to further our understanding of the origin of cells and their steady-state morphology and to establish quantitative relationships between cell spacing and the various growth parameters such as velocity, alloy content and temperature gradient. The ultimate aim is of course to verify the theoretical model for stable cell growth presented in the previous chapter.

## 4.2 Choice of the System

As mentioned in chapter 2, the difficulty in experimenting with metals is that the observations must be made by interrupting the solidification process and sectioning the solidified metal. Jackson and Hunt pioneered work on in-situ observation of solidification interfaces in transparent organic compounds which freeze like metals.

In our work direct observation of the cellular interface was selected over the "post-mortem" method required for metallic systems. The key reason for this choice was that for verification of the new physical model presented by Kirkaldy and expanded in this thesis, it was necessary to observe the behaviour of the true solidification interface at different growth conditions. Of particular importance

was the response of the interface to perturbations about the steady-state. It is also possible to make accurate spacing measurements on the transparent systems. There is a drawback, however, in that it is extremely difficult to measure the concentration profiles in such samples.

A variety of transparent systems which model metals are available for study. Table 1 lists some of these. The succino nitrile (SN)-salol system was chosen, on the basis of the following considerations:

a) SN and salol are easily purified by conventional techniques such as partial crystallization and zone refining.

b) Both materials have very low vapour pressures in the temperature range used in the experiments. Table 2 contains vapour pressure data on salol. In the absence of such data for SN, a simple experiment was conducted in which a sample of SN was kept at its melting point for two hours in an ampule similar to the one used in the experiments in a $N_2$ atmosphere and the weight change was observed to be less than 0.05%. The low vapour pressure assures very little loss of material during melting, handling and alloy making and a high accuracy.

c) SN is the best characterised organic compound used in solidification studies. Wulff and Westrum[45], have provided thermodynamic data including the enthalpy of fusion, entropy of fusion and specific heat data. Schaefer et al[46], Jones[47] and Jones and Chadwick[48] have measured the thermal conductivities of solid and liquid as well

as the solid-liquid interfacial energy. Table 3 lists all the relevant data on SN.

## 4.3 Material Preparation

### 4.3.1 Purification

Since the investigation concerns the effect of binary alloying component on cellular solidification, it is necessary to start with pure materials and to add controlled amounts of the alloying component. SN and Salol are commercially available at a purity level of 98%.

All of the melting and handling of SN was carried out in a nitrogen atmosphere. Wulff and Westrum[45] have reported that contamination of SN is not measurable in a nitrogen atmosphere. As received SN, supplies by Messers. Eastman Co, was melted and partially frozen. The remenant liquid was filtered through a coarse glass frit using vacuum. The solid left behind was used as the raw material for further purification by zone-refining[49].

The vertical zone refiner consisted of a mounting which could travel up or down a threaded shaft driven by a constant r.p.m. motor through a worm-and-gear attachment. The speed could be changed by changing to a shaft with a different pitch. Two sets of resistance heating coils were attached to the mounting. These provided two liquid zones in the sample for each pass of the coils along the sample.

SN, partially purified by fractional crystallization, was melted and poured into a glass tube of 9 m.m. inner diameter and 50 c.m. length. This tube was sealed and placed in the zone refiner.

A schematic arrangement of the set-up is shown in figure 26. The coils were moved up at a rate of 2 μm per second. After 40 passes of the liquid zone, the sample was removed and halved. The melting points of samples from the top half and the bottom half were measured. The bottom sample showed an increase in the melting point over the initial sample from 56.4°C to 57.8°C. The top half showed a decrease in the melting point of 1.2°C to 55.2°C. This test showed that the impurities in the sample were segregating to the top end and have a distribution coefficient of less than unity. The bottom half of the sample was used as the starting material for further zone refining. After another 40 passes of the zone through the sample, the sample was halved again and the melting point of the bottom half was measured. The zone refining process was continued until the melting point was 58.08°C or more. This corresponds to a purity of >99.999% as determined from the well-known thermodynamic relation for the depression of the freezing point of a dilute binary alloy described in section 4.4. Typically, this required 150 passes. The method used for measuring the melting point is described in section 4.4.

Salol was purified by repeating the partial freezing procedure several times followed by zone refining. Zone refining was continued until a melting point of 42.8°C was reached.

4.3.2 Alloy Preparation

Alloys were prepared by adding liquid salol to a pre-weighed

liquid SN sample and mixing in a nitrogen atmosphere. The alloy was quickly frozen and weighed again to determine the composition of the alloy. The samples were then used in phase diagram determination and in solidification experiments. To ensure maximum accuracy, the lag time between alloy preparation and the experiment was minimized.

## 4.4 Determination of the SN-rich Side of the Phase Diagram

To test the quantitative aspect of the cellular growth model described earlier, it is necessary to have thermodynamic information such as the liquidus slope and the alloy partition ratio between the solid and the liquid. Due to the unavailability of these thermodynamic data on the present system, it was decided to measure the phase diagrams experimentally at the SN-rich side.

Thermal analysis was used as the technique for determining the liquidus and solidus temperatures of prepared alloys. Temperature changes were noted using a platinum-resistance-thermometer. The schematic arrangement is shown in figure 27. A constant current of 100 μA was passed through a calibrated thermometer supplied by Omega Engineering Co. and the voltage across the thermometer was plotted on a recorder. In the range of temperatures at which the experiments were carried out, this amounted to a power input of less than 1.25 μW. From the data provided by the supplier, the error in temperature measurement due to self-heating of the elements is less than 0.001 K. The recorder itself was calibrated using a standard 100 Ω resistance.

An electrical resistance furnace was used for thermal analysis. The sample was kept in an austenitic stainless steel block in order to provide uniform temperature throughout the sample. The furnace coil was wound up to the top of the furnace to provide a temperature gradient of less than 2 K/cm along the length of the thermometer. This was done to reduce error in temperature measurement due to conduction of heat along the thermometer sheath.

The sample was heated to 5 K above the melting point and the furnace was switched off. The natural cooling rates were between 1 and 2°C/min. The potential difference across the thermometer was measured to an accuracy of 0.001 mV. This corresponds to an error of ±0.03 K in the temperature.

The trace of a typical cooling curve is shown in figure 28. The absence of a sharp thermal arrest in the cooling curve presented some difficulty in establishing the freezing point. The procedure followed is indicated in figure 28. The two upper segments of the curve were extrapolated and their intersection at point O was taken as the equilibrium liquidus temperature. The lower two segments were unreliable as a measure of the solidus location because of possible segregation in the liquid at later times.

To measure the solidus temperature the sample was remelted, stirred and frozen quickly by immersing the container in a mixture of dry ice and methyl alcohol. This sample was kept in the furnace and heated at a rate of 2°-3°C/min. and the heating curve was plotted. Following a similar procedure to the one explained above, the

solidus temperature was determined. The change in slope was more gradual in the heating curve and so the uncertainty in the solidus temperature is expected to be greater than that in the liquidus temperature.

The liquidus and solidus temperatures were measured for various alloy compositions and the experimental results are plotted in figure 29. In drawing the liquidus line, the experimental points which showed a large scatter at the low temperature side were discarded and a best fit was done among the other points. Some of the points were observed to lie above the liquidus line. This could be due to the error introduced in establishing the arrest temperature. Similarly the best fit was made for the solidus points.

The following thermodynamic check was conducted on the experimental measurements. We can represent equilibrium solidification of a binary alloy into one solid phase by means of the following two equations:

Component 1 in liquid = component 1 in solid

Component 2 in liquid = component 2 in solid

and write the equilibrium constants for these two reactions[52] as

$$k_1 = \frac{a_1^s}{a_1^\ell} \quad \text{and}$$

$$k_2 = \frac{a_2^s}{a_2^\ell} ,$$

and the a's represent the appropriate activities. For a dilute solution, application of Raoult's law to component 1 (solvent) gives

$$k_1 = \frac{N_1^s}{N_1^\ell} = \frac{(1-N_2^s)}{(1-N_2^\ell)} \tag{4.1}$$

where the N's are the mole fractions. Choosing a standard state for component 2, the solute, such that $a_2$ approaches $N_2$ as $N_2$ approaches zero in each phase, and applying Henry's law to the solute, at the dilute solution limit, we get

$$k_2 = \frac{N_2^s}{N_2^\ell} \tag{4.2}$$

From equations (4.1) and (4.2), we can write[52], for $N_2 \ll 1$,

$$\ell n\ k_1 \cong - N_2^\ell(1-k_2)$$

Inserting this into van't Hoff's relation,

$$\frac{d\ \ell n\ k}{dT} = \frac{\Delta H}{RT^2}$$

(where $\Delta H$ is the heat of fusion and T is the temperature) and integrating from pure component 1 ($N_2$=0) we get

$$N_2^\ell \cong \frac{\Delta H\ \Delta T}{RT_m^2(1-k_2)} \tag{4.3}$$

where $T_m$ is the melting point of pure solvent and $\Delta T$ is the depression of melting point when the molefraction of solute in the liquid is $N_2^\ell$. Using $N_2^\ell$ and $\Delta T$ values from the liquidus measurements, we obtain from (4.3), $k_2$ = 0.21.

The dashed solidus line was drawn with a value of distribution coefficient of 0.21 as calculated above. The measured solidus temperatures were consistently lower than that given by the theoretical

line. This could be due to an error in the thermodynamic parameters used in the calculation.

## 4.5 Experimental Set-up

There are several reports in the literature of methods for direct observation of the solidification interface in transparent systems. Hunt, Jackson and Brown[53] and Jones[54] have described their experimental arrangements for this purpose. The present experimental set-up is similar to that used by Hunt et al.

### 4.5.1 Microscope Stage

A stage was constructed to conduct solidification experiments on their samples, under an optical microscope. The stage consists of essentially a hot plate and a cold brass plate separated by a distance which can be varied. The sample in the form of a thin film sandwiched between two glass plates, can be located on the stage. A temperature gradient is established in the glass container and in the sample in the gap between the hot and cold plates. Adjustment of the temperatures of the two plates keeps the solid-liquid interface in the gap. Locating this gap in the optical path of a microscope, the solid-liquid interface is viewed directly.

Figure 30 shows the microscope stage arrangement. The cold plate was cooled by passing water through the tube brazed on to it. By controlling the water temperature, it is possible to closely control the cold plate temperature. Two cylindrical elements are used to heat the hot plate; its temperature is controlled by the power input into

the elements. The gap between the two plates could be adjusted by moving them in a groove in the teflon sidings. The sample is held on the stage by a teflon sample holder and in direct contact with the hot and cold plates. Sample movement was achieved by connecting the teflon slide holder to a commercial linear drive mechanisms, which consists of a 100 r.p.m. synchronous motor and a 30 step parallel shaft gear box. With this set-up it was possible to obtain speeds in the range of 0.08 μm/s to 1283 μm/s with a ratio of 1.4 to 1 between adjacent rates. The drive mechanism was calibrated using a graduated slide in the teflon holder. The temperatures of the hot and cold plates were measured by spot welding thermocouples on to the plates. Microscope slides were placed on grooves in the sidings above the sample and below the hot and cold plates to minimize air currents over the sample.

4.5.2 Sample Preparation

The samples used in solidification experiments were prepared by placing a small quantity of molten alloy on a cleaned and dried cover glass slid of dimensions 22 x 30 x 0.3 mm. This was quickly covered by an identical glass slide and the liquid was frozen. It was then sealed on three sides with resin. A schematic diagram of the sample is shown in figure 31. In solidification experiments the unsealed side of the sample was always kept in contact with the cold plate and so was sealed with the solid. The sample thickness varied from 40 μm to 100 μm. In some of the samples, three of 25 μm chromel-alumel thermocouples were placed and these were used to measure the

temperature profiles in the stage.

4.5.3 Measurement of Temperature Gradient

When the sample is placed on the stage with one end in contact with the hot plate and another in contact with the cold plate, a temperature gradient is set up in the glass slide and in the sample. Since the hot and cold plates are much wider than the sample, and since the gap and the thickness of the entire sample is small, the heat flow in the sample and the glass holder in the gap can be considered as one-dimentional. Under these conditions, the ratio of parallel heat flux through the sample material and the glass slides may be estimated as $k_s\ t_s/k_G\ t_G$ where $k_s$ and $k_G$ are the thermal conductivities of the sample and of the glass, respectively, and $t_s$ and $t_G$ are the thicknesses of the sample and the glass.

For a sample thickness of 75 μm and with $k_G/k_s = 3.3$[47] and thickness of glass = 2 x 0.3 mm, the parallel heat flow through the sample is less than 4% of the total heat flow through the slides and the sample. As a result, it can be concluded that the heat flow through the glass slides controls the temperature profile in the gap. With the further assumption of constant thermal conductivity of glass in the temperature range involved the temperature profile in the gap may be considered linear. In fact, as shown in figure 32, the meausred profile is linear in the gap except very near the hot and cold plates.

Since the solidification experiments are at the steady-state in which the sample is moved over the stage at a fixed velocity, it is highly desirable to know the effect of sample movement on the

temperature profile in the sample in the gap. The following experiment was conducted to determine this effect empirically. A sample with thermocouples was placed on the stage and kept stationary for a period of 1 hour. This time is more than adequate for the sample to come to a steady-state, as confirmed by a stationary profile in the gap. The sample was then moved at a constant velocity towards the cold plate side. The output from the thermocouples was plotted. The same experiment was repeated at different velocities. The observations were as follows:

a) Up to a velocity of 120 μm/s, no change in the temperature gradient was observed. However, the profile was transposed towards the cold plate side at velocities in excess of 23 μm/s.

b) The extent of transposition varied with the velocity. It was not observable below 23 μm/s and at 120 μm/s, the temperature profile was transposed by ∿200 μm with respect to the profile in a stationary sample.

c) the temperature profile in the gap returned to stationary after approximately 5 seconds from the time the sample movement began.

d) No change in the profile was observed as the solid-liquid interface passed the thermocouples.

These empirical observations lead to the conclusion that the present experimental set-up is ideally suited for testing the quantitative aspects of the model, as well as permitting direct observation of the interface.

## 4.6 Experimental Procedure

The sample was placed on the stage with the unsealed end in contact with the cold plate. The temperatures of hot and cold plates were so chosen as to keep the interface in the field of view. The sample was kept stationary for a period of 1 hour to set up a steady temperature profile as well as to eliminate any segregation caused by previous solidification. The sample was then moved at a constant velocity towards the cold plate side. All measurements of spacing and length were made in the middle portion of the sample after the attainment of stable cells. The same procedure was repeated at other velocities.

## 4.7 Observations

### 4.7.1 Formation of Stable Cells

Initially, when the sample was kept stationary, the interface was planar as expected. As the sample was moved and solidification initiated the following qualitative observations were made.

We first summarize a series of observations at fixed alloy content and temperature gradient. At very low velocities the planar interface was stable. At slightly higher velocities, the planar interface became unstable. Near the margin, however, stable cells were not observed as the interface shape fluctuated until solidification was complete. These interfaces showed large radii of curvature at both the hot and cold ends of the sample. (see Figure 33). The root at the cold end is highly unstable, the perturbation length increasing and decreasing with time.

Above a certain velocity, the planar interface breaks down to a stable cellular interface. Even though the initial breakdown is similar to that at the sub-cellular velocites, as the transient stage develops, the root of the interface becomes sharper and a stationary interface is obtained at the steady-state. (Figure 34).

The critical velocity above which stable cells were obtained increases with decreasing alloy content and increasing temperature gradient. At very high velocities, the interface breaks down into a dendritic interface. (Figure 35).

4.7.2 Effect of Crystallographic Orientation

The breakdown of an interface described in the above section refers to changes occurring in a grain which is oriented such that the cell (and dendrite) axis is parallel to the growth direction. For grains which have their dendrite axis oriented slightly away from the growth direction, the same qualitative description is valid. But the cell to dendrite transition takes place at a lower velocity than for perfectly oriented grains.

When the dendrite axis is oriented farther away from the growth direction, stable cells were not obtained. The shape of these interfaces at intermediate velocities was interesting in that one side of the "cells" was smooth while the other side always showed dendritic perturbations. (Figure 36). At high velocities dendritic perturbations were seen on both sides.

4.7.3 Observations on Stable Cells

Quantitative observations in the present study were restricted to the stable cell morphology. All the measurements were made on cells whose axis was aligned along the growth direction. Since no seed crystals were used to obtain the required orientation it was necessary to repeat a procedure of melting the entire sample followed by directional freezing in the temperature gradient stage until grains with the desirable orientation were obtained. Then all the observations are made on this grain.

The interface was photographed after steady-state was reached. This was assumed to have occurred when the interface shape and position did not change with time. Spacing measurements were made on the photographs. Since the field of view of the recording instrument was restricted, it was not possible to make length measurements for all growth conditions as the cells were too long to be photographed at low velocities and temperature gradients.

The experimental variables under control were (i) the growth velocity, (ii) the alloy composition and (iii) the temperature gradient. The range in which the growth velocity could be varied was restricted at the lower end by the irregular to regular cell transition. As described in section 4.7.1, below certain transition velocity, regular cells were not obtained. At the higher velocity end, the cell-dendrite transition limited the range of observation. This range was found to be a function of the alloy composition and the temperature gradient.

In the ultra-pure SN, the cellular structure was not obtained at all. In this sample, there was a direct transition from the planar

to dendritic mode of growth. These dendrites, referred to as thermal dendrites in the literature, are characterized by a very sharp tip and their growth is considered to be controlled by heat transfer and/or interface kinetics. Clearly, this is not the focus of attention in this present work.

In the binary alloys, the cellular range was found to decrease with increasing alloy content. While stable cells were obtained at lower velocities as the alloy content was increased, the cell-dendrite transition velocity decreased rapidly. In the 0.5% alloy stable cells were observed from 5.3 μm/s to 122 μm/s at a gradient of 150°C/cm, while in the 5% alloy, the range was limited to 2.2 μm/s to 11.7 μm/s, at the same temperature gradient. The effect of temperature gradient on the cellular range was less dramatic. An increase in temperature gradient resulted in an increase in the lower limit to the velocity but it also increased the cell-dendrite transition velocity. For a 0.5% alloy, the cellular velocity range was between 5.3 to 122 μm/s at 150°C/cm while at 100°C/cm the range was from 3 to 62 μm/s.

Experimental observations were made at gradients of 50, 100 and 150 K/cm on alloys with composition ranging from 0.5% to 5% salol (0.19 to 1.95 mol %) in the cellular velocity range.

a) Effect of Velocity

Above a certain velocity, cell spacing decreased with increasing velocity as shown in figures 37, 38 and 39 for different gradients and compositions. At very low velocities, there was an increase in spacing as velocity increased in the more dilute alloys. Each data point in the figures refers to a particular run. As can be seen, the

reproducibility is very good.

The length of the cells decreased with increasing velocity. However, as mentioned earlier, it was only measureable at a gradient of 150 k/cm over the entire range of velocity. Figure 40 shows the variation of cell length with velocity.

b) Effect of Alloy Content

At a fixed growth velocity and a fixed temperature gradient, the spacing decreased with increasing alloy content in the range of alloy contents investigated. However, the functional dependence of spacing an alloy content was very weak as can be seen from figures 37, 38 and 39.

The length of the cells increased with increasing alloy content as shown in figure 40. The wavelength at which dendrite breakdown occurs is larger at the higher composition.

c) Effect of Temperature Gradient

Increase in temperature gradient gave rise to a decrease in spacing as can be seen from figures 37, 38 and 39. While the length of the cells was qualitatively observed to be strongly dependent on the gradient, quantitative measurements could only be made at one gradient, for reasons already discussed. (See figure 40).

4.7.4 Cell Shapes

The experimental cell shapes were approximately elliptical. Near the low velocity limit the cells became more rounded near the tip. Near the high velocity limit, the tip became sharper and the

cell shape approached that of a parabola.

## 4.8 Perturbation Experiments

Steady-state cells were perturbed to study the approach to steady-state from a perturbed state. The perturbation involved the introduction of a step change in velocity. The response of the system was to reach a new steady-state with a new spacing and length. The new spacing and length were found to be the same as would have been obtained in a steady-state experiment at the new velocity. In other words, the spacing and length of properly oriented cells have a unique value for a given velocity, alloy content and temperature gradient. Given sufficient time to attain the steady-state, the system attains this unique length and spacing irrespective of the initial conditions.

In our experimental set-up the smallest change in velocity that could be made was 40% of the original velocity. This change was sufficient to generate observable changes in spacing and length of the cells. For small perturbations, the change in length of the cells occurred continuously with most of the change evidenced in the root of the cells moving up or down the temperature gradient. For large perturbations, the reduction in length occurred both continuously and discontinuously by "pinching-off" of liquid droplets at the root of the interface. Figure 41 shows the "pinching off" phenomenon.

For large increase in velocity changes in spacing occurred by creation of a new cell. Grain boundaries were often the source of new

cells. At very large perturbations, splitting of the existing cells occurred leading to a decrease in spacing. Reduction in velocity led to overgrowth of cells yielding an increase in spacing.

When the spacing change is sufficiently small that it does not require the creation or elimination of a cell, it is accomplished by a different mechanism. The cell walls across the crystal develop small amplitude perturbations, as shown in figure 37, which drift along the interface to effect the change. Figure 42 shows a grain boundary with an unstable cell wall at the boundary. A similar mechanism was observed to operate to eliminate any local non-uniformity in spacing and to obtain a uniform spacing within the grain. The number of perturbation on the side wall depended on the magnitude of change in spacing, increasing with increase in spacing change. Figure 43 shows the sequence of events in eliminating a non-uniformity in spacing created by a perturbation in which the velocity was increased for a short time and brought back to its original value.

The major conclusion from the perturbation experiments is that the cells have mechanisms for changing the spacing discontinuously or continuously. The spacing and length have unique values determined by the growth conditions — alloy content, velocity and temperature gradient. This introduces a high confidence level in the spacing and length measurements as true steady-state values.

For small perturbations, the root of the cells respond quickly by moving up or down the temperature gradient. This indicates a high mobility for this part of the interface. Also, the changes in length which occur during the transient can be attributed mainly to the motion

of the root with respect to the rest of the interface and the length of the cells are primarily determined by the condition at the root.

## 4.9 Summary

The observations can be summarized as follows:

a) For a given set of growth conditions, there is a unique value for the spacing and the length of oriented cells. The system attains these values irrespective of the initial condition.

b) The cell spacing decreases with increase in velocity for a given alloy and temperature gradient. It increases as the temperature gradient decreases for a given alloy at a particular velocity. At the same growth conditions, spacing decreases with increase in alloy content in the range of compositions studied.

c) The length of the cells decrease with increasing temperature gradient, decreasing alloy composition and increasing velocity.

d) From the perturbation experiments, the root of the cells respond quickly to perturbations, indicating a high mobility for this portion of the interface.

# CHAPTER 5

# DISCUSSION

In this chapter some aspects of cellular solidification brought forward in the present work will be discussed both in respect to the theoretical model and in the light of the experimental observations. A comparison will be made between theoretical predictions and experimental observations on the spacing and the length of cells.

## 5.1 Comparison of Theory and Experiment

As mentioned in the previous chapter, a limitation of the system chosen for experimental study is that the concentration profiles are not measurable. On the other hand, the experiments were ideally suited for comparisons on spacing and lengths as the assumptions used in the model, such as a constant temperature gradient, were accurately satisfied in the experiment. Figure 44 shows the results of such a comparison of spacing in a 0.005% alloy for a temperature gradient of 100°C/cm. It is seen that the functional dependence is closely followed while the numerical value of calculated spacings is somewhat higher than observed. The reason for this discrepancy probably lies in the uncertainties in the material parameters and (or) the shape constraint imposed on the model. Indeed, it is seen that decreasing the solute diffusion coefficient in the liquid from $2 \times 10^{-5}$ $cm^2/s$ to $1 \times 10^{-5}$ $cm^2/s$ yields a better closure with experiment. Diffusion coefficients have not in fact been measured in this system. The value used in the calcu-

lation was guestimated by assuming that the diffusion coefficient is inversely proportional to viscosity and comparing the viscosity of this organic compound with that of metals. In any case, a factor of 2 in a diffusion coefficient is well within the range of uncertainty normally encountered in published diffusion data. Figures 45-49 show similar comparisons of the spacings for different growth conditions.

Comparison of lengths however showed a better numerical comparison as well as a better functional comparison. This is demonstrated in figures 50-51.

The observed spacing showed an anamolous behaviour in the low velocity regime, where the spacing increased with increasing velocity. This behaviour was not observed at an alloy content of 5%. The calculated spacings did not show such a behaviour. Also at the high velocity limit and high alloy contents, the spacing-velocity curve became flatter. This was also not predicted by the theoretical model. These discrepancies probably have their origin in the fact that the overall experimental shape actually changes at these velocity limits as discussed earlier, while in the calculations no provision is made for shape changes.

## 5.2 On the Optimization

The main observation from the experiments whereby the steady-state cells were perturbed by a step change in the velocity is that the immediate response was a change in length via the motion of the root up or down the temperature gradient, according as to whether the length decreased or increased. This was followed by slower spacing changes

during which the change in length was nominal. Unfortunately, the root radius in stable cells is too small to be observable. Nevertheless, the limited observations on the response of the cells to perturbations shed some light on the nature of the process. The initial response of the interface, which is to change the length to a new value at virtually the old spacing, indicates a local optimization at the root of the interface. The slower process of changing the spacing to a new steady-state value indicates a global optimum. Such a behaviour bears out the predictions of the theory whereby a local and a global optima are not only expected but also found in the solution. Indeed, the solution algorithm follows precisely the path followed by the system in response to the perturbation. A spacing and a length are input to the calculation as is the case when we step-change the velocity. A local optimum is first found with respect to the length and then the spacing is changed and a new optimum is found, etc., until the final solution is obtained. This observation provides a source of great confidence in the theoretical model presented.

## 5.3 Marginal Instability and Cellular Instability

At this juncture, it is appropriate to discuss the difference between marginal and cellular instability. We noted in chapter 2, that Kirkaldy[40] had brought to light the difference between the two states in terms of their detailed physics. His approximate mathematical analysis also showed that marginal instability solutions cannot be obtained from cellular solutions and vice versa, i.e., there is no path in the kinetic phase space connecting the two states. Such a

behaviour is also predicted by the present model. At very low velocities, as pointed out in the previous chapters, a theoretical solution does not exist. Furthermore, the experimental observations showed a region of velocities between the planar steady-state and the cellular steady-state in which a steady-state was not observed. Similar observations though less definitive, have been made in metallic systems, as reported in chapter 2. With the information we now have on this topic, we can say unequivocally that the equilibrium marginal stability theories are incapable of predicting the cellular solidification structures. In fact, as noted in chapter 2, the calculations of Langer[25] based on the local equilibrium approach did not produce stationary solutions. In the marginal stability analysis due to Mullins and Sekerka the perturbations either grew or they died.

## 5.4 What is New in this Contribution?

A quantitative model has been developed to describe the cellular instability in binary alloys. The theoretical model predicts the behaviour of cells to a high degree of accuracy.

The physics of the problem as originally presented by Kirkaldy[40] has been confirmed by experimental and theoretical analyses. By using a complete solution of the diffusion problem the defects of his approximate calculation have been removed. Specifically, the following improvements have been made.

a) The defect in assuming a one-dimensional term of solution was to provide improper mass balance conditions. With reference to equation 6 in reference 40, which is the local mass balance at the root,

subsitution of the one-dimensional form of solution (equation (1) in ref. 40), yields a diffusional flux in the solid towards the interface. Mathematically, the solution is given as

$$X = X_o + (X_2 - X_o)e^{-\frac{v}{D}X} \tag{5.1}$$

where X is measured from the root.

$$\left.\frac{dX}{dx}\right|_{root} = -\frac{v}{D}(x_2 - x_o) \tag{5.2}$$

Substitution of this into equation 6 of ref. 40, yields

$$v(1-k)X_2 = aD_s \frac{\Delta X_s}{r} + v(x_2 - x_o) \tag{5.3}$$

Rearranging (5.3)

$$aD_s \frac{\Delta X_s}{r} = v(X_o - kX_2) \tag{5.4}$$

In cellular solidification, where solute accumulates in the liquid "groove", the liquid composition at the root $x_2$ must be greater than $x_o/k$. Thus $kX_2 > X_o$. This suggests from equation (5.4) that the diffusional flux in the solid is positive which is to say that the flux is towards the interface. This is physically possible but appears inconsistent with intuition about the problem and our own more rigorous treatment. The origin of the defect lies in the approximate form of solution. Even though the liquid composition profile is one dimensional in the region from the root to nearly 80% of the length of the cells the effect of solute build-up at the front of the "groove" is to increase the non-exponential term to a value larger than $X_o$. In the

present solution this factor is $A_o$ and is calculated in the solution to be between 2 $X_o$ and 6 $X_o$ depending on the growth conditions. This provides for a more realistic mass balance at the root.

b) The crude assumption of zero-constitutional supercooling at the tip has been eliminated. This is given in ref. 40 as equation 3, which is

$$\left.\frac{dx}{dx}\right|_{tip} = -\frac{G}{m} \tag{5.5}$$

This led to another defect on the approximate analysis. Together with the local equilibrium assumption at the tip, this necessarily yielded the conclusion that the entire cell wall was superheated. This is evident from the construction in figure 4 of reference 40. In the present analysis this condition was relaxed and only local equilibrium at the tip was imposed. As can be seen from figure 5a it is still possible with this condition to get a solution in which the entire cell wall is superheated. However, as the stable solutions show in the calculations of Chapter 3, the solid or cool section of the cell wall is superheated while liquid or hot part of it is supercooled. While this does not drastically change the structure of the problem, the distribution of supersaturation is changed. The dendritic branching must now be regarded as the breakdown of the cell walls when the supersaturation which in this case is supercooling near the tip, increases. It also shows that nature is trying to balance the supersaturation in the solid and in the liquid, which is a kind of conditional free energy minimum.

## 5.5 More on the Non-equilibrium Cell Walls

The model predicts that the cell walls cannot be in equilibrium so it must be assumed that these are stabilized by kinetic effects. There is some evidence for this from the experimental observations. When the velocity is increased, we note that the supersaturation along the high temperature part of the walls increases so we expect a breakdown when the supersaturation exceeds a certain value. In fact, the experimental observation is that at large velocities the cell walls form dendritic perturbations. This course of events is self-evident for the supercooled section of the interface. We must now ask whether kinetic effects can adequately describe the greater stability of the superheated section of the interface? As Kirkaldy[40] points out this particular problem is analogous to the well-known Widmanstätten ferrite problem in which a needle-shaped precipitate of a phase with a large diffusion coefficient grows into a supersaturated medium of lower diffusion coefficient along a crystallographically well-defined direction. In this case, the walls of the "spike" are stabilized by kinetic and crystallographic effects. Drawing the analogy, we can state that a similar stabilization takes place here. Furthermore, Purdy[55] has shown that it is possible to have a stationary non-equilibrium interface on the basis of purely thermodynamic considerations. Referring to the free energy composition diagram of figure 52, when a liquid of composition $X_L$ is in contact with a solid of composition $X_s$ as indicated the two phases are not at equilibrium. From the tangent construction we can also see that the chemical potential of component 1 is lower in the

solid than in the liquid while the chemical potential of 2 is lower in the liquid than in the solid. Under these conditions, the interface cannot migrate if its movement is controlled by independent transfer of 1 and 2 across the interface.

# CHAPTER 6

## CONCLUSIONS

1) A quantitative model has been presented for the cell problem which describes the cellular instability with good accuracy.

2) Subject to an imposed realistic shape constraint the cellular problem has two degrees of freedom. It is thus necessary to apply two optimization conditions to obtain a unique solution. Experimental observations indeed indicate the presence of two optimizations -- a local one at the root of the interface and a global optimum.

3) The cell walls are non-equilibrium interfaces and are stabilized by kinetic and crystallographic effects. The supersaturation along the walls is roughly evenly distributed between the liquid and the solid.

4) Lateral diffusion effects extend to a distance behind the tips approximately equal to the spacing of the cells.

5) The spacing and the length decrease with increasing velocity. Spacing decreases with increasing temperature gradient and increasing alloy content in the range of investigation. The length increases with increasing alloy content and decreasing gradient. The functional dependencies are satisfactorily predicted by the model.

6) Marginal stability theories necessarily produce unstable solutions due to neglect of the non-equilibrium nature of the

interface and material and kinetic properties of the root of the interface.

7) The root of the cellular interface with its strong capillarity effect is a necessary element in the stabilization of the cellular interface. It defines a stable region of kinetic phase space which is not accessible to local equilibrium perturbation relaxations.

## APPENDIX 1

Substitution of $U = \dot{X} - X_o$ into (3.3) gives

$$D\left(\frac{\partial^2 U}{\partial x^2} + \frac{\partial^2 U}{\partial y^2}\right) + v\frac{\partial U}{\partial x} = 0 \qquad \text{(A1.1)}$$

Using the method of separation of variables, we write $U = \phi(x)\,\psi(y)$. Then,

$$\frac{\partial U}{\partial x} = \psi\frac{d\phi}{dx}$$

$$\frac{\partial^2 U}{\partial x^2} = \psi\frac{d^2\phi}{dx^2} \qquad \text{(A1.2)}$$

and

$$\frac{\partial^2 U}{\partial y^2} = \phi\frac{d^2\psi}{dy^2}$$

Substituting (A1.2) into (A1.1) and rearranging we obtain

$$\frac{1}{\phi}\frac{d^2\phi}{dx^2} + \frac{v}{D}\frac{1}{\phi}\frac{d\phi}{dx} = -\frac{1}{\psi}\frac{d^2\psi}{dy^2} \qquad \text{(A1.3)}$$

The LHS of (A1.3) is a function of x only and the RHS is a function of y only. Therefore, each must be equal to the same constant $\lambda^2$. Thus, we reduce the second order partial differential equation (A1.1) to two ordinary differential equations

$$\frac{d^2\phi}{dx^2} + \frac{v}{D}\frac{d\phi}{dx} - \lambda^2\phi = 0 \qquad \text{(A1.4)}$$

and

$$\frac{d^2\psi}{dy^2} + \lambda^2\psi = 0 \qquad \text{(A1.5)}$$

The solution of (A1.5) is

$$\psi = c_1 \sin \lambda y + C_2 \cos \lambda y \tag{A1.6}$$

The solution of (A1.4) is

$$\phi = c_3 \exp(-\eta x) + c_4 \exp(\mu x) \tag{A1.7}$$

where

$$\mu = \frac{1}{2} \left\{ \sqrt{\left(\frac{v}{D}\right)^2 + 4\lambda^2} - \frac{v}{D} \right\} \tag{A1.8}$$

and

$$\eta = \frac{1}{2} \left\{ \sqrt{\left(\frac{v}{D}\right)^2 + 4\lambda^2} + \frac{v}{D} \right\} \tag{A1.9}$$

Applying the boundary condition (3.5), we get

$$\frac{d\psi}{dy} = 0 \; ; \quad y = 0$$

$$\frac{d\psi}{dy} = 0 \; ; \quad y = \pm 5 \tag{A1.10}$$

Substitution of (A1.6) into (A1.10) gives

$$c_1 = 0$$

and

$$\lambda = \frac{n\pi}{5} \qquad n = 0,1,2,\ldots \tag{A1.11}$$

All integer values of n are permissible. Thus combining (A1.6) and (A1.7) and applying the principle of superposition of solutions we obtain the general solution of equation (3.3) as

$$X = X_o + \sum_{n=0}^{\infty} B_n \exp(-\eta_n x) \cos \lambda_n y + \sum_{n=0}^{\infty} A_n \exp(\mu_n x) \cos \lambda_n y \tag{A1.12}$$

We note that $\eta_o = \frac{v}{D}$ and $\mu_o = 0$. We also note that a particular solution of (3.3) is a special case of (A1.12) given by

$$X = X_o + b \exp(-vx/D) \qquad \text{(A1.13)}$$

## APPENDIX 2

AT $x = 0$, (3.19) gives

$$x(o,y) = x_o + A_o + b + \sum_{n=1}^{\infty} A_n \cos\lambda_n y \qquad (A2.1)$$

Eqn. (3.20) gives at $x = 0$

$$X(o,y) = x_o + B_o + \sum_{n=1}^{\infty} B_n \cos\lambda_n y \qquad (A2.2)$$

From (3.19),

$$\frac{\partial X}{\partial x}(o,y) = -\frac{v}{D} b + \Sigma A_n \mu_n \cos\lambda_n y \qquad (A2.3)$$

while from (3.20),

$$\frac{\partial X}{\partial x}(o,y) = -\frac{v}{D} B_o - \Sigma B_n \eta_n \cos\lambda_n y \qquad (A2.4)$$

At $x = 0$, the liquid domain ranges from $y = -y_o$ to $y = y_o$. Equating (A2.1) and (A2.2), we get

$$A_o + b + \Sigma A_n \cos\lambda_n y = B_o + \Sigma B_n \cos\lambda_n y \qquad (A2.5)$$

and equating (A2.3) and (A2.4), we get

$$-\frac{v}{D} b + \Sigma A_n \mu_n \cos\lambda_n y = -\frac{v}{D} B_o - \Sigma B_n \eta_n \cos\lambda_n y \qquad (A2.6)$$

Setting $A_n = B_n$, we obtain from (A2.5),

$$B_o = A_o + b \qquad (A2.7)$$

Substitution into (A2.6) yields

$$\frac{v}{D} A_o = -\Sigma A_n (\mu_n + \eta_n) \cos \lambda_n y \qquad \text{(A2.8)}$$

Expressing $\frac{v}{D} A_o$ as a Fourier Cosine series of the same period as the series on the RHS, in the domains $-y_o < y < y_o$, we get from (A2.8)

$$A_n = -2 \frac{v}{D} \frac{A_o \sin \lambda_n y_o}{(\mu_n + \eta_n) \lambda_n (S - y_o)} = B_n \qquad \text{(A2.9)}$$

REFERENCES


1. M. Buerger, Z. Kristallographie 89 (1934) 196.

2. R.B. Pond and S.W. Kessler, Trans. AIME 191 (1951) 1156.

3. J.W. Rutter and B. Chalmers, Can. J. Phys. 31 (1953) 15.

4. W.A. Tiller, K.A. Jackson, J.W. Rutter and B. Chalmers, Acta Met. 1, (1953) 428.

5. D. Walton, W.A. Tiller, J.W. Rutter and W.C. Winegard, Trans. AIME 203 (1955) 1023.

6. M. Herman and V. Camiano, Private Communication to G.F. Bolling and W.A. Tiller, Reference no. 24.

7. G.F. Bolling, W.A. Tiller and J.W. Rutter, Can. J. Phys. 34 (1956) 234.

8. J.J. Kramer, G.F. Bolling and W.A. Tiller, Trans. AIME, 227 (1963) 374.

9. L.R. Morris and W.C. Winegard, J. Crystal Growth, 5 (1969) 361.

10. R.M. Sharp and A. Hellawell, J. Crystal Growth 5 (1969) 155.

11. M.H. Burden and J.D. Hunt, J. Crystal Growth 22 (1974) 99.

12. I. Jin and G.R. Purdy, J. Crystal Growth 23 (1974) 37.

13. A.L. Coulet, B. Billia and L. Capella, J. Crystal Growth 51 (1981) 106.

14. G.A. Chadwick, Acta Met., 10 (1962) 1.

15. K.A. Jackson and J.H. Hunt, Acta Met., 13 (1965) 1212.

16. K.A. Jackson and J.D. Hunt, Bell Telephone Laboratories, Murray Hill, N.J.

17. M. Glicksman, in Solidification, American Society for Metals, Metals Park, OH., 1971.

18. R.J. Schaefer and M. Glicksman, in Modelling of Casting and Welding Process, Ed. by H. Brody and D. Apelian, AIME, Warrendale, PA 1981.

19. W.W. Mullins and R.F. Sekerka, J. App. Phys., 35 (1964) 444.

20. L.A. Tarshis and W.A. Tiller, in Crystal Growth, Proceedings of an International Conference on Crystal Growth, Boston, 1966, Pergamon Press, N.Y. (1967).

21. P.G. Shewman, Trans. AIME, 233 (1965) 736.

22. R.F. Sekerka, J. Phys. Chem. Solids, 28 (1967) 983.

23. D.P. Woodruff, The Solid-Liquid Interface, Cambridge, University Press, London, 1973.

24. D. Wollkind and L. Segel, Phil. Trans. R. Soc., 268 (1970) 351.

25. J.S. Langer, Rev. Mod. Phys., 52 (1980) 1.

26. G.F. Bolling and W.A. Tiller, J. App. Phys., 31 (1960) 2040.

27. L.F. Donaghey and W.A. Tiller, in The Solidification of Metals, Proceedings of a Conference on Crystal Growth held in Brighton.

28. M.H. Burden and J.D. Hunt, J. Crystal Growth, 22 (1974) 109.

29. R. Trivedi, Acta Met. 18 (1970) 287.

30. T. Bower, H. Brady and M.C. Flemings, Trans. AIME, 236 (1966) 624.

31. R.M. Sharp and A. Hellawell, J. Crystal Growth, 6 (1970) 253.

32. M. Hillert, in the Proceedings of the Conference on In-situ Composites III, Boston 1978 Materials Research Society.

33. I. Jin and G.R. Purdy, J. Crystal Growth 23 (1974) 29.

34. J.S. Kirkaldy, Can. J. of Phys. 37 (1959) 739.

35. W.B. Brown, Trans. Faraday Soc. 54 (1958) 772.

36. S.R. de Groot, Thermodynamics of Irreversible Processes North-Holland Pub. Co., Amsterdam 1952.

37. B. Billia and L. Capella, J. Crystal Growth, 44 (1978) 235.

38. B. Billia, H. Ahdout and L. Capella, J. Crystal Growth, 51 (1981) 81.

39. P. Glansdorff and I. Prigogine, Thermodynamic Theory of Structure Stability and Fluctuations, Wiley, N.Y. 1971.

40. J.S. Kirkaldy, Scripta Met., 14 (1980) 739.

41. W.A. Tiller, in Solidification, American Society for Metals, Metals Park, 1971.

42. M. Hillert, Jernkont. Ann., 141 (1957) 757.

43. J.S. Kirkaldy, Can. J. Phys.,

44. R.J. Tykodi, Thermodynamics of Steady States, The McMillan Company, 1967.

45. C.A. Wulff and E.F. Westrum, J. Phys. Chem., 67 (1963) 2376.

46. R.J. Schaefer, M.E. Glicksman and J.D. Ayers, Phil. Mag. 32 (1975) 725.

47. D.R.H. Jones, Phil. Mag., 27 (1973) 569.

48. D.R.H. Jones and G.A. Chadwick, Phil. Mag., 22 (1970) 291.

49. W.G. Pfann, Zone Melting, John Wiley and Sons, N.Y., 1958.

50. J.D. Ayers, R.J. Shaefer and M.E. Glicksman, Met. Trans., 7A (1976) 1747.

51. R.J. Corcoran, B.A.Sc. Thesis, University of Toronto, 1966.

52. L.S. Darken and R.W. Gurry, Physical Chemistry of Metals, McGraw-Hill Book Co., N.Y., 1953.

53. J.D. Hunt, K.A. Jackson and H. Brown, Rev. Sci. Inst., 37 (1966) 805.

54. D.R.H. Jones, Rev. Sci. Inst., 41 (1970) 1509.

55. G.R. Purdy, Private Communication, McMaster University, Hamilton, Ontario.

TABLE 1

| System | Reference # |
|---|---|
| Carbontetra bromide-hexachloroethane | 15 |
| Impure $CBr_4$ | 15,16 |
| Succino nitrile-camphor | 51 |
| Succinonitrile-salol | Present Study |

TABLE 2

Vapour Pressure Data on Salol[42]

| Vapour pr. in mm Hg | Temperature °C |
|---|---|
| 1 | 117.8 |
| 10 | 167 |
| 40 | 205 |

Melting point of salol 42.8°C

TABLE 3

Properties of Suceinonitrile

| | | Ref. |
|---|---|---|
| Molecular weight | 80.092 | 45 |
| Density of solid | 1.016 g/cc | 45 |
| Density of liquid | 0.988 g/cc | 18 |
| Solid-liquid surface tension | 8.9 $mJ/m^2$ | 46 |
| | 28 $mJ/m^2$ | 47 |
| Equilibrium melting point | 331.24 K | 50 |
| Latent heat of fusion | $4.78 \times 10^7$ $J/m^3$ | 45 |
| Entropy of fusion | $1.45 \times 10^5$ $J/m^3k$ | 45 |
| Thermal conductivity of solid | 0.225 J/mks | 46 |
| Thermal conductivity of liquid | 0.223 J/mks | 46 |

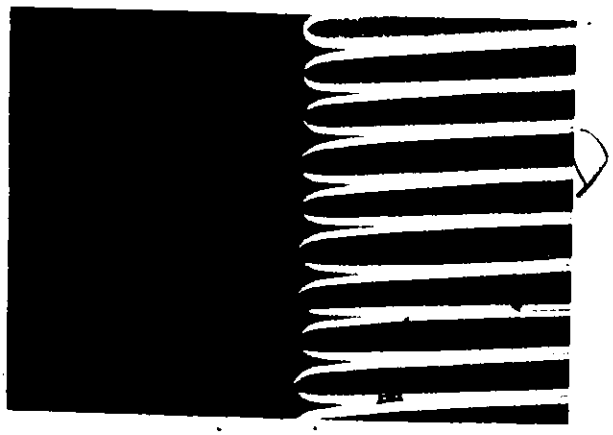

Fig. 1: Cellular solidification interface.

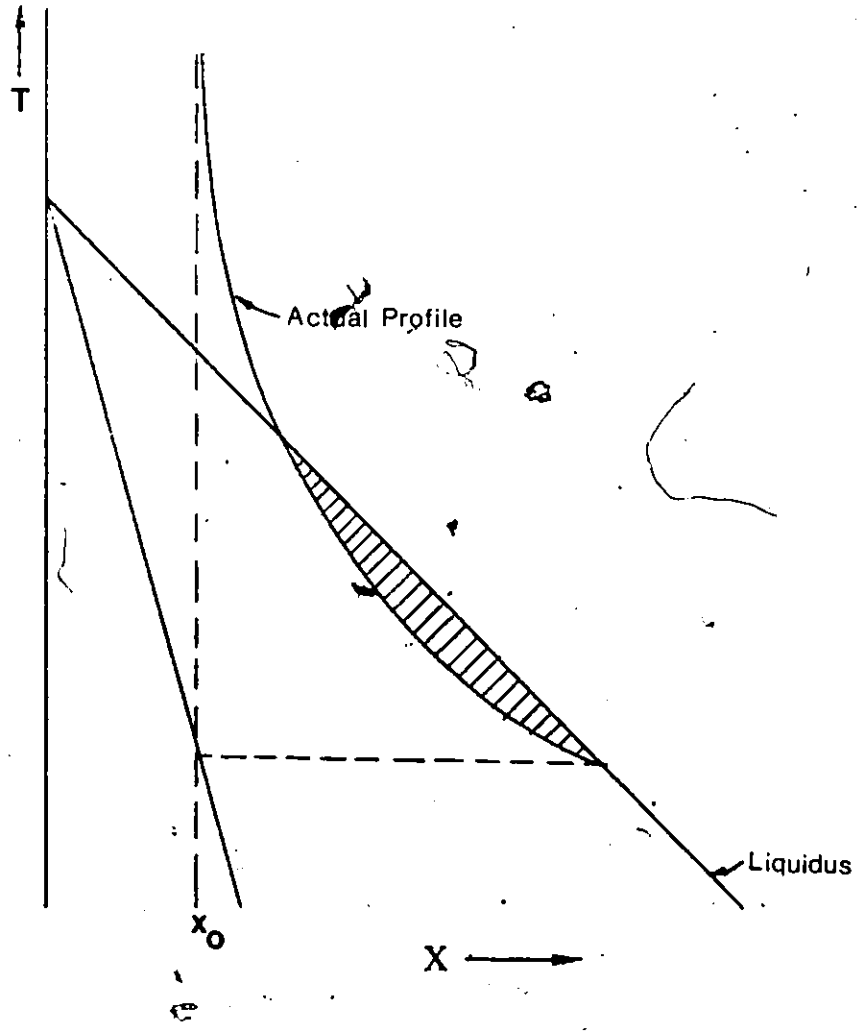


Fig. 2: Constitutional supercooling criterion. The shaded area indicates the supercooled region.

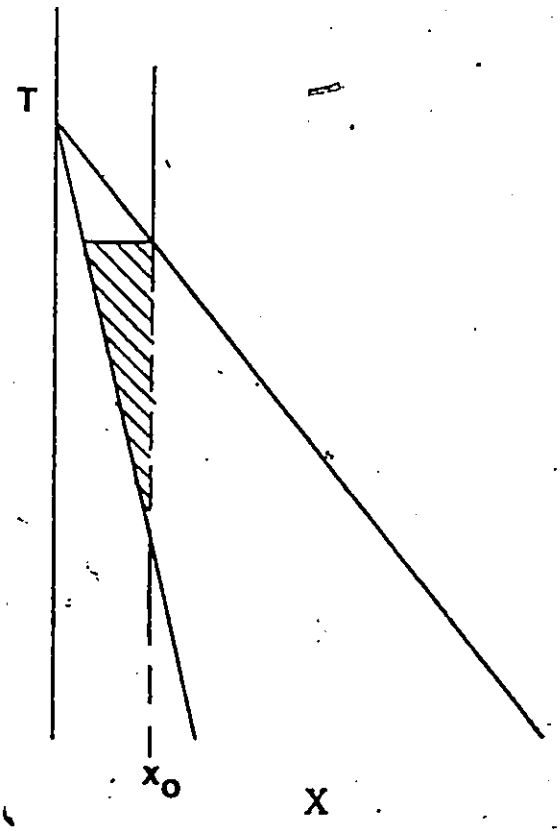


Fig. 3: Virtual supersaturated state for a solid liquid interface with superheated solid. After Kirkaldy[40].

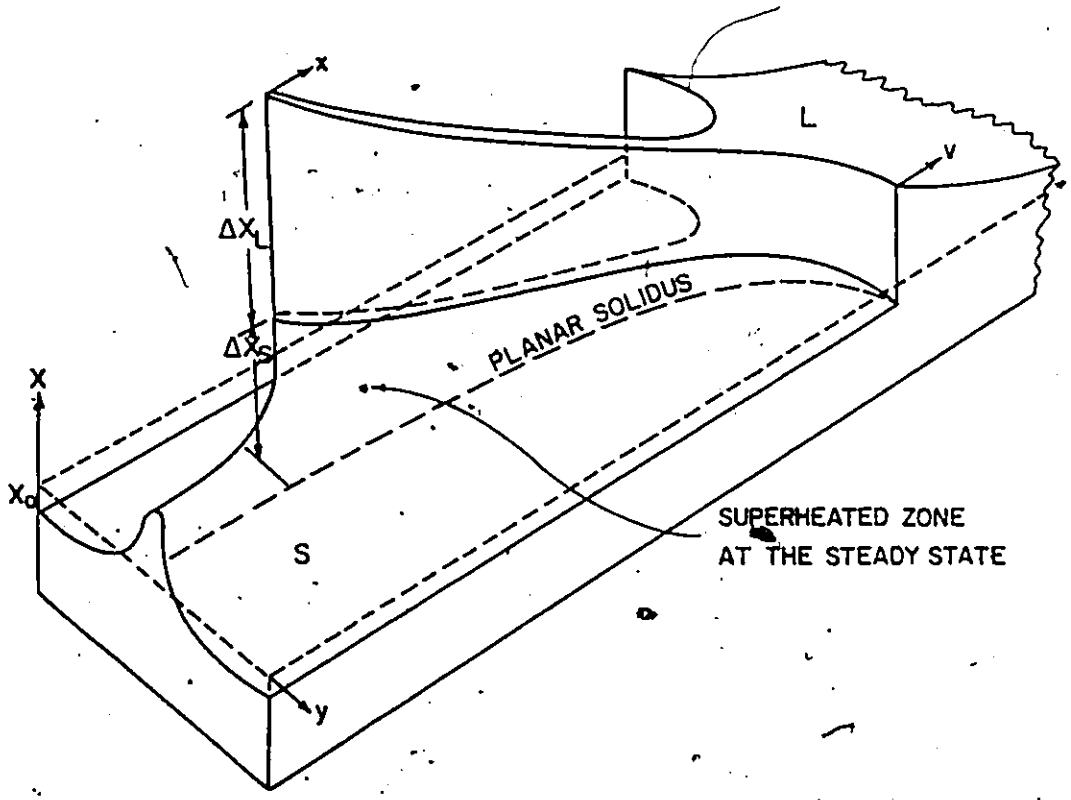


Fig. 4: Solid-liquid concentration distributions during steady-state. After Kirkaldy[40].

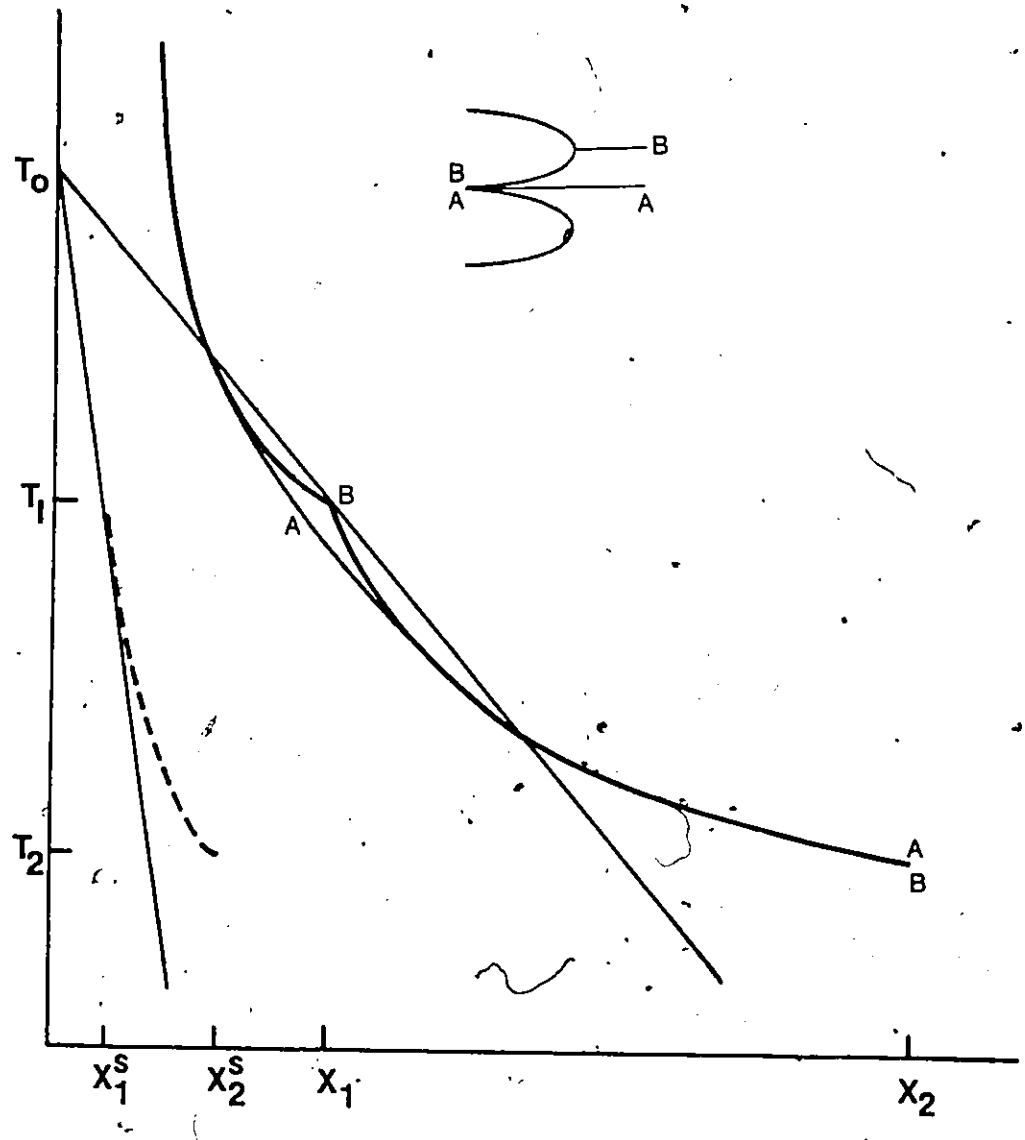


Fig. 5: Concentration distributions corresponding to the cellular steady state superposed on the phase diagram.

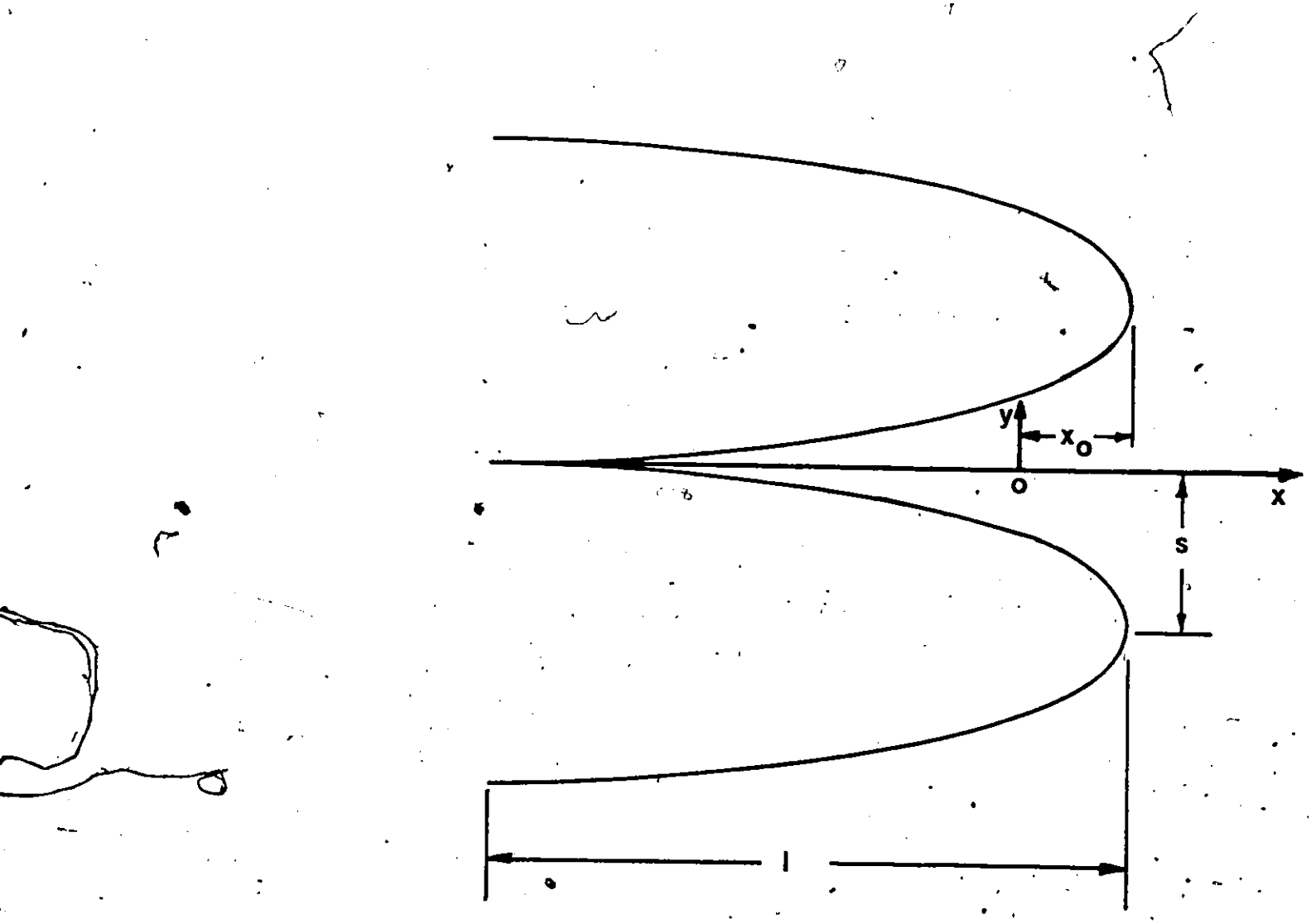


Fig. 6: Schematic cellular interface with the moving frame of reference.

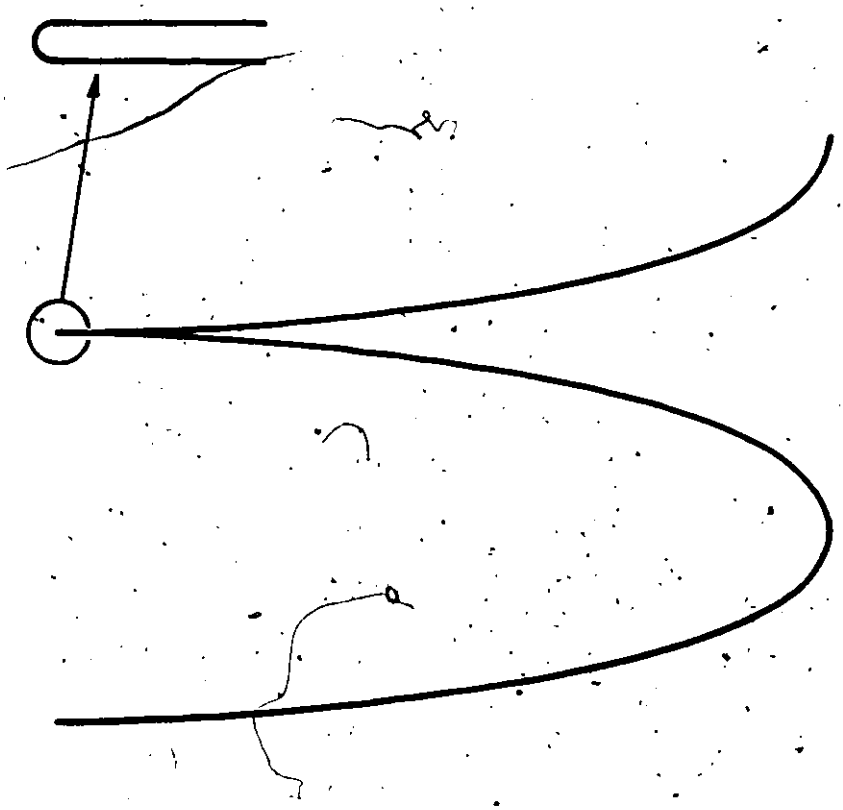

Fig. 7: Details of the interface shape used in the calculations.

Fig. 8: Cellular interface in a succinonitrile-salol alloy to show the relative magnitudes of the spacing and the root dimensions.

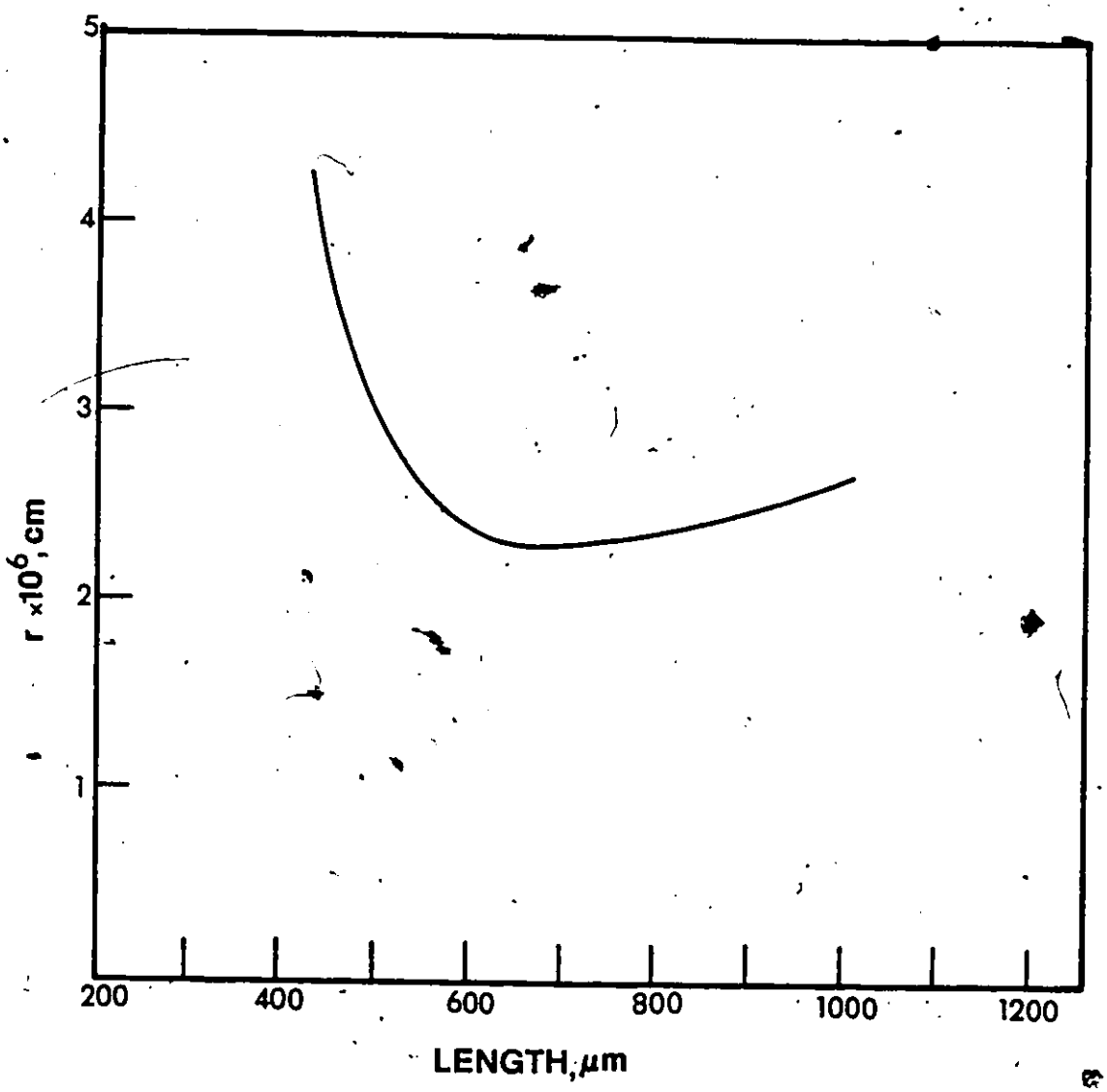


Fig. 9: Calculated root radius as a function of cell length at a cell spacing of 121 μm. Growth conditions are $X_o$ = 0.005, G = 100°C/cm, and v = 30 μm/s. The minimum in the curve gives the value of $r_{opt}$.

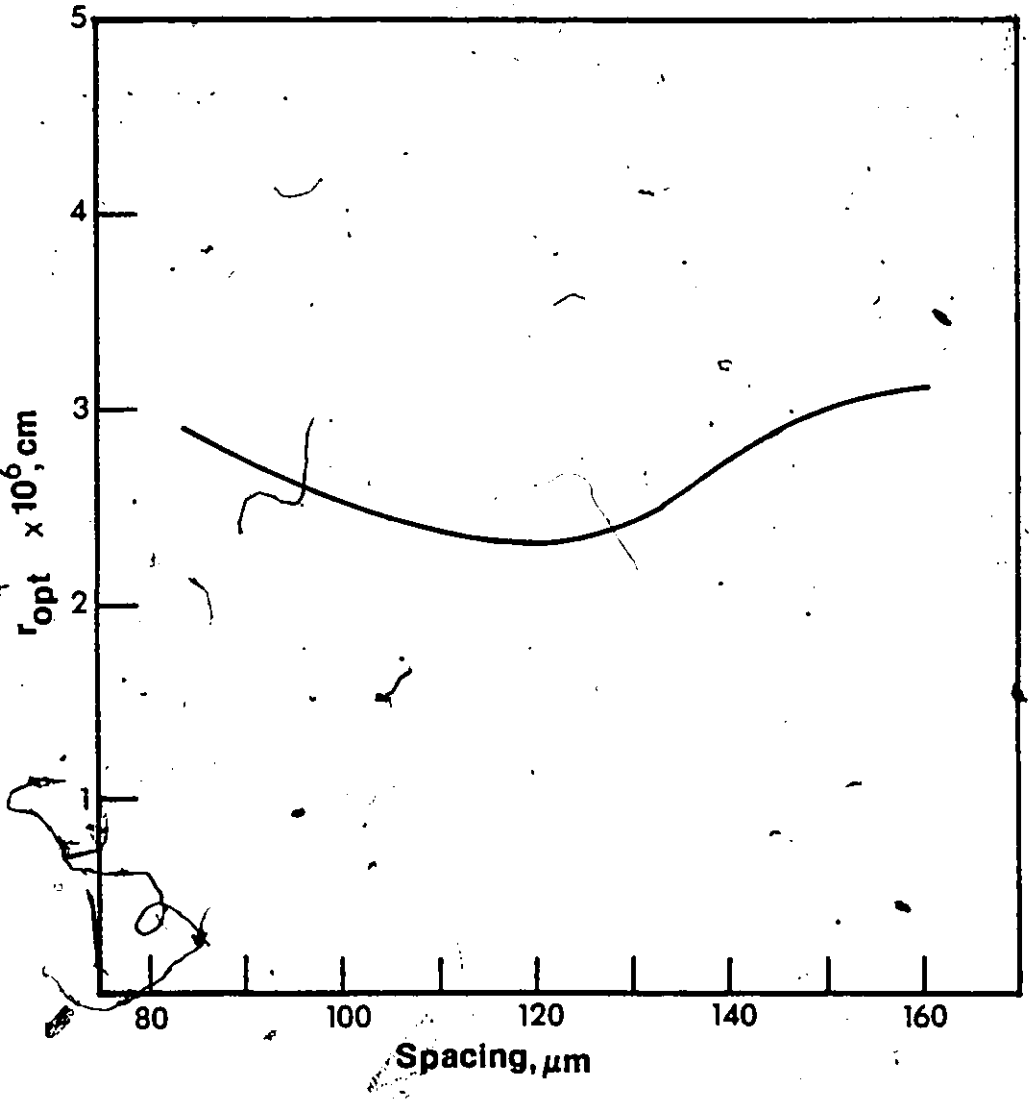


Fig. 10: Variation of $r_{opt}$ with cell spacing for the same growth conditions as in figure 9. The minimum value of the curve corresponds to $r_{nun}$. The stable solution is taken at this minimum.

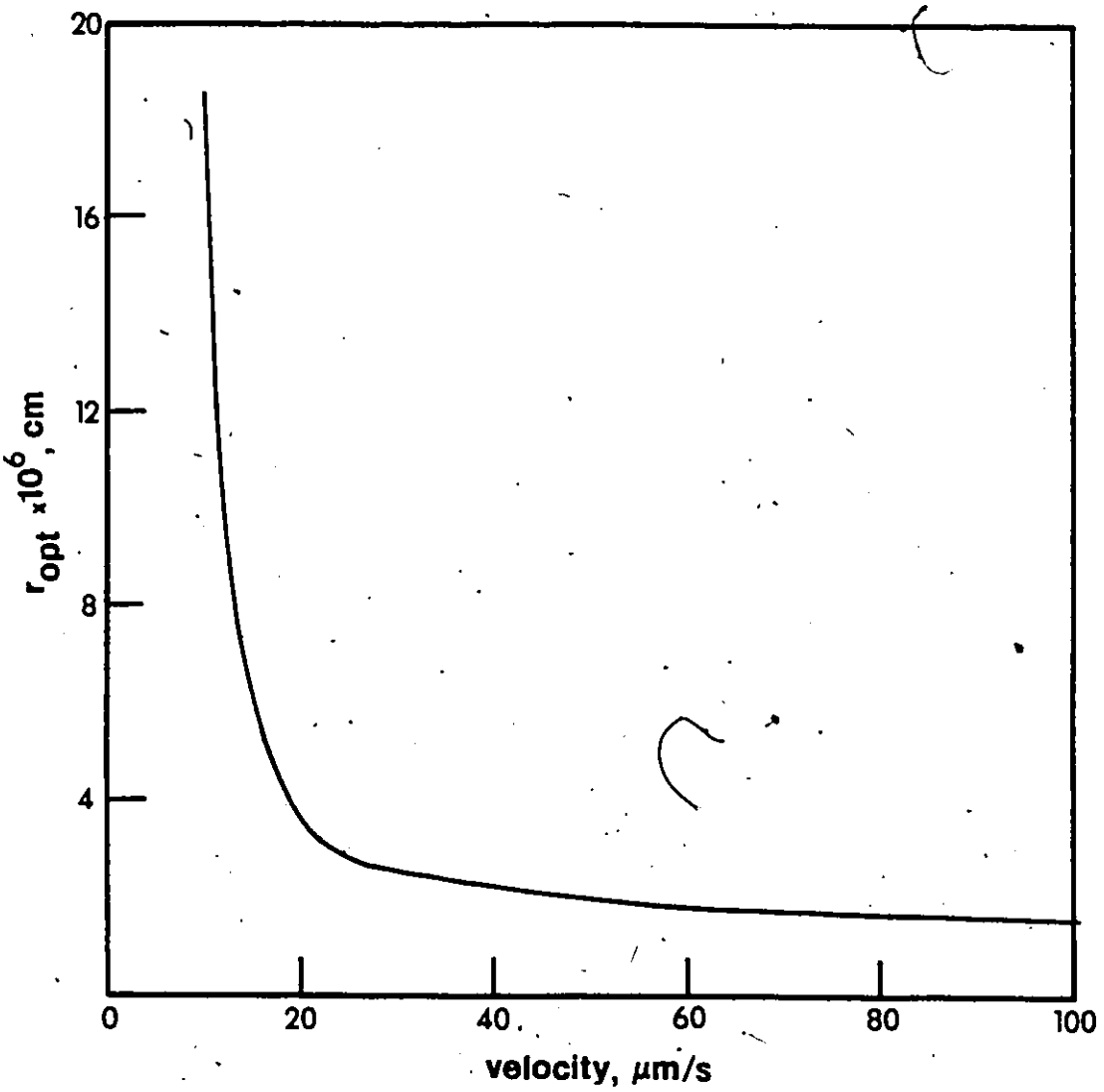


Fig. 11: Variation of $r_{nun}$ with the growth velocity for $X_o$ = 0.005 and G = 100°C/cm.

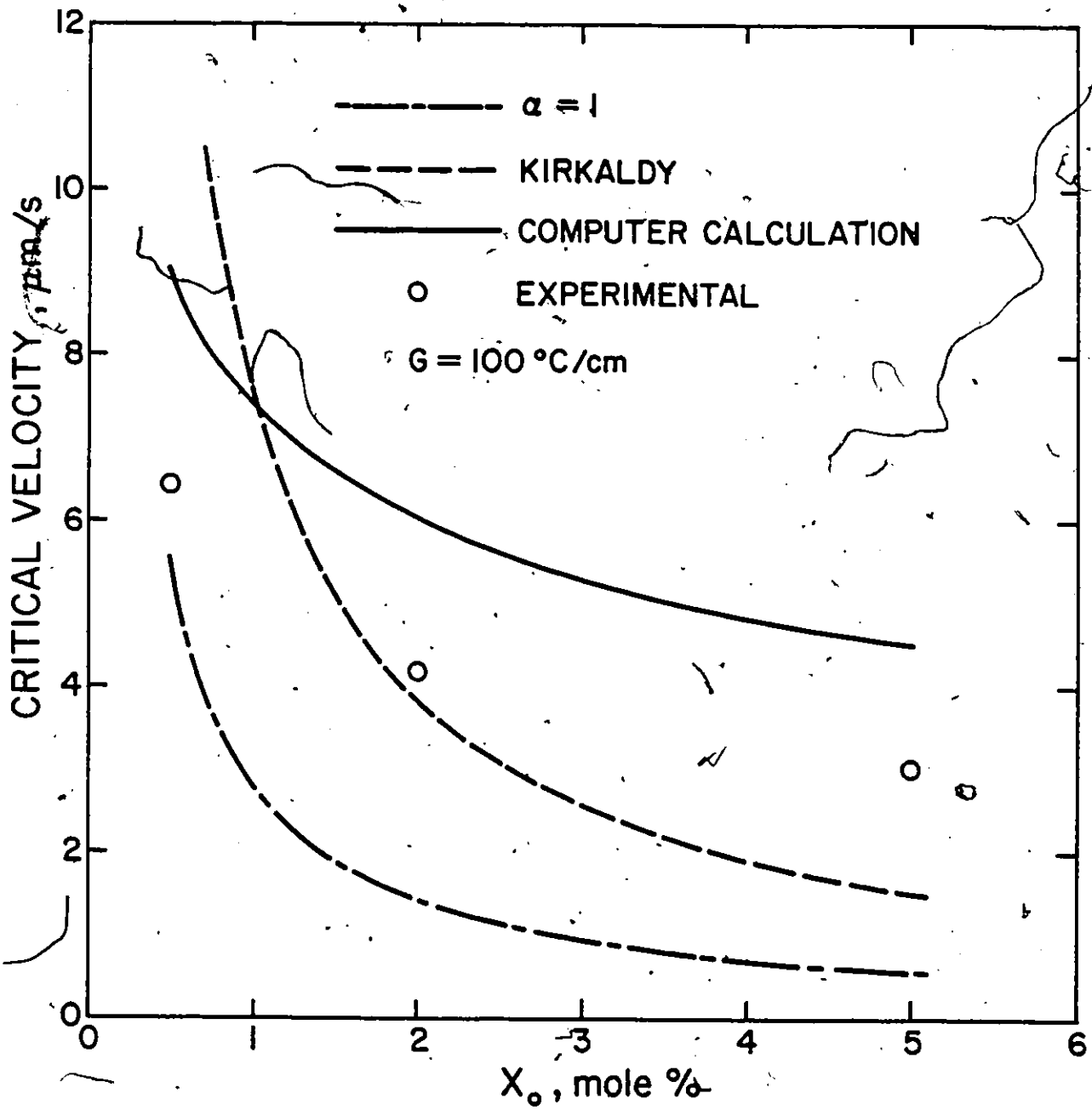


Fig. 12: The critical velocity for the onset of stable cells expressed as a function of alloy composition. The dash-dotted line is calculated from the CS criterion (Equation 2.1).. The dashed curve is from Kirkaldy[40] and the solid curve represents the present calculations. The experimental observations are plotted for comparison for (a) G = 100°C/cm, (b) G = 150°C/cm and (c) G = 50°C/cm.

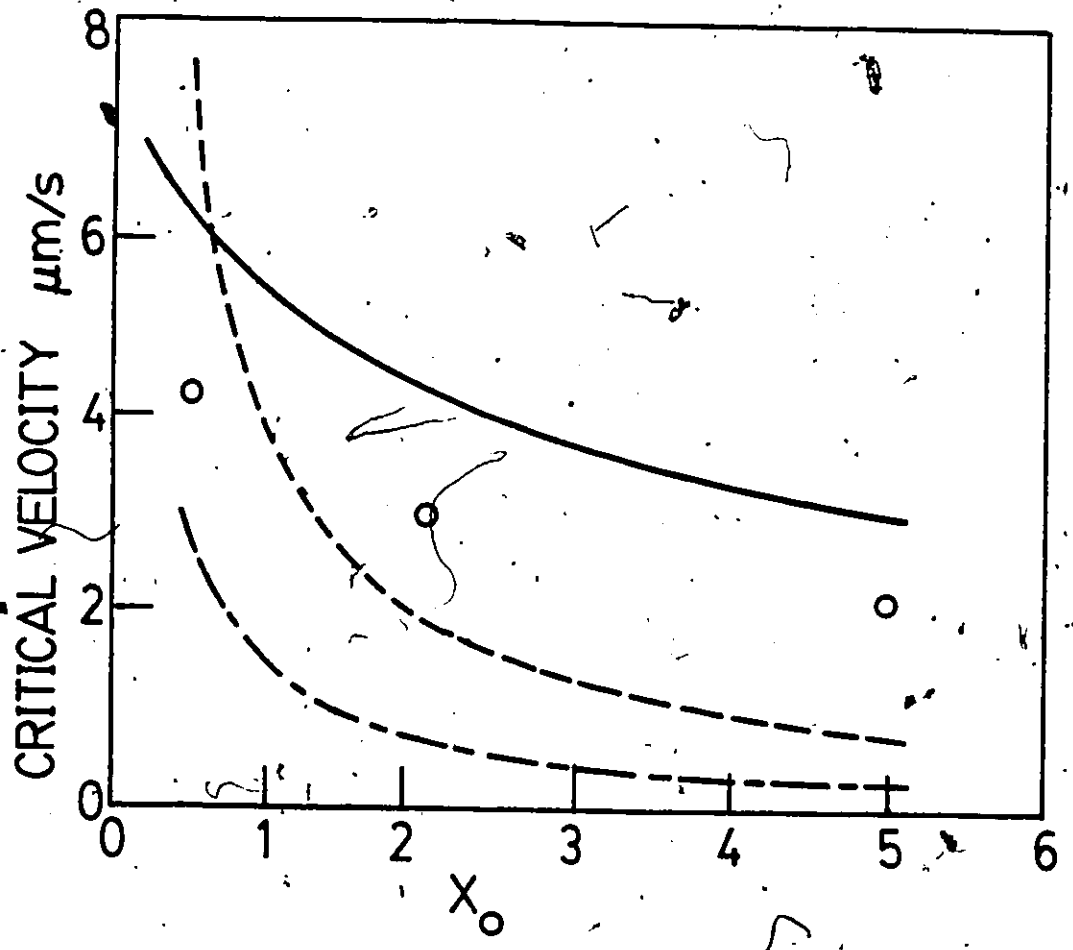


Fig. 12b

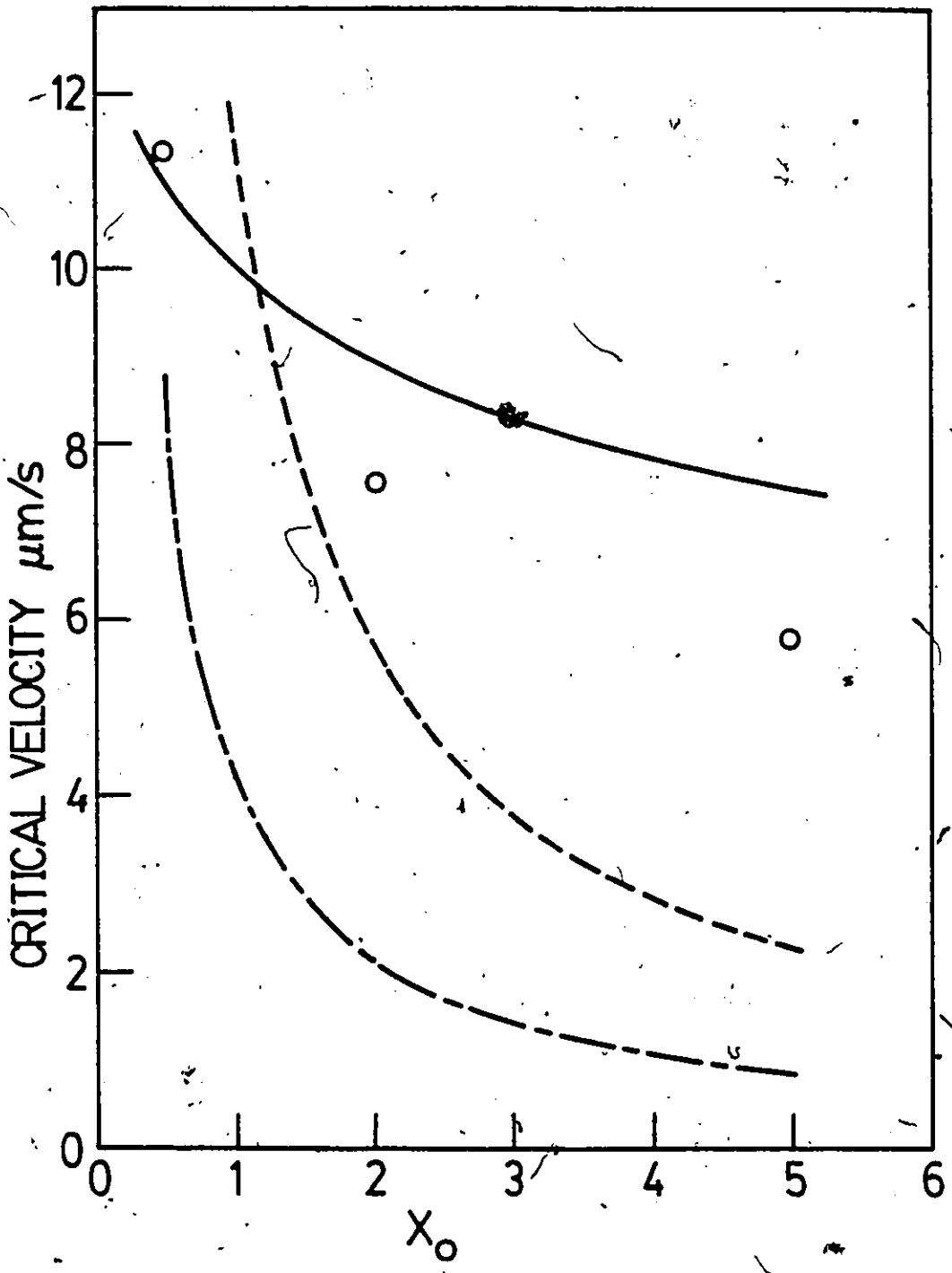


Fig.12c

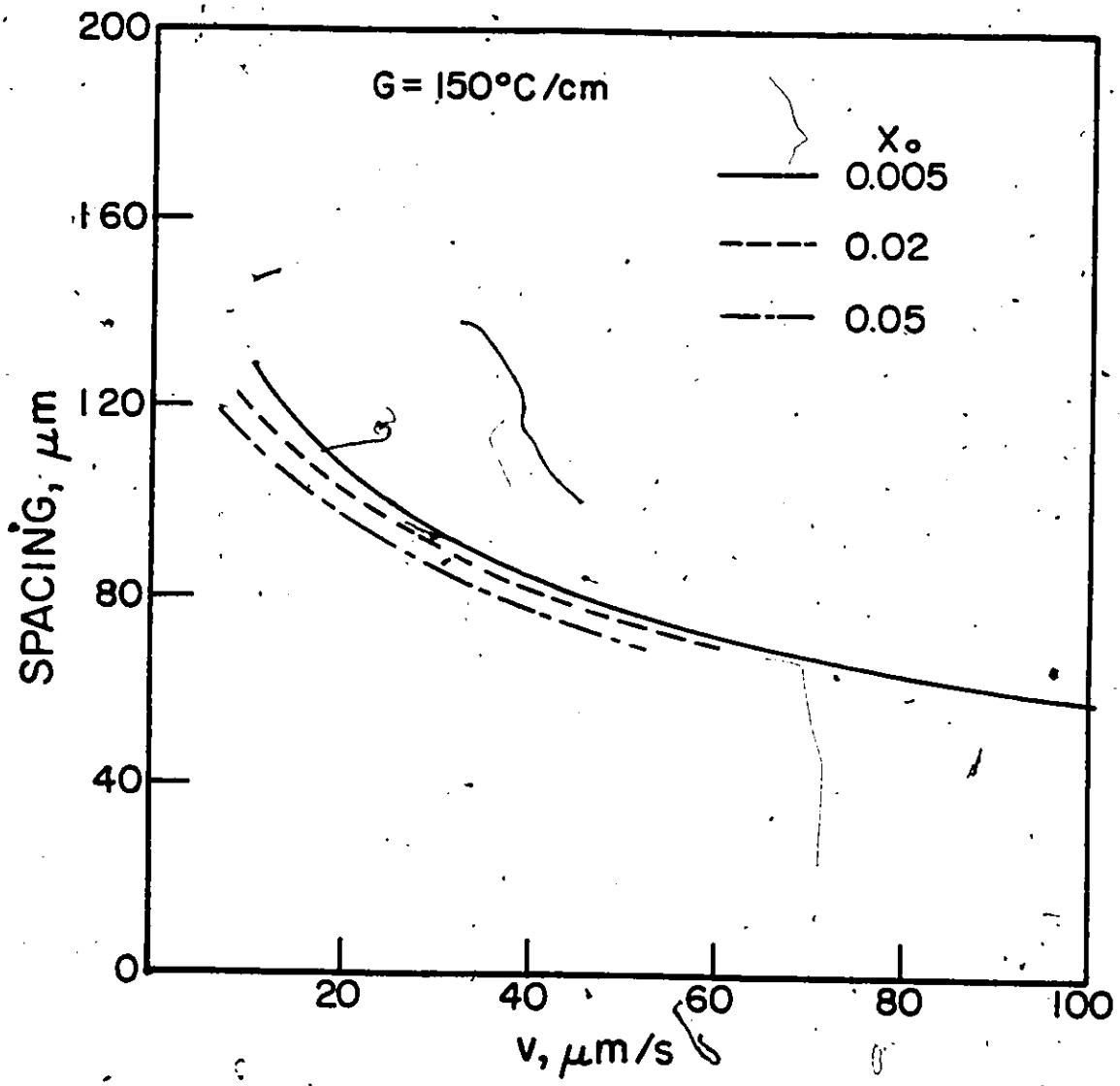


Fig. 13. Calculated cell spacing as a function of velocity for G = 150°C/cm.

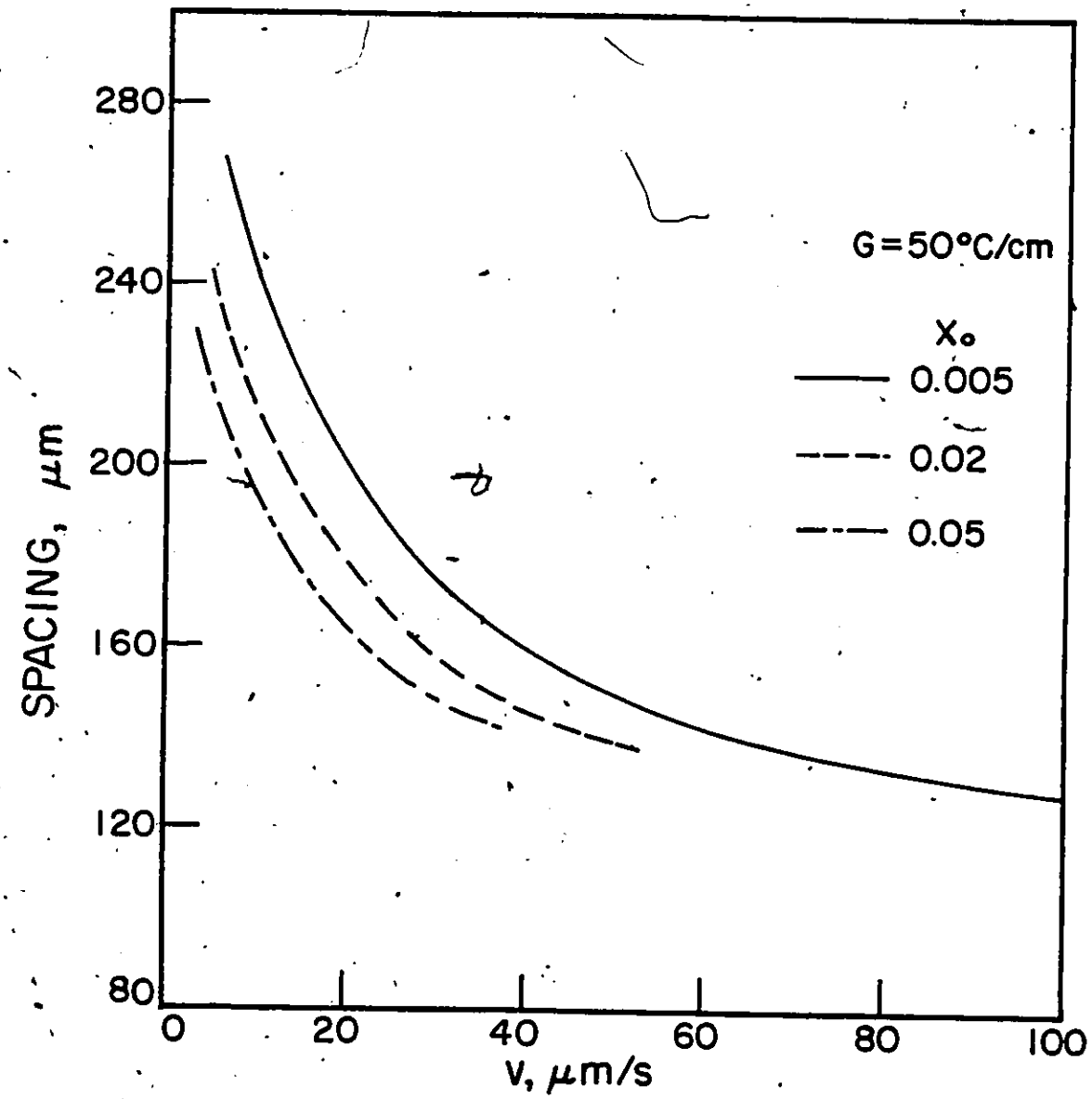


Fig. 14: Calculated cell spacing as a function of velocity of G = 50°C/cm.

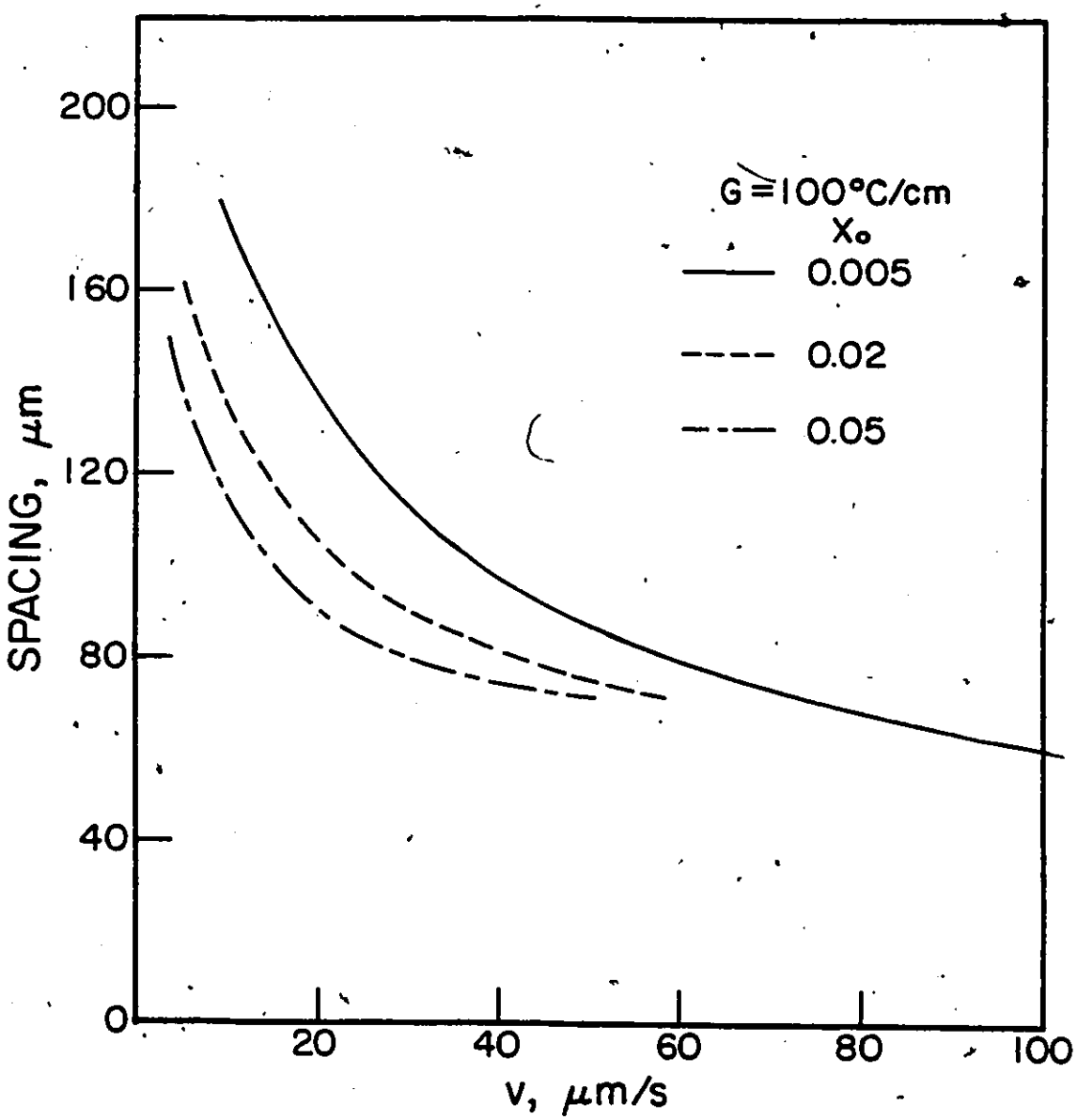


Fig. 15: Calculated cell spacing as a function of velocity for G = 100°C/cm.

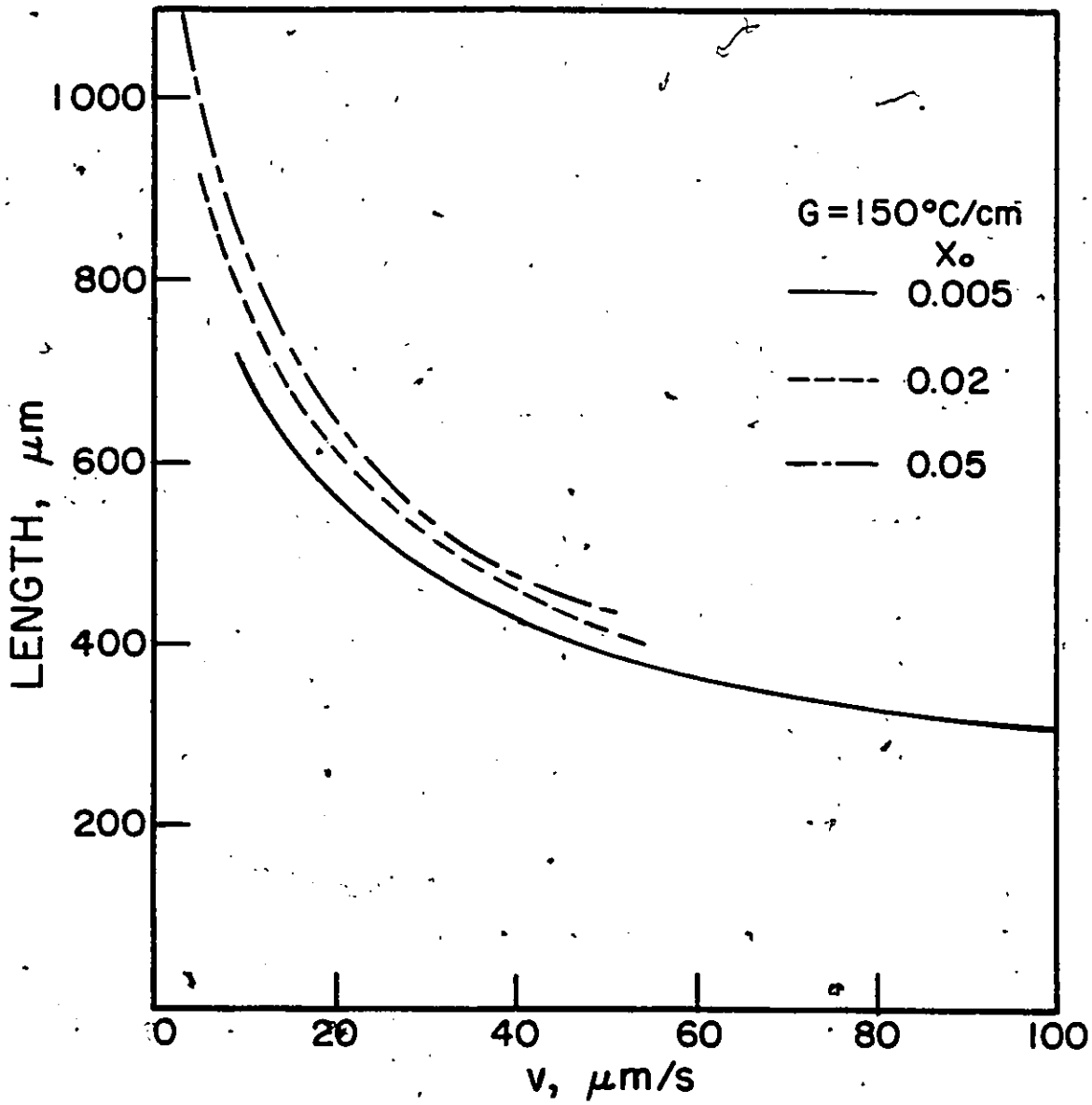


Fig. 16: Calculated cell length as a function of velocity for G = 150°C/cm.

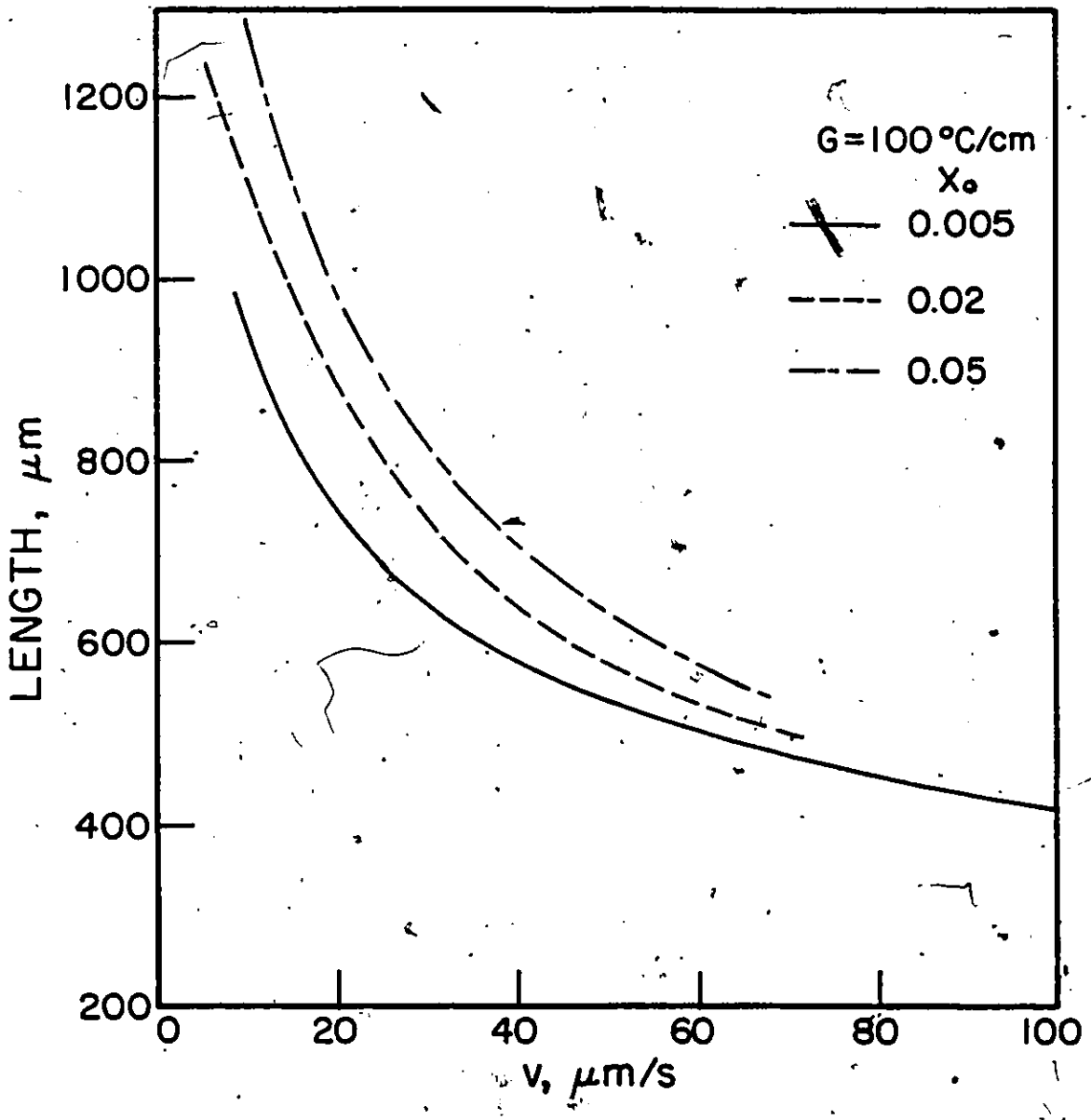


Fig. 17: Calculated cell length as a function of velocity for G = 100°C/cm.

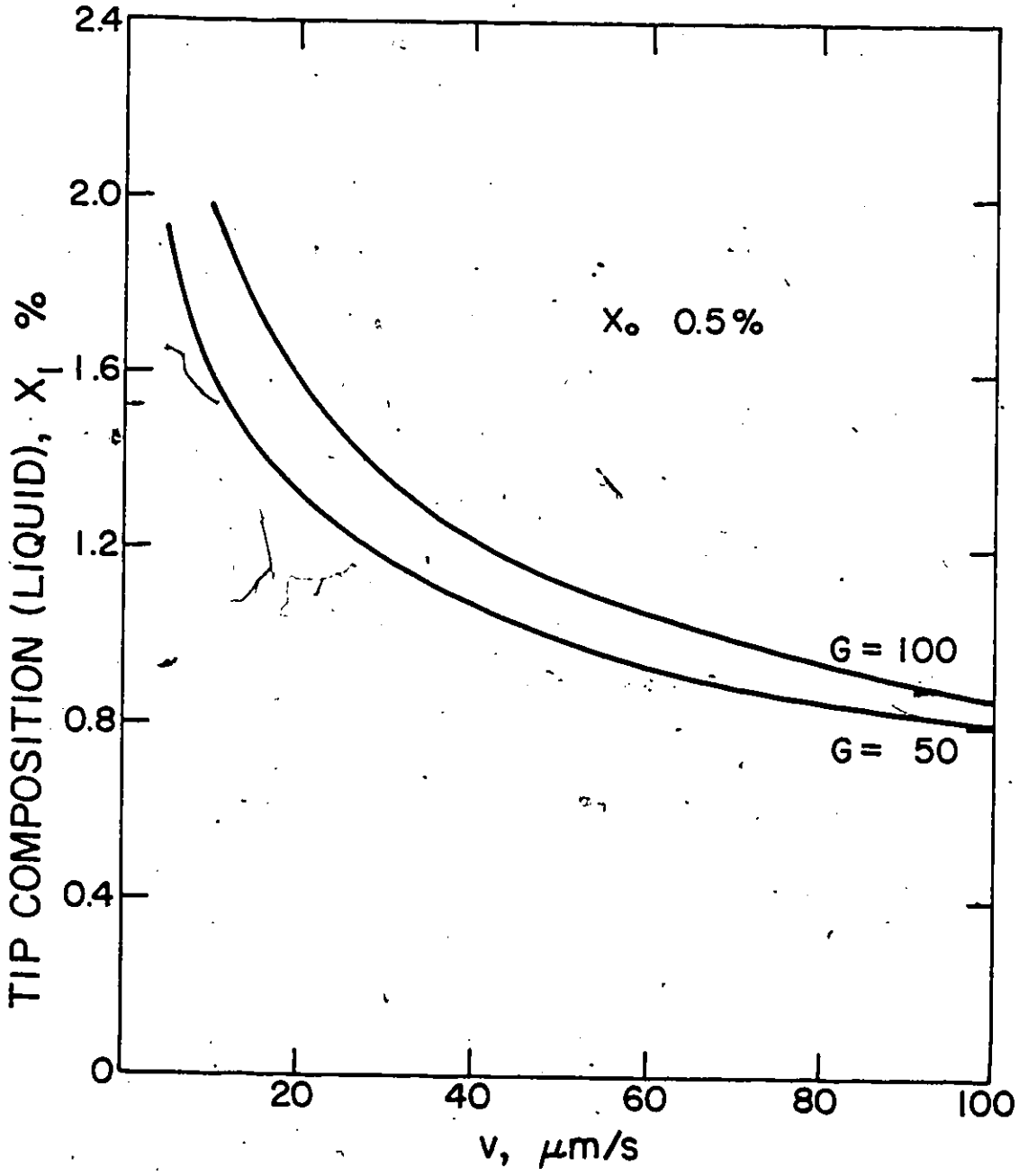


Fig. 18: Liquid composition at the cell tip versus velocity.

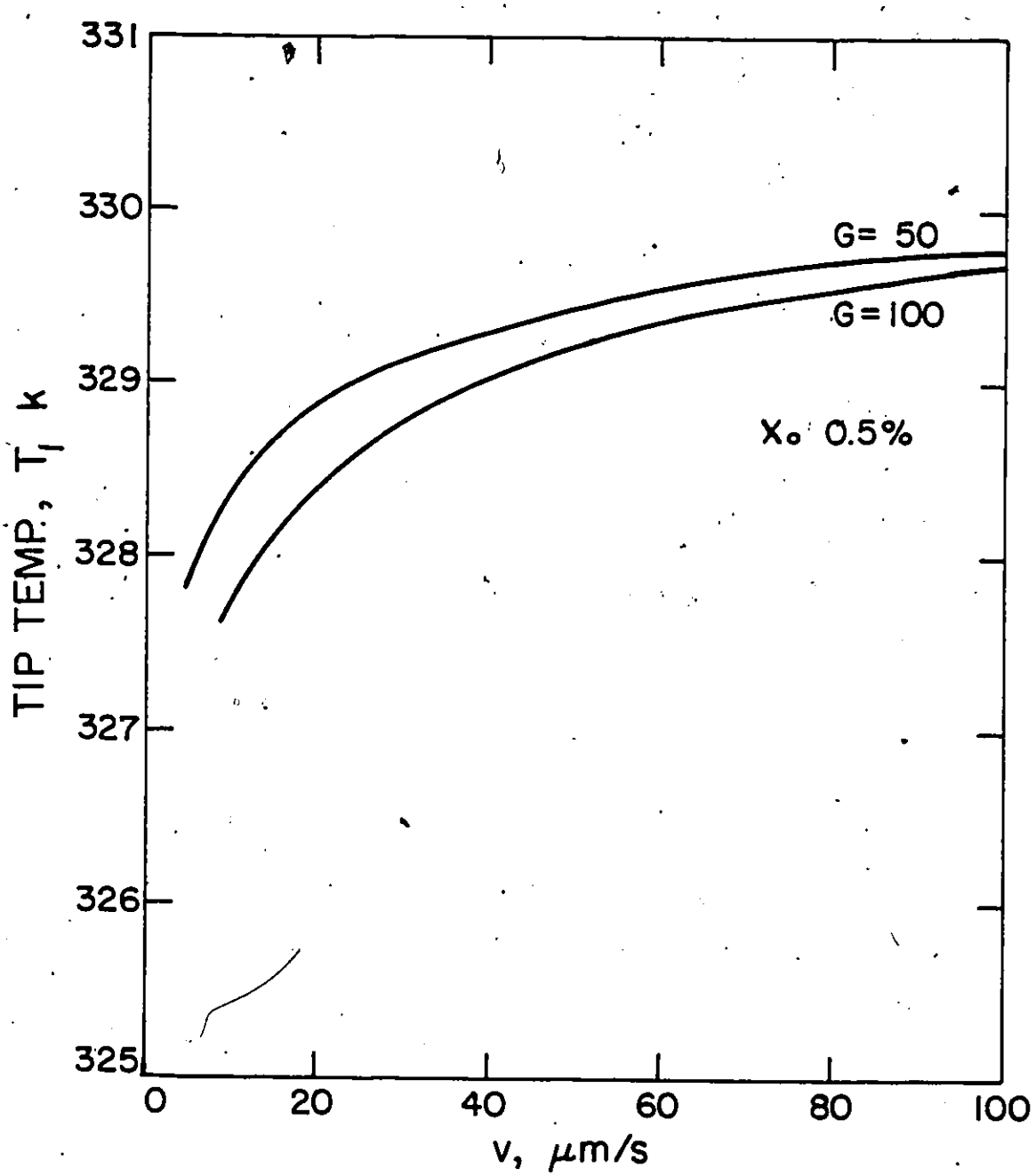


Fig. 19: Cell tip temperature versus velocity.

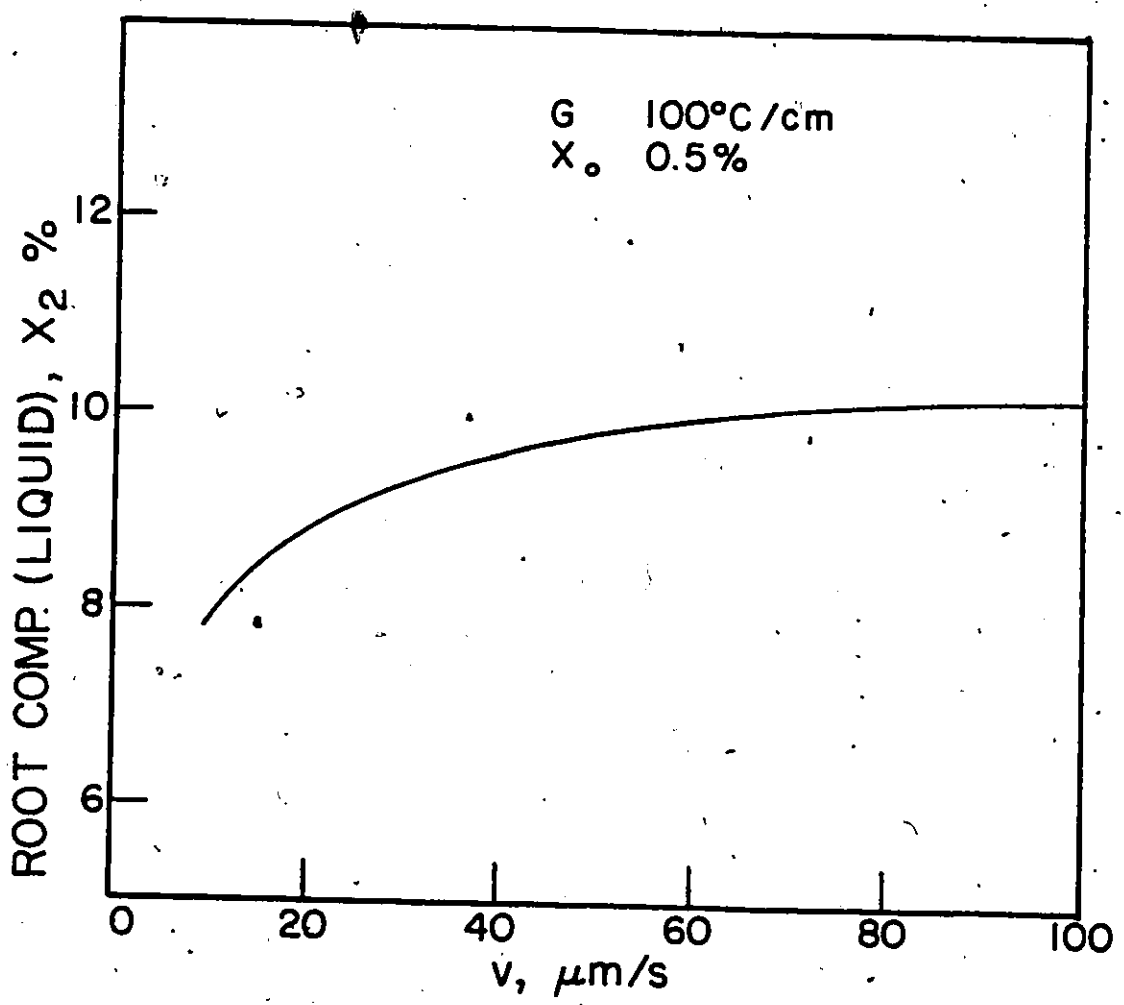


Fig. 20: Liquid composition at the root versus velocity.

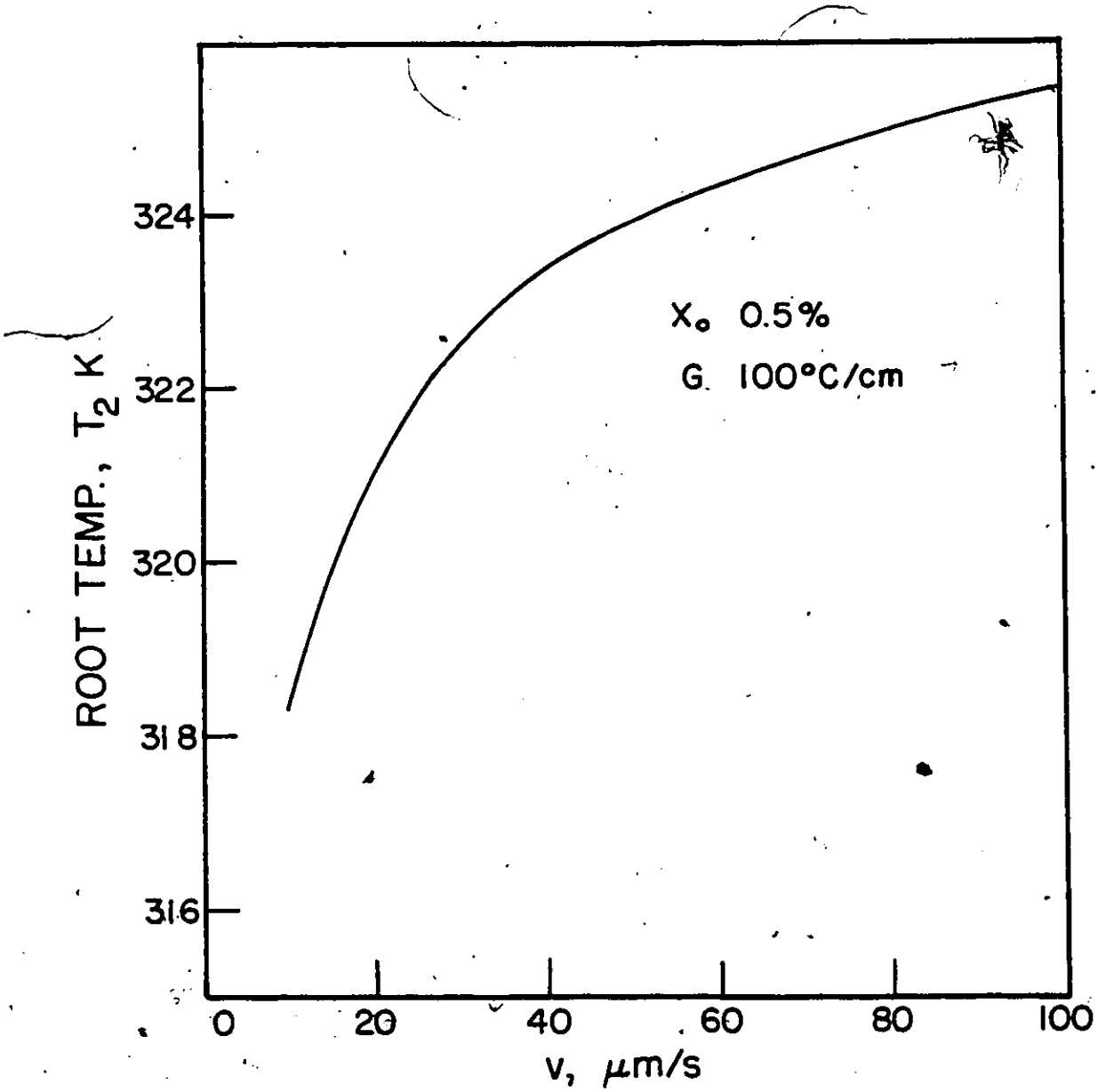


Fig. 21: Root temperature versus velocity.

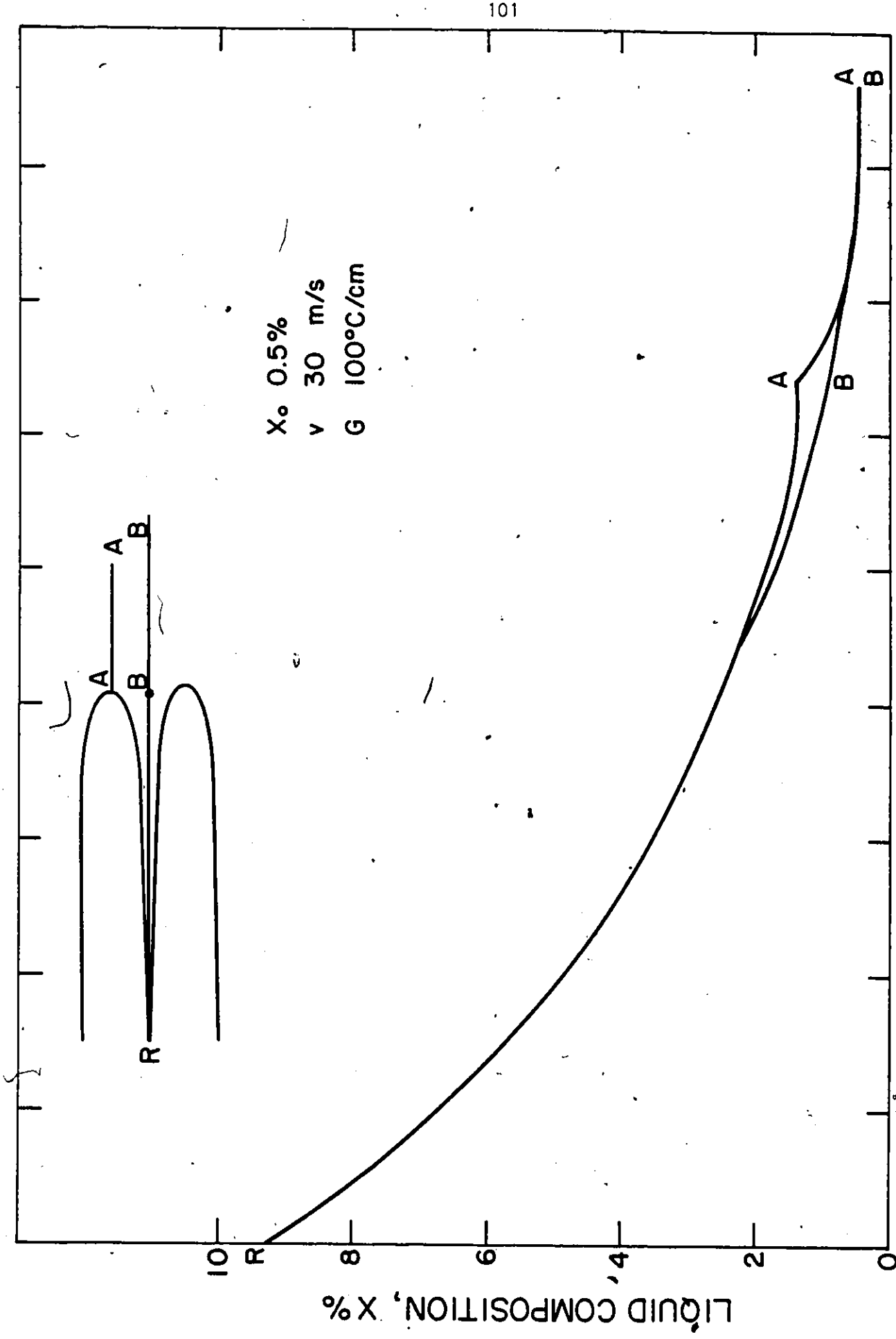


Fig. 22: Calculated spatial distribution of solute in the liquid.

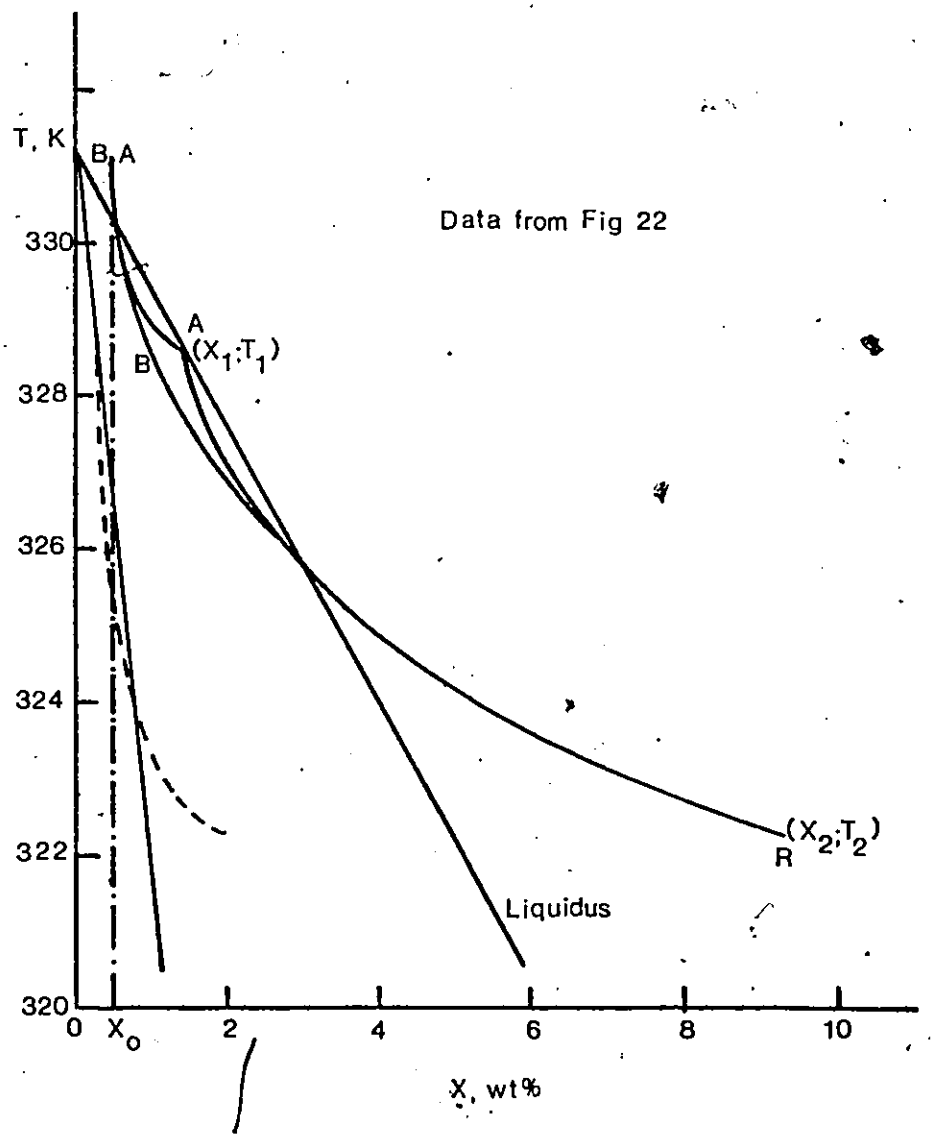


Fig. 23: Solute distribution superposed on phase diagram.

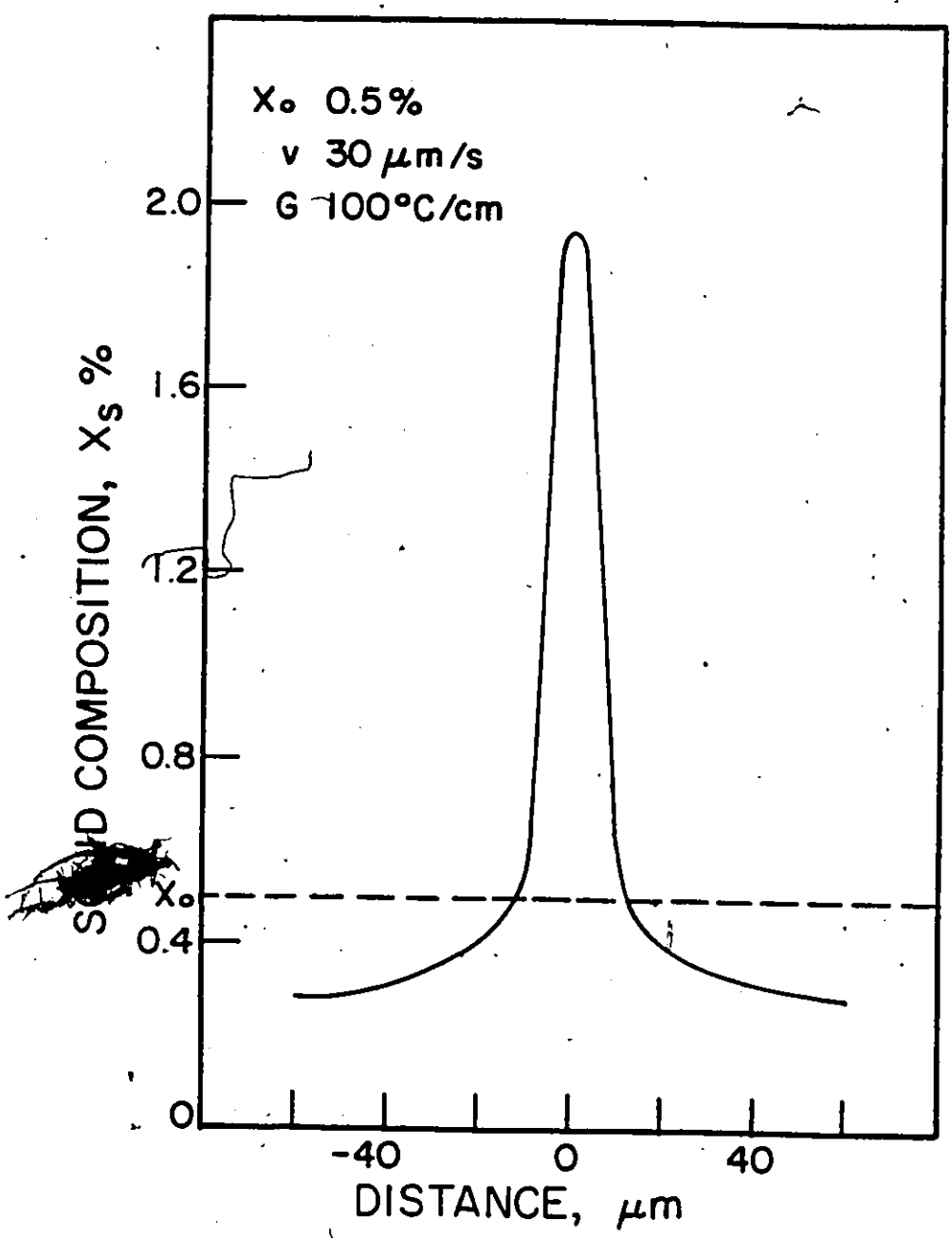


Fig. 24: Solute profile in the solid behind the interface.

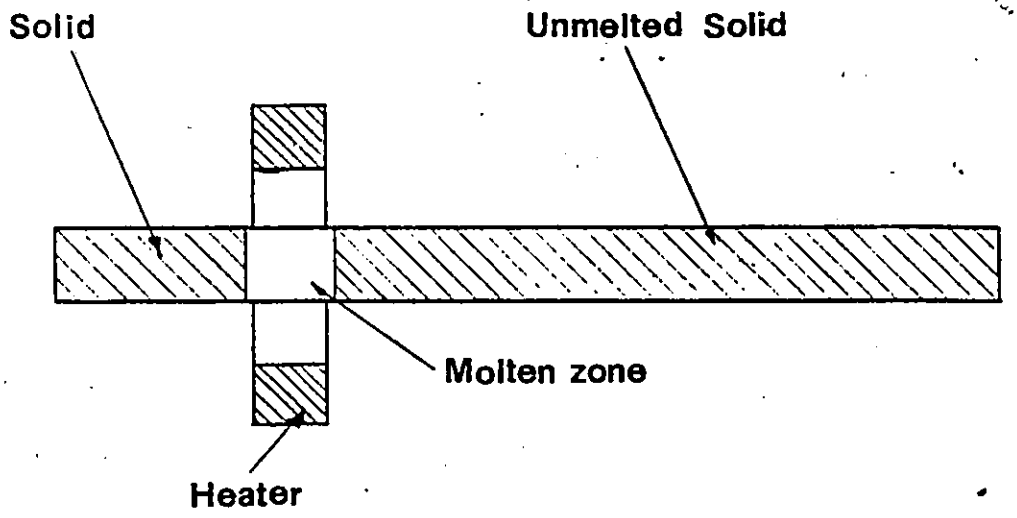


Fig. 25: Zone melting, schematic (from Ref. 49).

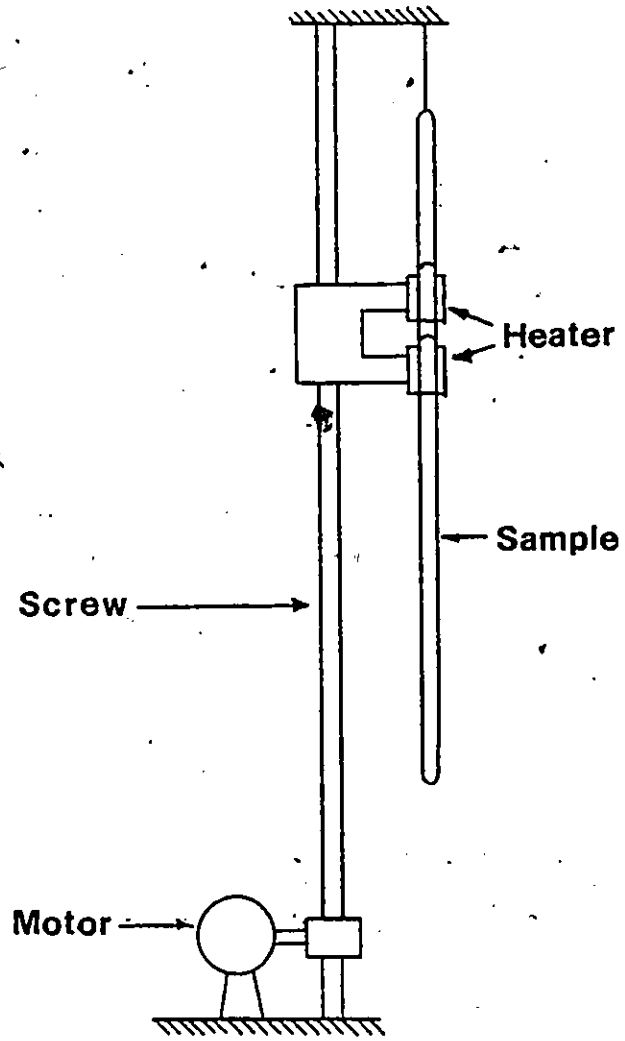


Fig. 26: Schematic of zone refiner used in this study.

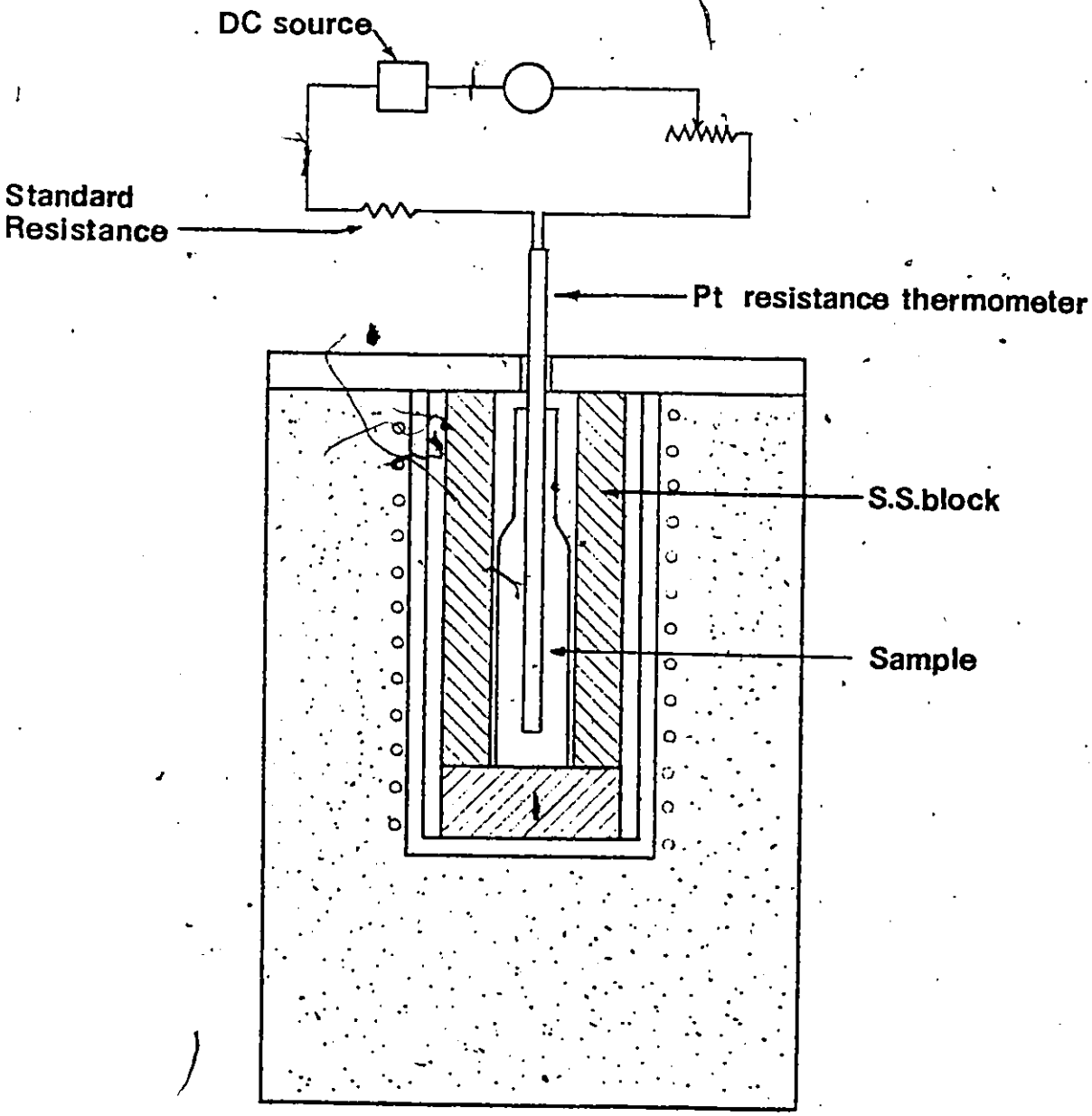


Fig. 27: Schematic of setup used for thermal analysis.

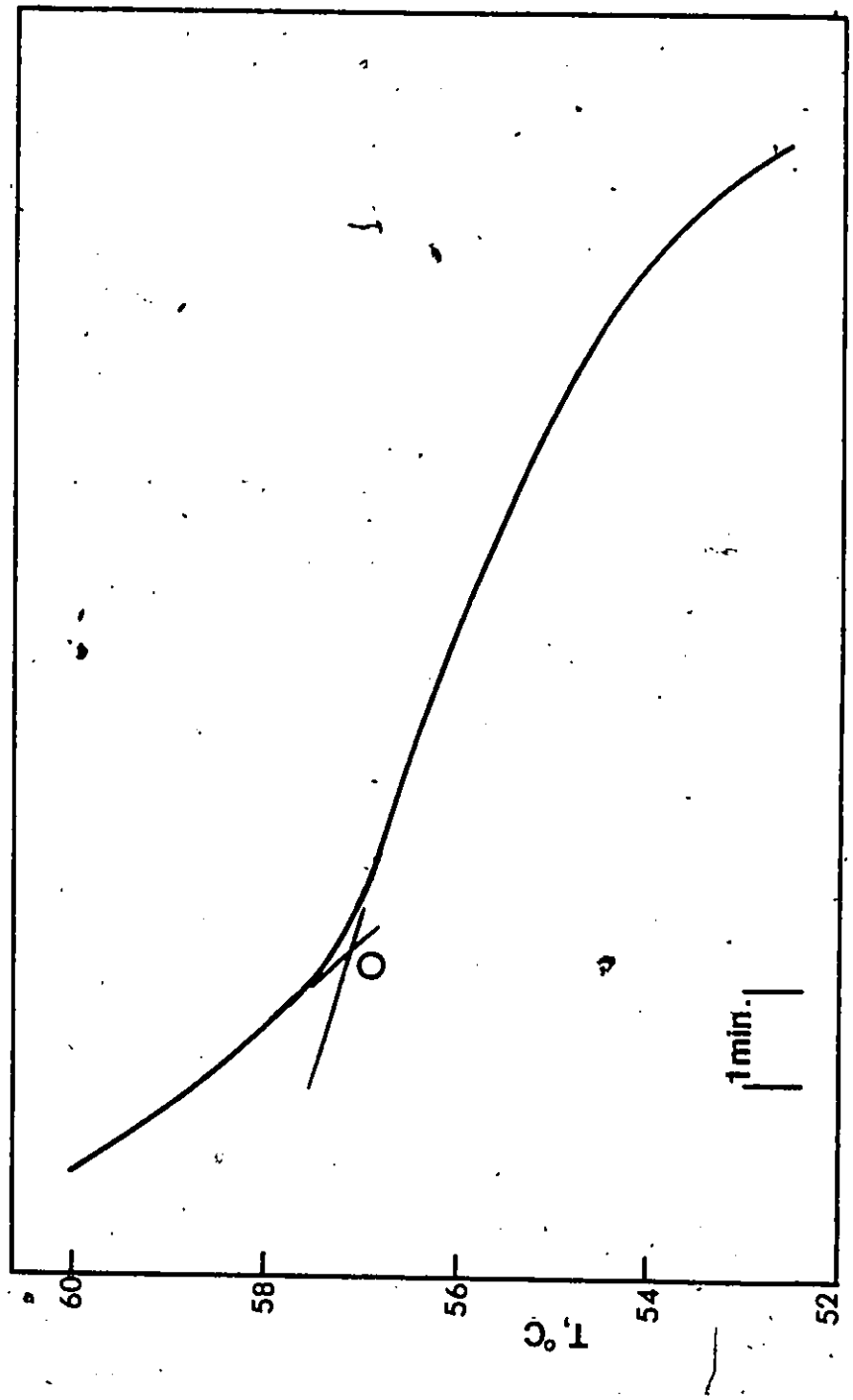


Fig. 28: Cooling curve for 0.5% alloy to show construction used to determine the arrest point.

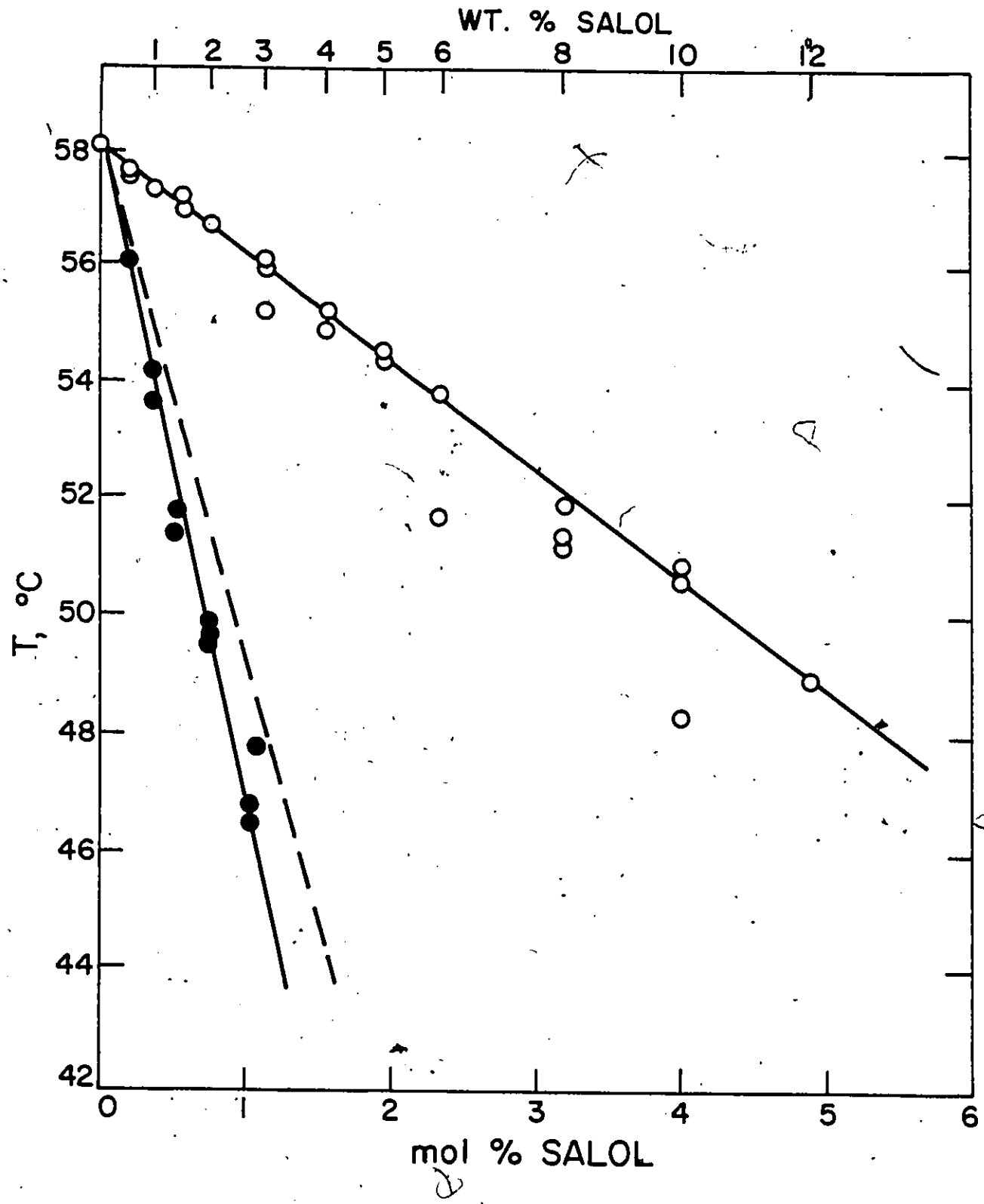


Fig. 29: Succinonitrile-rich side of the phase diagram in the SN-salol system. Solid lines are best-fit lines for experimental points. The broken line shows solidus as calculated in Section 4.4.

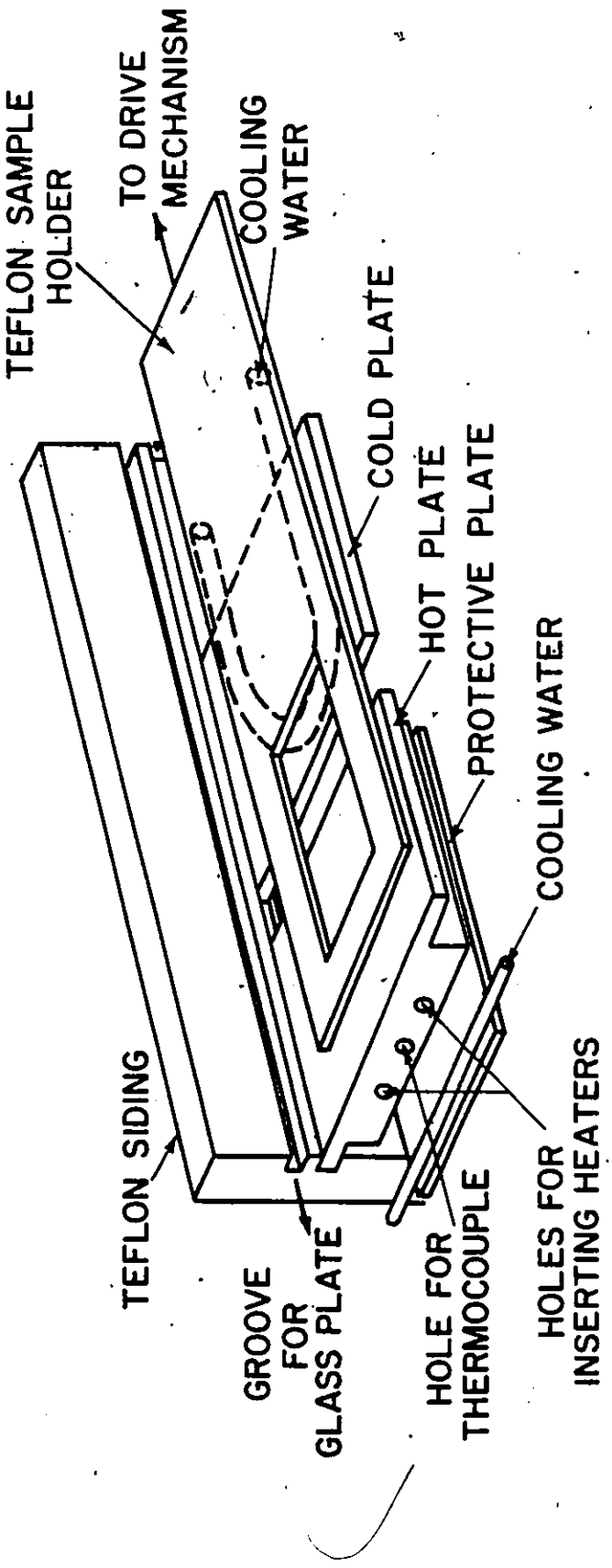


Fig. 30: A schematic diagram of the microscope stage.

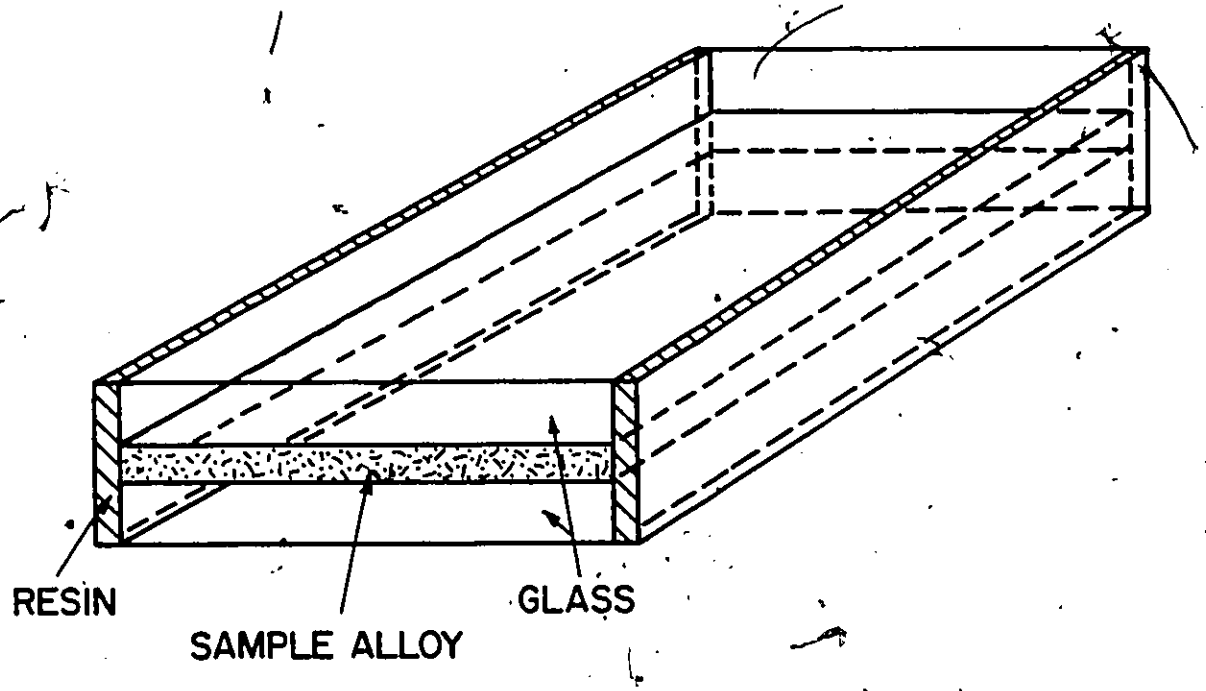


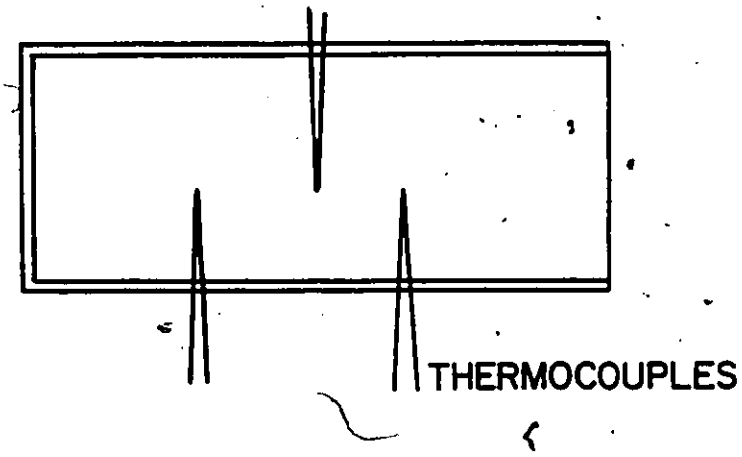


Fig. 31: A schematic diagram of the sample used in solidification experiments.

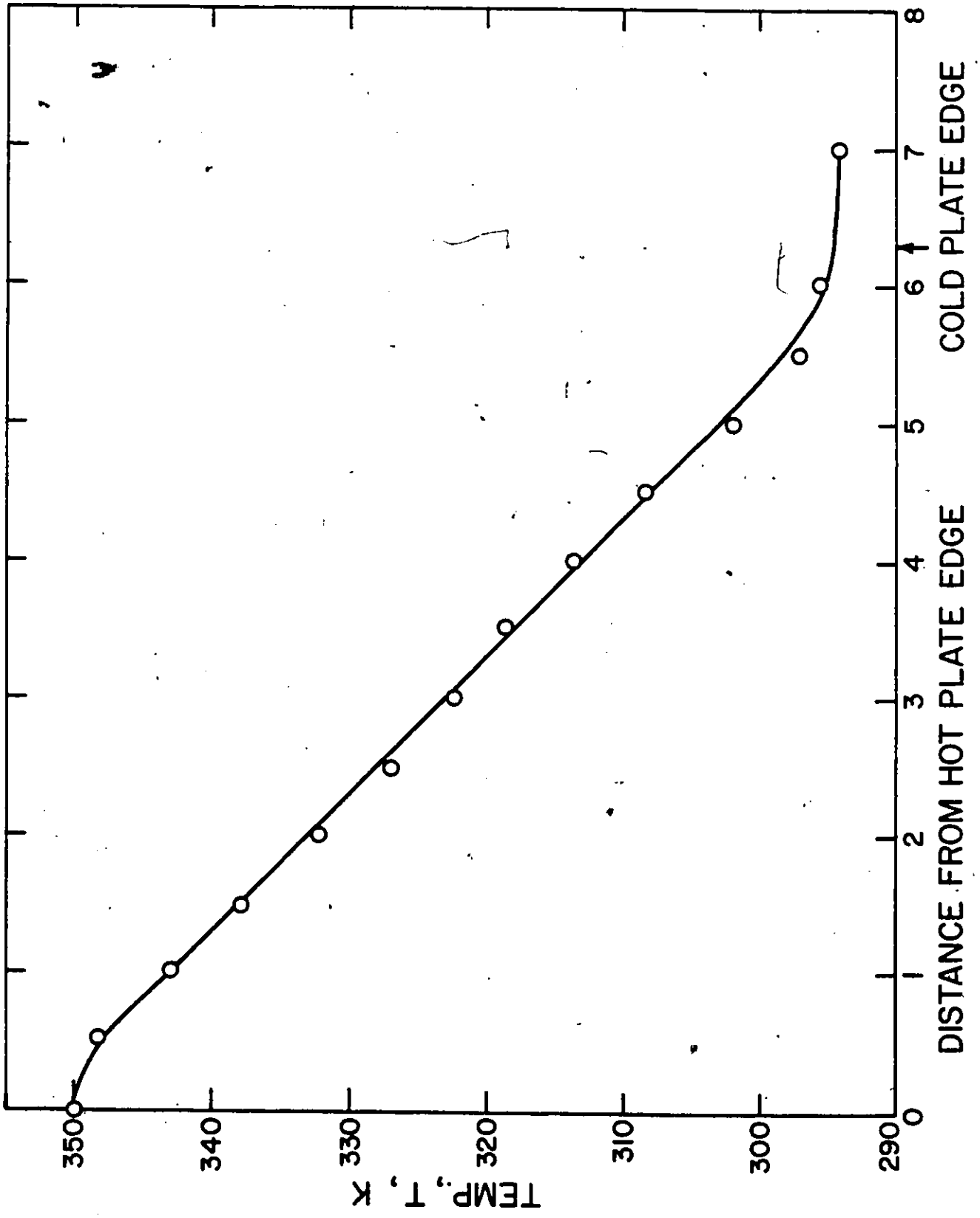


Fig. 32: Measured temperature profile in the gap of the stage.


Fig. 33: Photograph of an unstable interface growing at a velocity below the critical velocity for the onset of stable cells and above the CS limit.

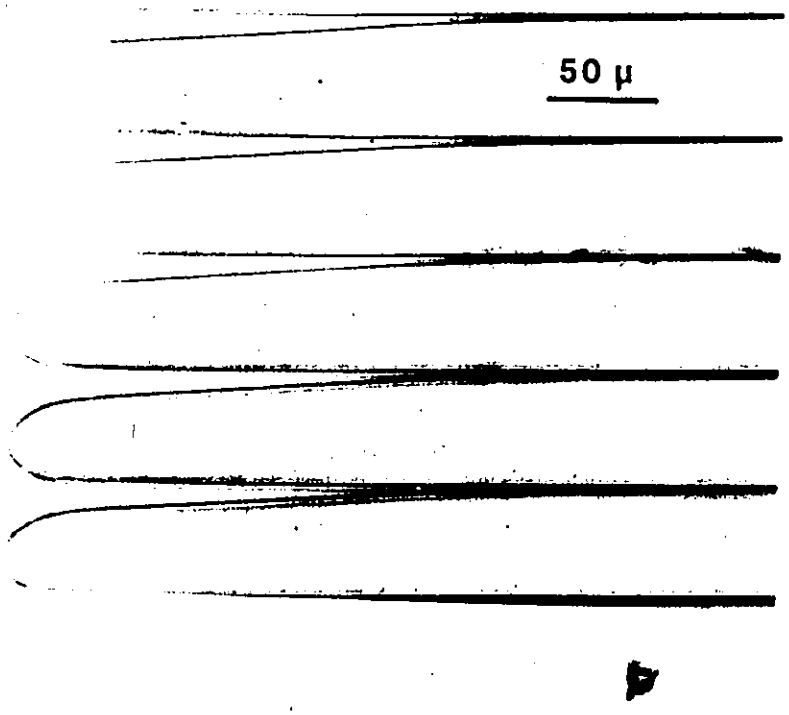


Fig. 34: A stable cellular interface.

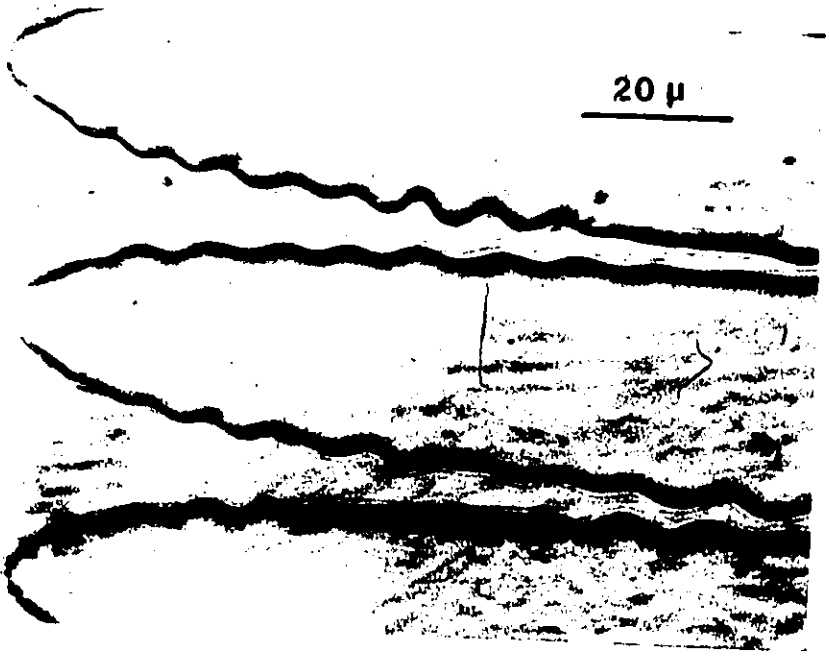


Fig. 35: Dendritic break down at high velocities.

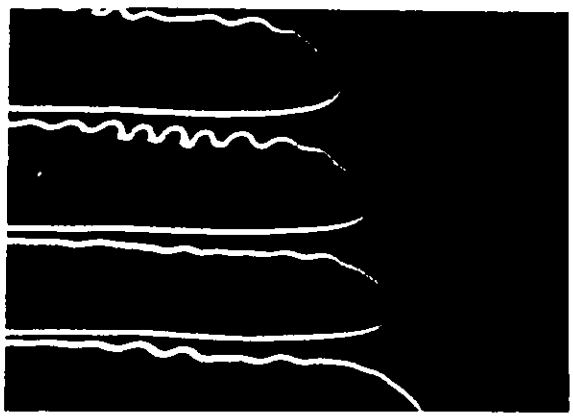

Fig. 36: Growth of a misoriented crystal.

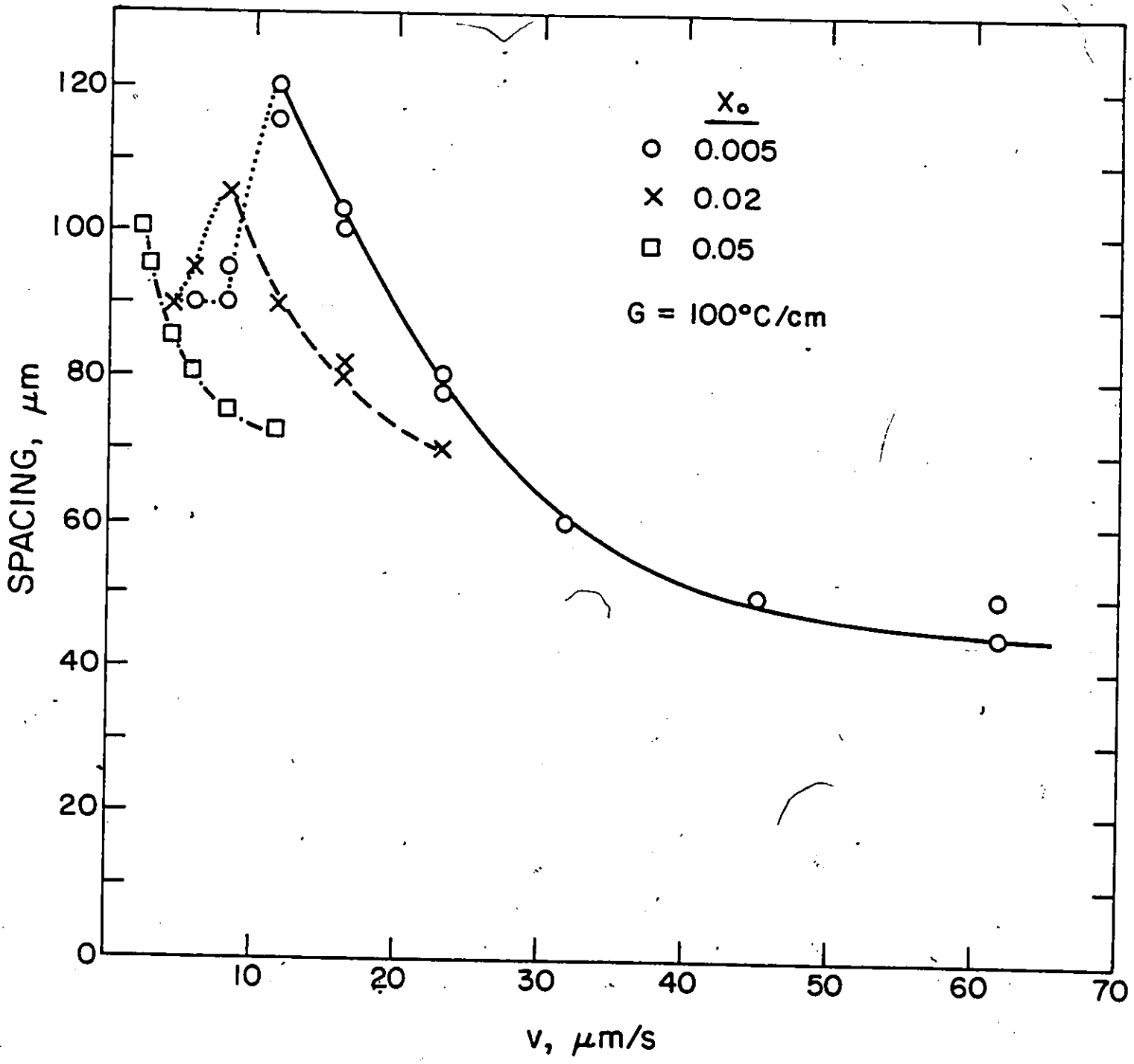


Fig. 37: Observed spacing versus velocity relationship for G = 100°C/cm.

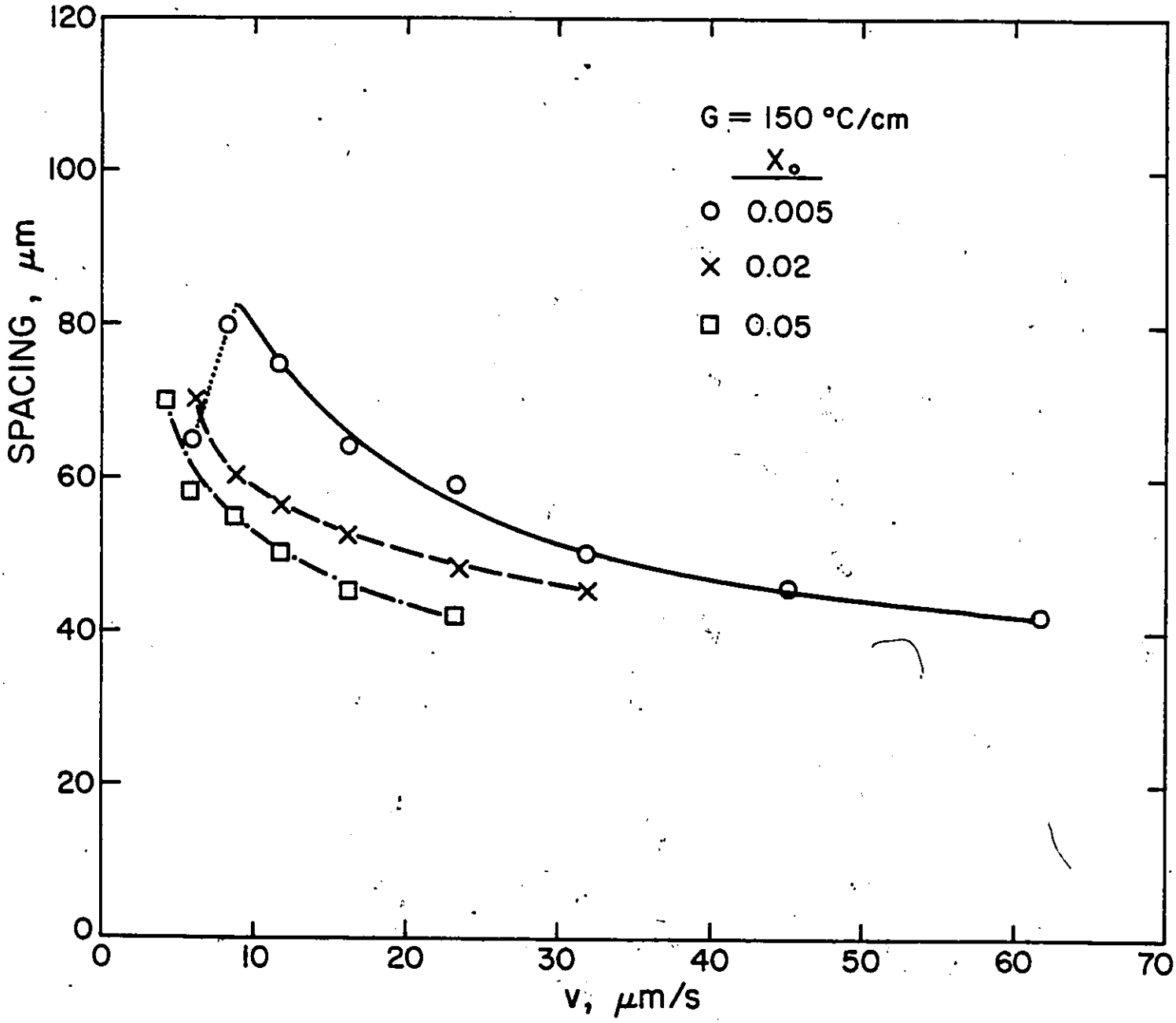


Fig. 38: Observed spacing versus velocity relationship for G = 150°C/cm.

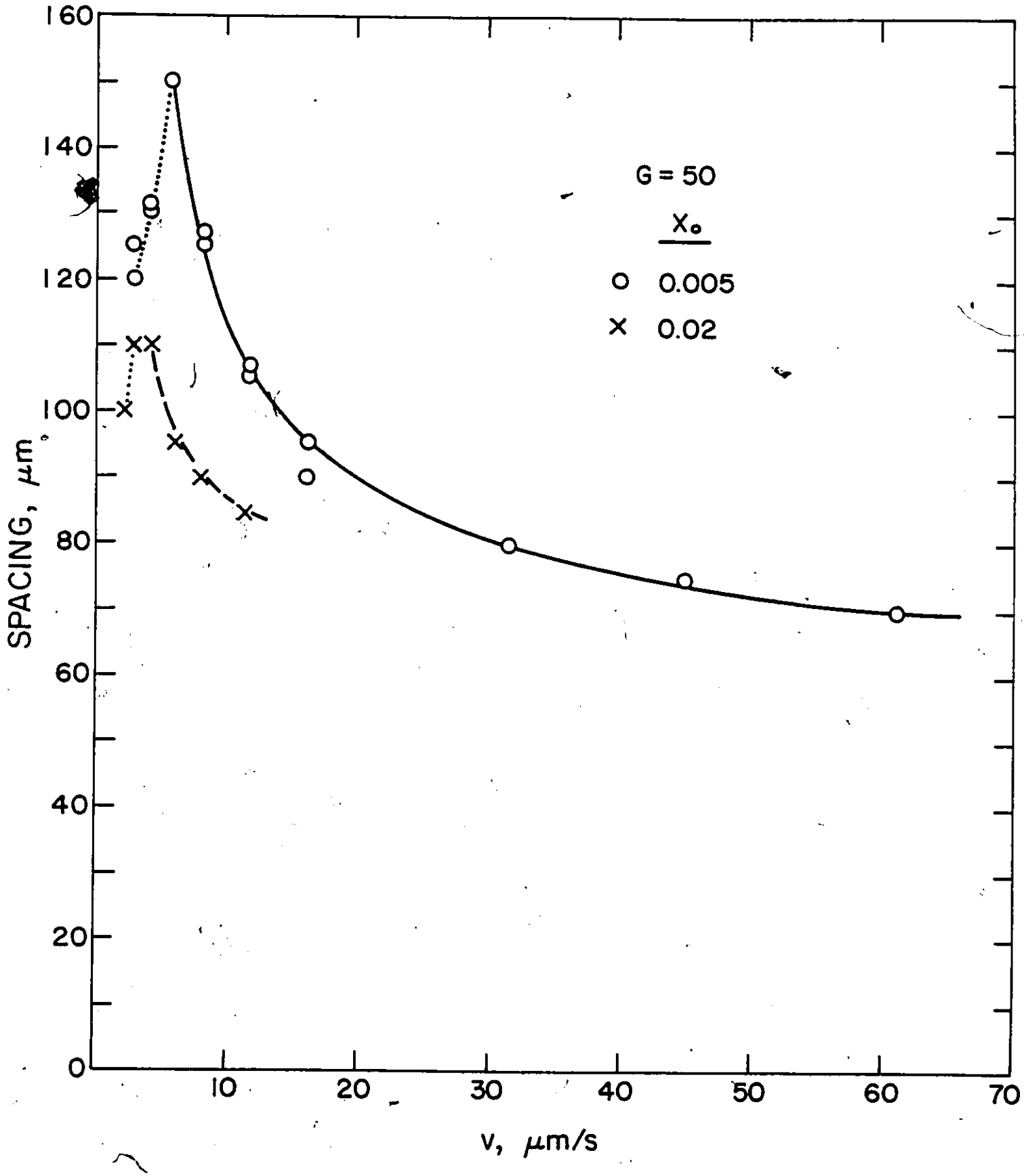


Fig. 39: Observed spacing versus velocity relationship for G = 50°C/cm.

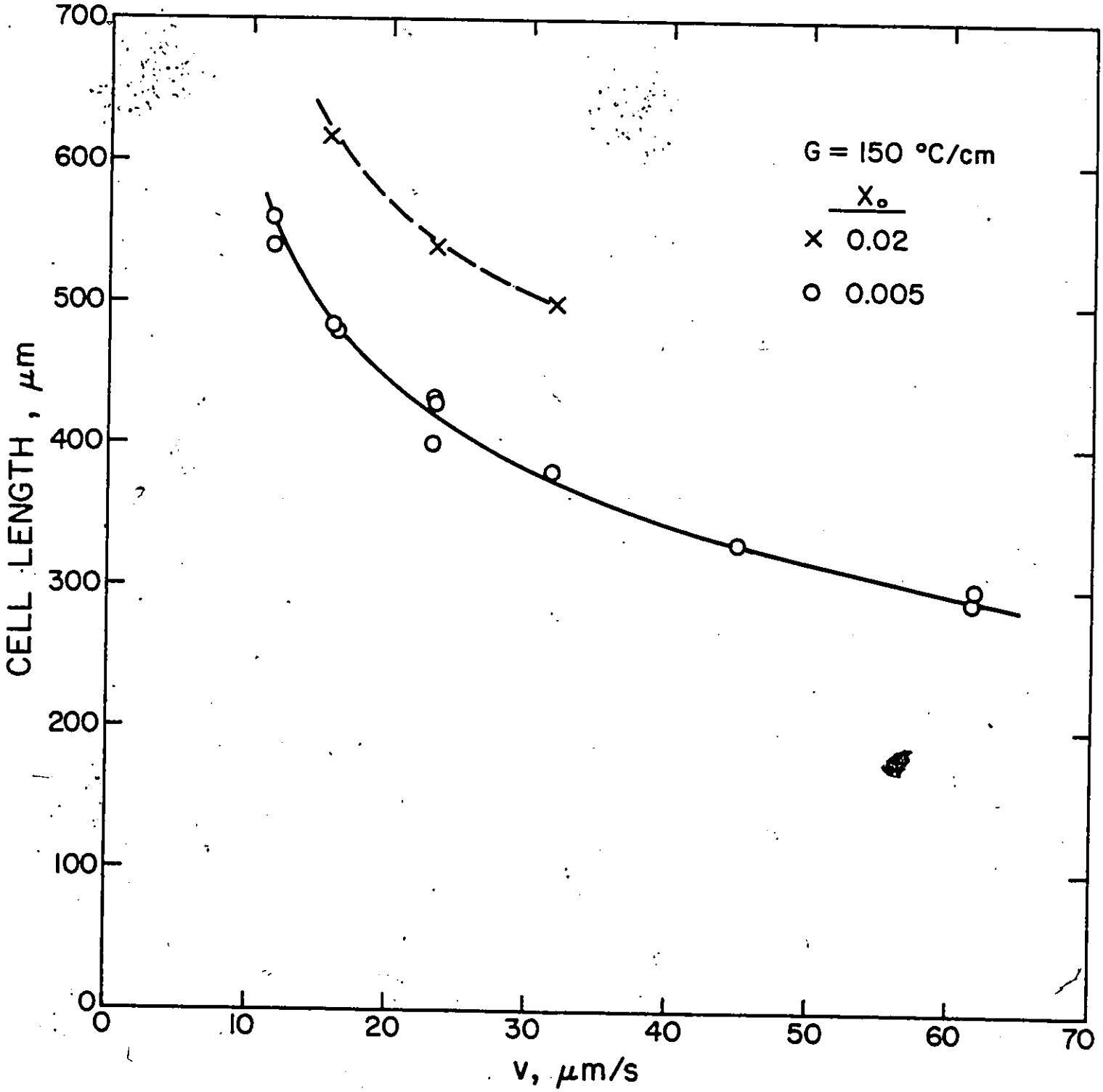


Fig. 40: Observed cell length versus velocity.

Fig. 41: Photograph showing the pinching-off mechanism during the transient between two steady-states.

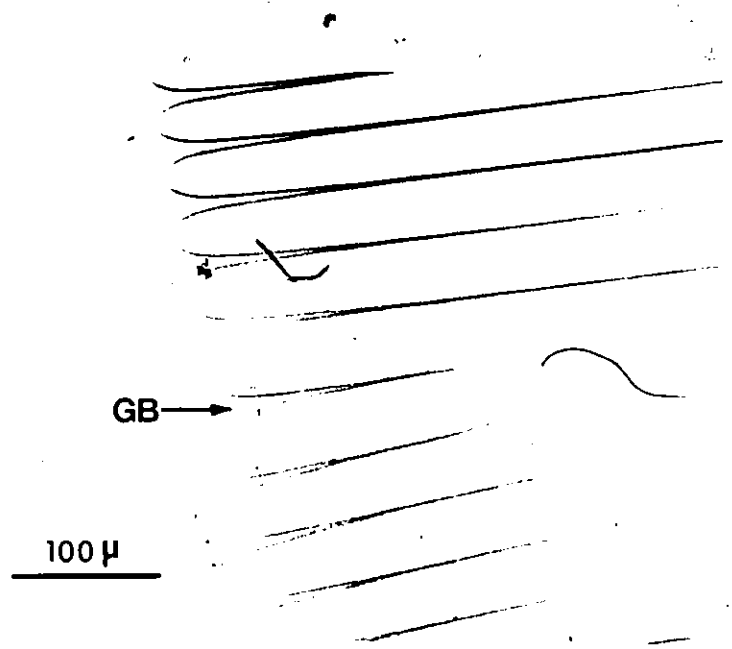


Fig. 42. Photograph showing an unstable cell wall at a grain boundary.

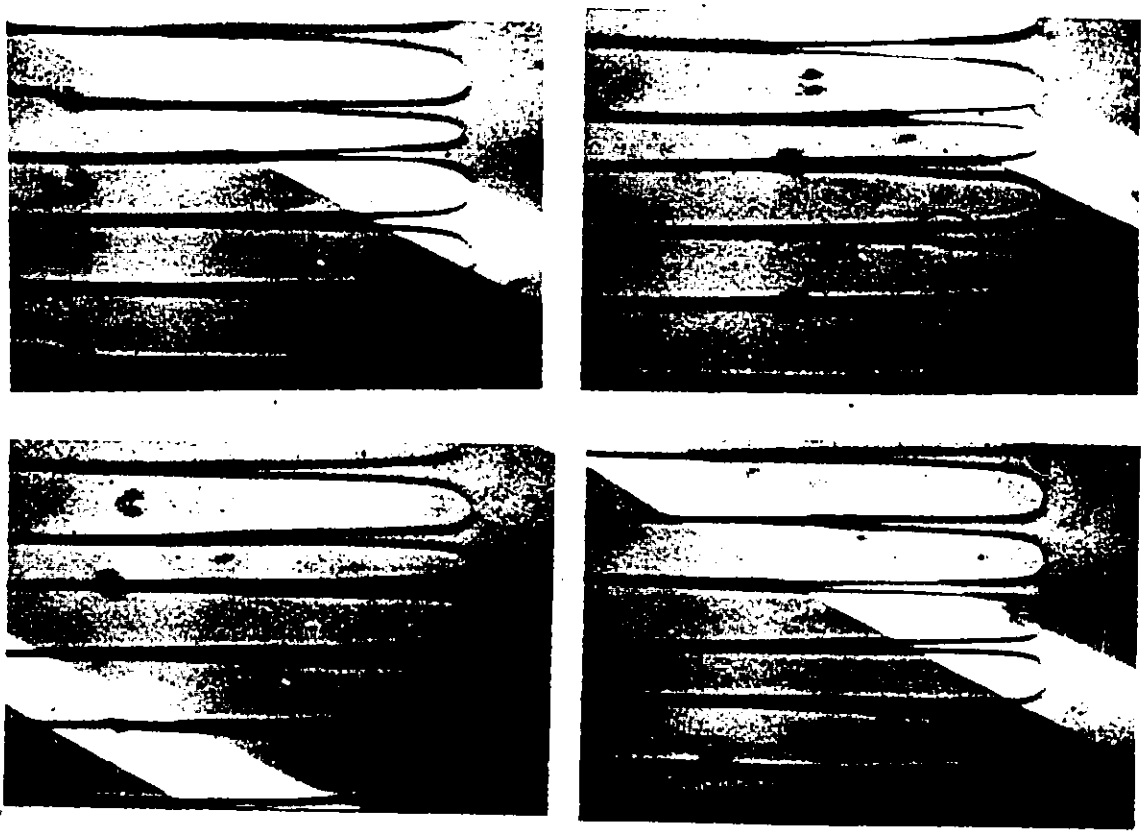

Fig. 43: A sequence showing the mechanism for the removal of a local non-uniformity in cell spacing. Low amplitude waves (circled) migrate along the cell walls to effect spacing changes.

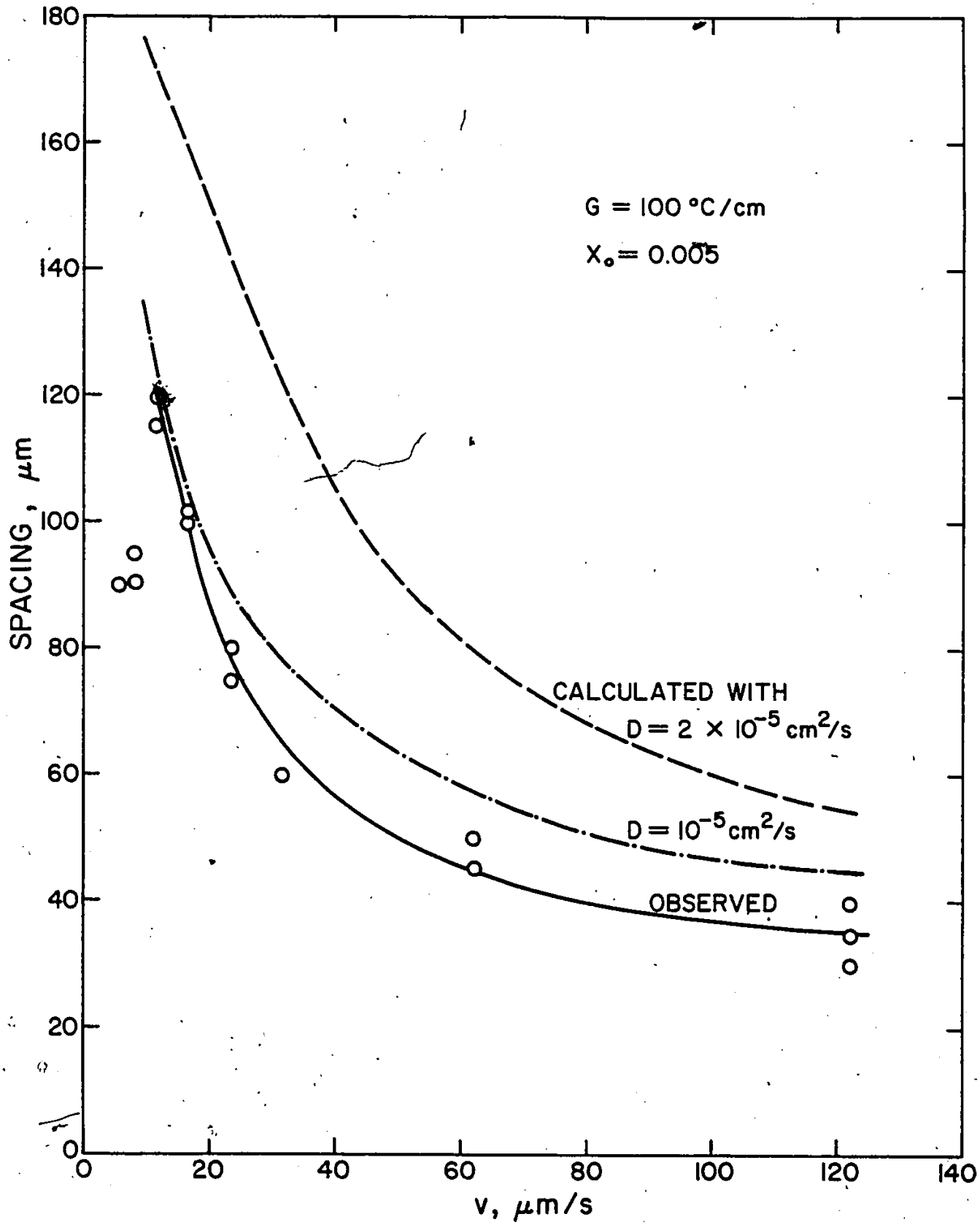


Fig. 44: Spacing versus velocity. G = 100°C/cm. $X_0$ = 0.005.

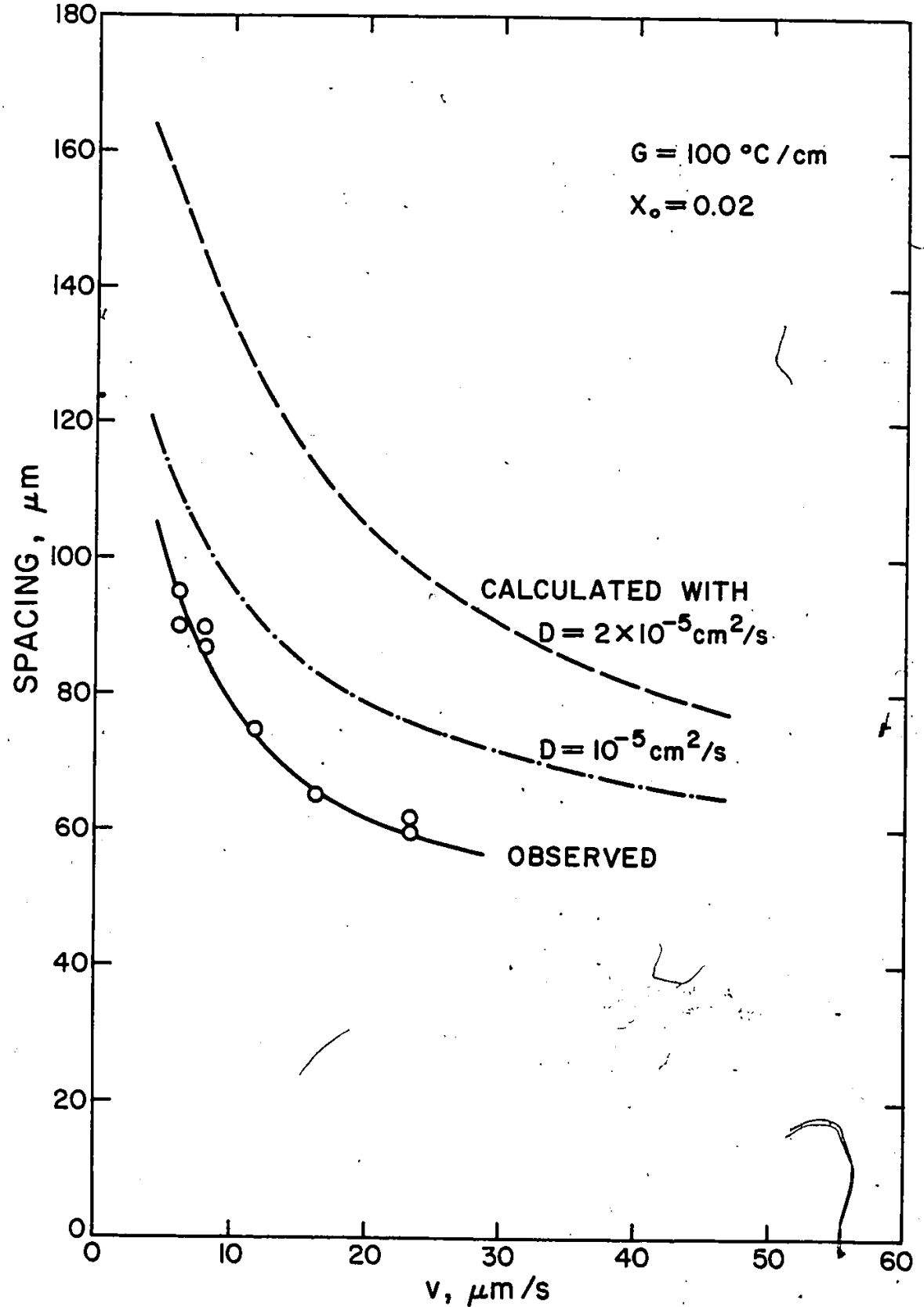


Fig. 45: Spacing versus velocity. G = 100°C/cm. $X_o$ = 0.005.

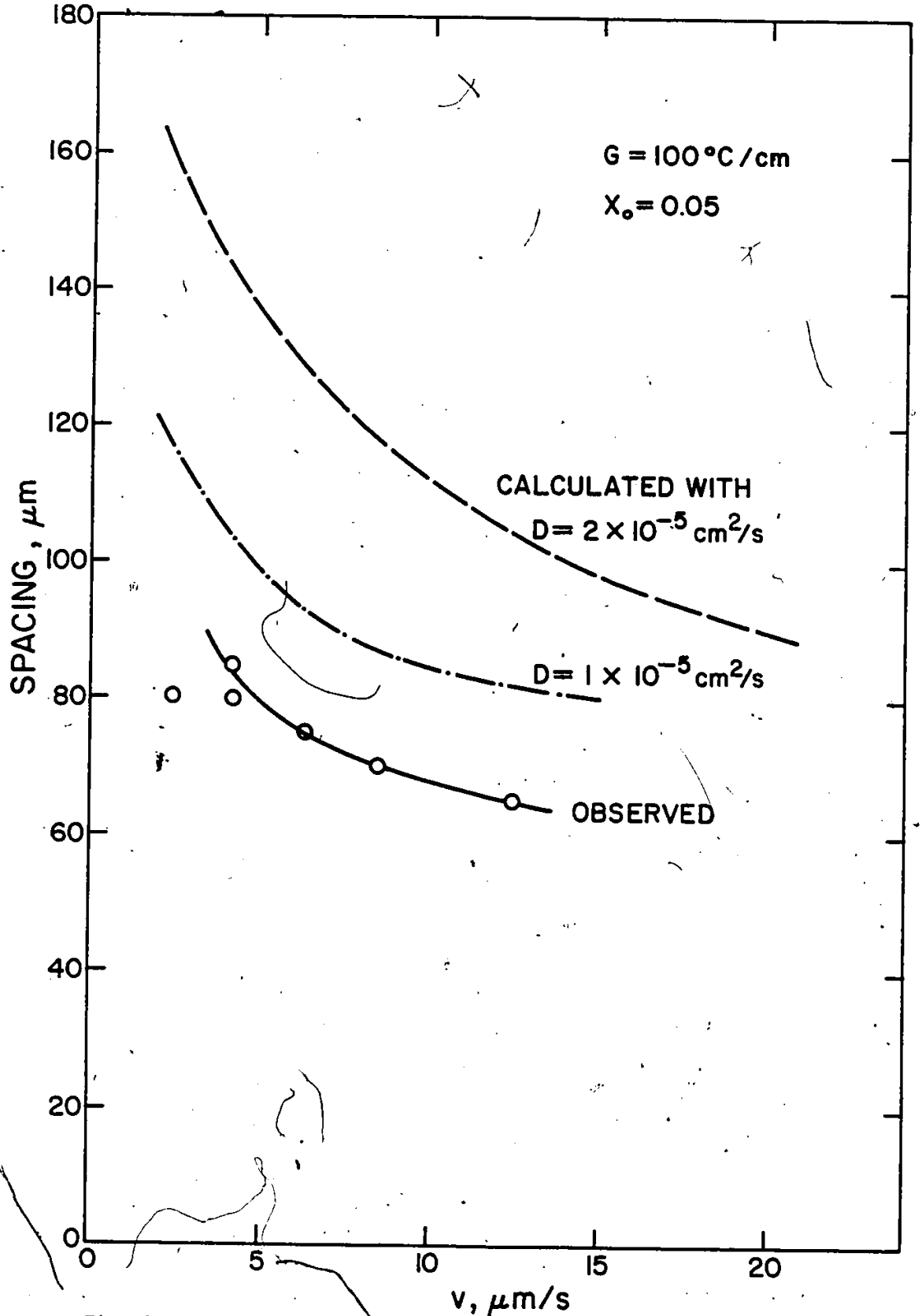


Fig. 46: Spacing versus velocity. G = 100°C/cm. $X_o$ = 0.05.

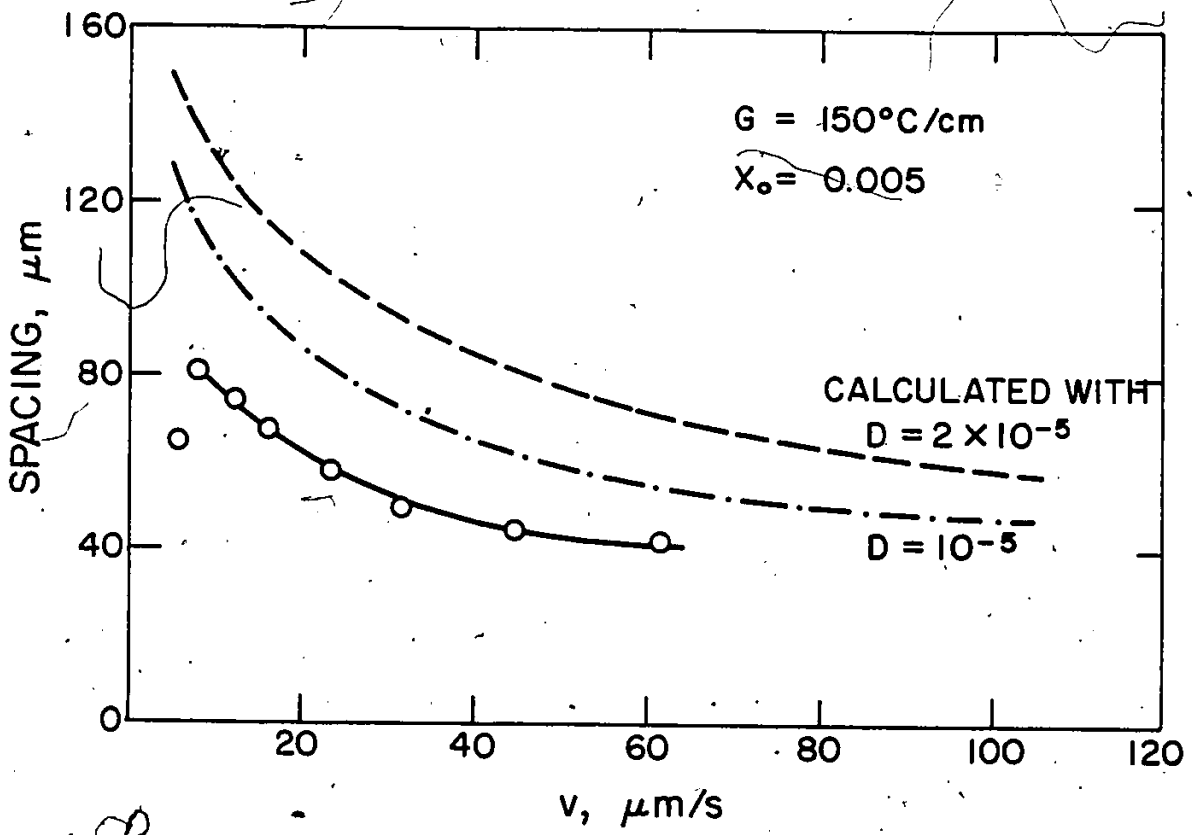


Fig. 47: Spacing versus velocity.—G = 150°C/cm. $X_o$ = 0.005.

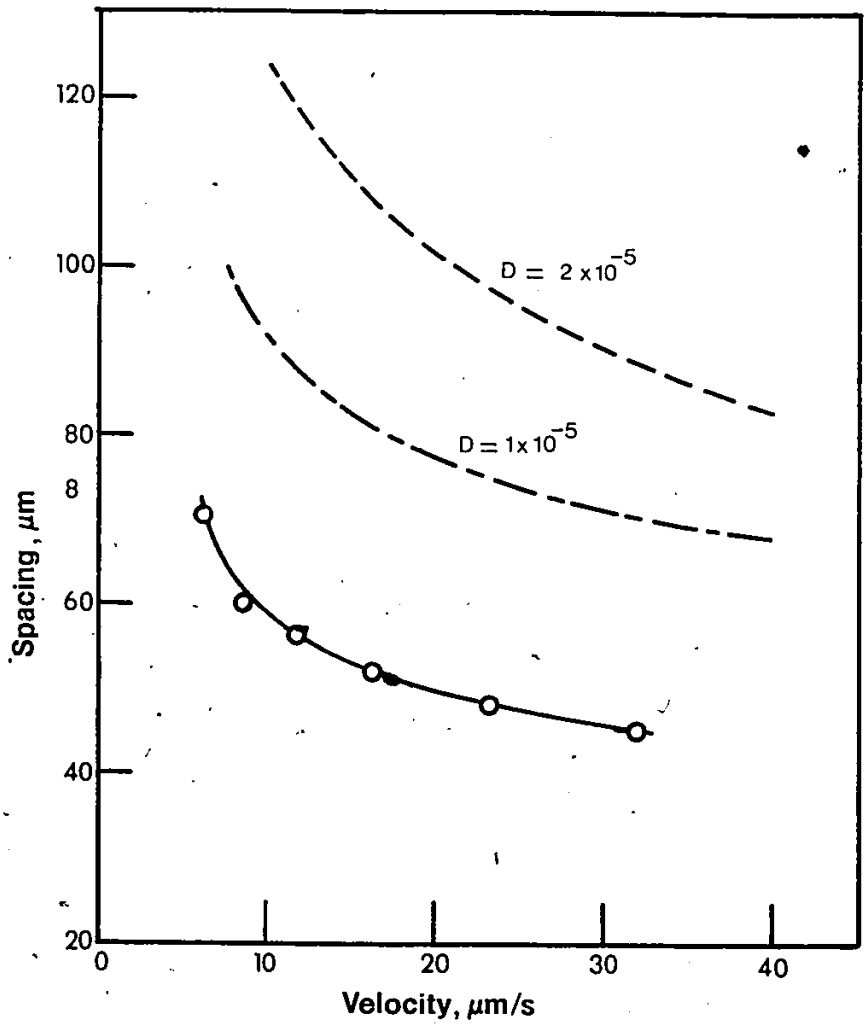


Fig. 48: Spacing versus velocity. G = 150°C/cm. $X_o$ = 0.02.

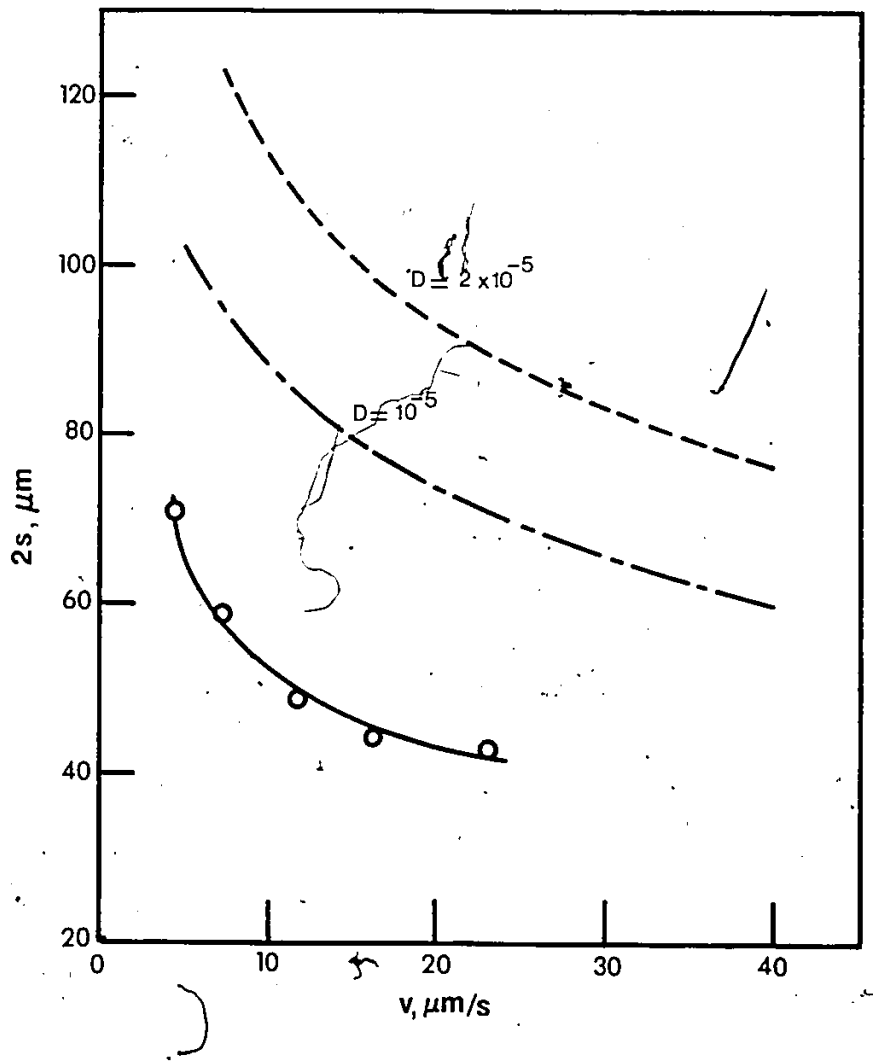


Fig. 49: Spacing versus velocity. G = 150°C/cm. $X_o$ = 0.05.

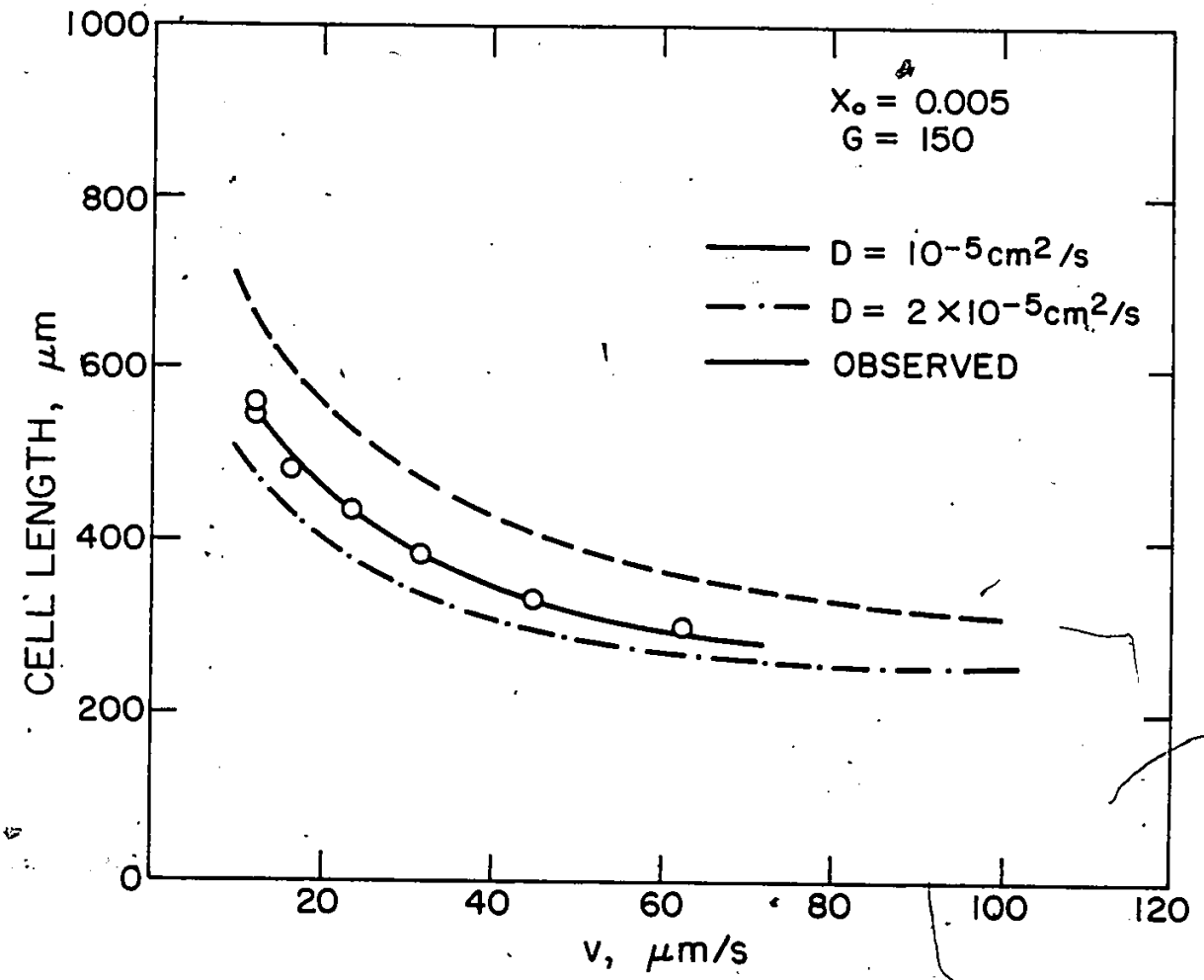


Fig. 50: Length versus velocity. G = 150°C/cm. $X_o$ = 0.005.

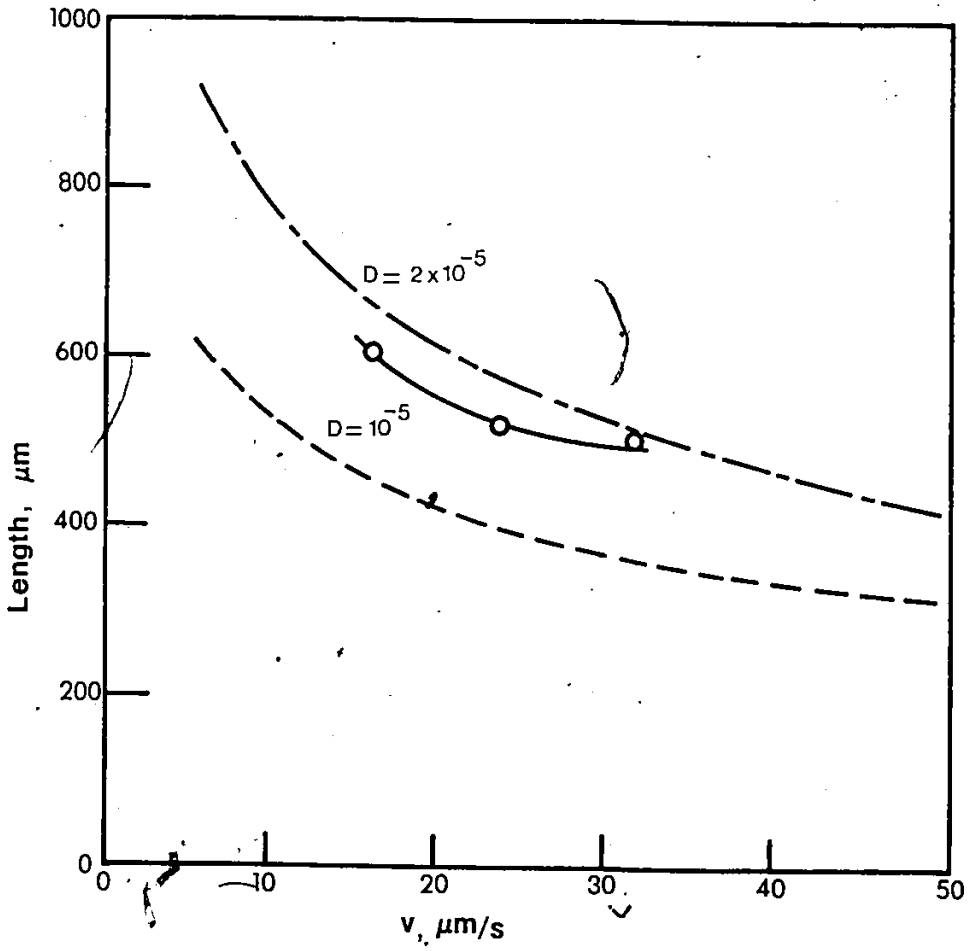


Fig. 51: Length versus velocity. G = 150°C/cm. $X_o$ = 0.02.

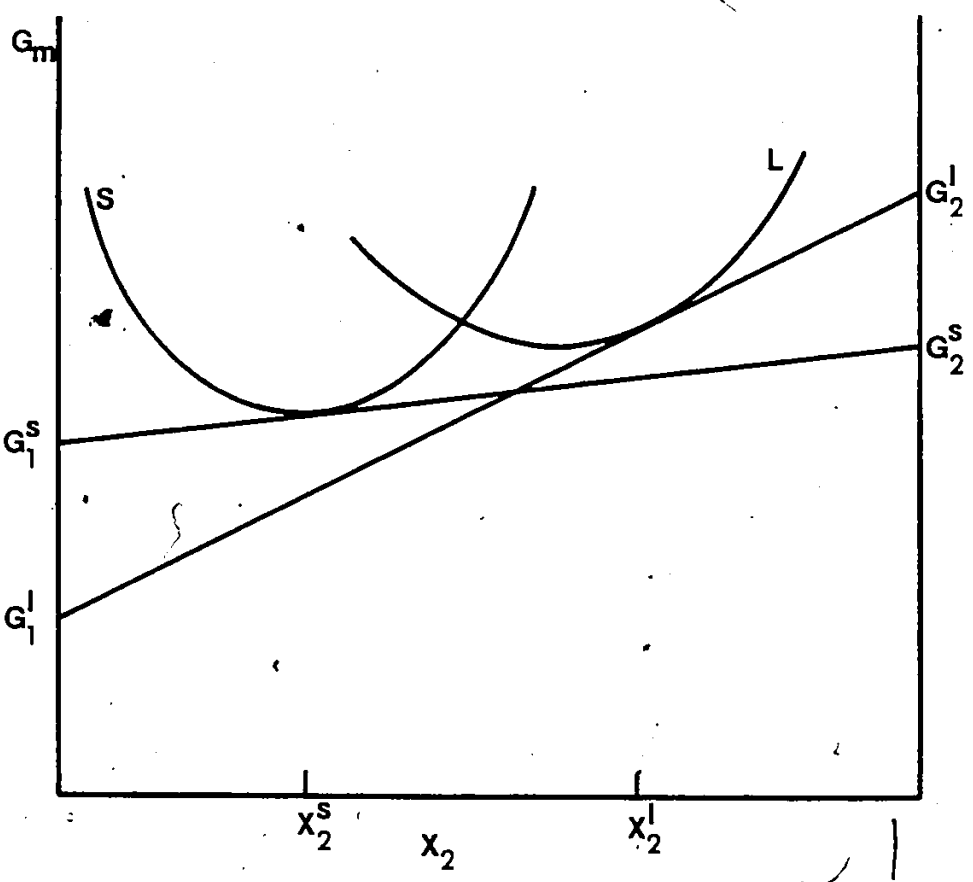


Fig. 52: Schematic free energy-composition diagram showing a thermodynamic condition for a stationary non-equilibrium interface.